BIOLOGICAL AND ENVIRONMENTAL APPLICATIONS OF PHYTOGENIC ZnO NANOPARTICLES

Thesis Submitted
to the University of Calicut for the
award of

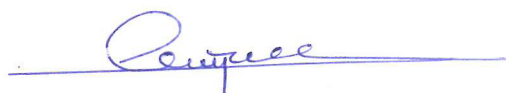## DOCTOR OF PHILOSOPHY IN CHEMISTRY

ANUPAMA R PRASAD

DEPARTMENT OF CHEMISTRY
UNIVERSITY OF CALICUT
KERALA- 673635
OCTOBER 2020

Declaration

I, **Anupama R Prasad**, hereby declare that thesis entitled as "Biological and Environmental Applications of Phytogenic ZnO Nanoparticles" submitted to the University of Calicut is a bona fide record of project work done by me under the supervision and guidance of **Dr. Abraham Joseph**, Professor, Department of Chemistry, University of Calicut and it has not formed the basis for the award of any Degree/Diploma/Associate ship/Fellowship or other similar title of any other University or Institution.
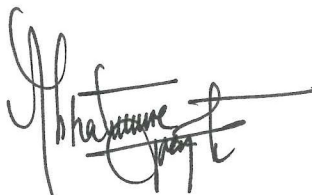
University of Calicut

Anupama R Prasad

Certificate

This is to certify that the thesis entitled "Biological and Environmental Applications of Phytogenic ZnO Nanoparticles" submitted to the University of Calicut, is a record of precise research work carried out by Anupama R Prasad at the Department of Chemistry, University of Calicut under my guidance and supervision. The contents of the thesis have been checked for plagiarism using the software 'Urkund' and the similarity index falls under permissible limit, and I further certify that the thesis or part has not previously formed the basis for the award of any degree, diploma or associate ship of any other University or Institute.

The suggestions/corrections recommended by the adjudicators have been made in the revised thesis.

University of Calicut

Dr. Abraham Joseph
Professor
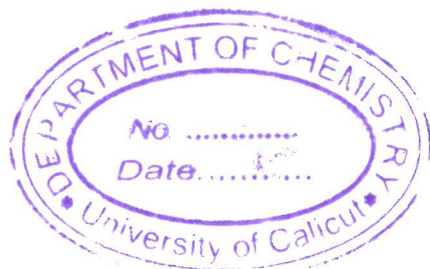
Acknowledgment

I wish to express my sincere appreciation to my supervisor, Dr. Abraham Joseph, who has the substance of a genius: he convincingly guided and encouraged me to be professional and do the right thing even when the road got tough. I would like to pay my special regards to Dr. A.I. Yahya, Head of the department of Chemistry, University of Calicut and former HODs of the department for providing the basic facilities during my Ph.D programme. Sincere thanks to the faculty members of the department Dr. P. Raveendran, Dr. K. Muraleedharan, Dr. N.K. Renuka, Dr. M.T. Ramesan and Dr. Pradeepan Periyatt.

I reverentially memorize late Professor M. Prabhakaran Nair, who hold my hands to the world of knowledge. To my former teachers: it is whole-heartedly appreciated that your great advice for my study proved monumental towards the success of my steps. I would like to recognize the support and assistance provided by our group members. It's my pleasure to thank Dr. K. Ramya, Dr. K.K. Anupama, Dr. K.M. Shainy, Dr. Rugmini Ammal P, Dr. Parajila M, Dr. Mathew Kuruvilla, Dr. Sabeel M. Basheer, Shamsheera K.O, Julia Garvasis, Sr. Asha Thomas, Jaseela P.K, P. Sowmya and Linda Williams. Sincere thanks to the research scholars, M. Phil students and non-teaching staffs of the department. Thanks to Mr. Aijon Pappachan, Ms. Reshmi S, Mr. Nidheesh Roy, Ms. Induja Gupta, Ms. Anila Jineesh, Mr. Faisalmoossa Athikkavil, Dr. K.K. Elyas Dr. Sanjay Gopal, Dr. Sangeeth Kallatt, and Dr. Jithesh Kavil.

I acknowledge the services provide by the Central Sophisticated Instrument Facility (CSIF) of University of Calicut, The Indian Nanoelectronics Users Program (INUP) of Indian Institute of Science- Bangalore (IISc), Central Leather Research Institute (CLRI) - Chennai, Central Sophisticated Instrument

"Having somewhere to go is home. Having someone to love is family. And having both is a blessing." My dear ones, your love, care, encouragement and support are most reminisced here. Devadevan, my dear little charm, love you so much. I am honestly grateful to the blessings of god almighty those I once enjoyed or those I enjoy now.

Anupama

Table of Contents

To,

Hari, Jithu, Sudha, Prasad, and myself

"Those who wished to happen and made it happen"

Preface

Nanoparticles have been integrated into health, food, feed, space, chemical, and cosmetics industries which calls for a green and benign approach to their synthesis. Nano science and technology is a wide and interdisciplinary area of science being fast developed in past few years. Nanomaterials are capable to addresses challenges in energy consumption, environmental pollution control and health remediation. Green chemistry has paved way for the development of eco-friendly approach for the synthesis of nanoparticles. Green synthesis of nanoparticles is an approach of developing nanoparticles using different biological components such as microorganisms, plants and other bio-regenerable materials. The natural strains and plant extract secrete some phytochemicals that act as both reducing agent and capping/stabilizing agents. Microorganisms have their intracellular enzymes capable of reducing metal ions which accounts for the feasible formation of nanoparticles. Plant based nanosynthesis gained preference owing to the great biodiversity, safest implementation, cost effective and easy synthesis of nanoparticles in large scale.

The green synthesis of metal oxide nanoparticles has the foremost choice of using plant extracts. Here the research instigates with an experiential selection of the plants from the widespread diversity. Leaves are extensively used for the synthesis amid different plant parts. In fact, they own the prime storage of active phytochemicals. Moreover, the choice become renewable, profuse and non-destructive to the source plant rather than using other plant parts. In the similar

sense the consumption of fruits and crops are benign. The altered experimental conditions can influence the yield and characteristics of particular nanoparticles obtained. Nanocrystalline transition-metal oxides have received wide attention due to unique properties that are technologically sound and used in nanodevice fabrications. Among metal oxides, ZnO has gained special attention due to striking physicochemical properties.Zinc oxide is an inorganic semiconductor, crystalline, biocompatible, less toxic, inexpensive, easily producible and available material which is highly demanded in nanoscale dimensions owing to exclusive potentials in all science stadia. Nano zinc oxide is a versatile material that has been functional in numerous areas. Green synthesized ZnO nanoparticles are nontoxic, biosafe and biocompatible. Further these nanoparticles are also used as drug carriers and in cosmetics and pharmaceutical industries.

Being versatile and benign material, biogenic synthesis of ZnO nanoparticles, characterization and its environmental and biological applications is the matter of our present study. Accounting the benefits and need to promote green synthesis routes, ZnO nanoparticles is prepared by using the plant extracts including the *Citrus lemon* extract, *Abelmoschus esculents* mucilage and *Gliricidia sepium* leaf extract. The thesis is literally presented in seven chapters. **Chapter 1** describes the background of the study, introduction to the green synthesis of nanoparticles, phyto-mediated nanosynthesis and the properties and applications of ZnO nanoparticles. This chapter also comprised of a literature review on the phyto-mediated synthesis of nanoparticles,

photodegradation, antibacterial activity, thermoluminescence, Bovine Serum Albumin binding, antidiabetic activity and theoretical approaches in nanoparticle-biomolecule interactions. The materials, synthesis methods, details of characterization techniques and experimental procedures carried out for the application studies have been defined in **Chapter 2**.

Chapter 3 contains the results of material characterization. The ZnO samples prepared using *citrus lemon* extract, *Abelmoschus esculents* mucilage and *Gliricidia sepium* leaf extract were characterized using field emission scanning electron microscopy (FESEM), high-resolution transmission electron microscopy (HRTEM), X-Ray diffraction (XRD) patterns, selected area diffraction patterns (SAED), fourier transform infrared (FTIR) spectra, diffuse reflectance spectra (DRS), energy dispersive X-ray spectroscopy (EDX), X-ray photoelectron spectroscopy (XPS) and zeta potential analysis.

Diabetes mellitus is a multifunctional disease identified as one among the major death causing diseases world-wide and would be the prime cause of illness and decease in coming decades. The strategies of stimulation of insulin production (Type 1) and inhibition of carbohydrate hydrolysing enzymes(Type 2) like α-amylase, α-glucosidase etc. are proven to be effective for controlling the blood glucose levels in the body. For Type 2 diabetic treatment, the inhibitors having mild amylase and strong glucosidase inhibition are preferred. ZnO nanoparticles have received wide attention for the biomedical applications. Moreover, zinc is the most common trace element in

human body after iron, and present in the structure of more than 300 enzymes as a cofactor. Zinc plays important role in various biological processes including glucose metabolism wherein improves the glucose conception by stimulating hepatic glycogenesis. Even though many of the inorganic materials especially those derived from green strategies have been investigated for the α-glucosidase and α-amylase inhibition, zinc-based inhibitors are being preferentially investigated. The *in-vitro* studies on the carbohydrate hydrolysing enzymes are beneficial to sort and exclude inactive candidates when a number of compounds are to be examined, thereby saving substantial time and money. **Chapter 4** covers the results of *in-vitro* α-glucosidase and α-amylase inhibition activity of the synthesized ZnO nanoparticles.

When nanoparticles enter in to a biological system, its surface gets covered with protein layers which is called corona. Therefore, a proper understanding and control on its physiological behaviour is crucial in the field of nanomedicine and environmental protection.Metal oxide nanoparticles are assumed to have strong interaction with the electron rich proteins. *In-vitro* studies with some model proteins are in common practice to understand these types of interactions. The results of the interaction (spectrophotometric monitoring) of ZnO nanoparticles with Bovine Serum Albumin (BSA) is described in **Chapter 5.**

The theoretical approaches using computational simulations can provide some complementary evidences for the binding of nanoparticles with the biomolecules, better understanding and visualization of the surface interactions. Computational modelling can

be a guide to design nanomaterials for the future biomedical experiments. Moreover, theoretical calculations can provide a near-idea of these experimental results, rather than conducting numerous trials. Molecular docking is a bio-informatics modelling tool which provides the possible orientations of two or more molecules when they interact each other to form a stable adduct with minimum energy. The docking models are capable of forecasting a three-dimensional view of any such complexes, the strength and type of interactions involved reliant on the binding characteristics of the ligand and target molecule. It can generate a set of probable complex structures that are ranked by total energy, and assembled via scoring function software. **Chapter 6** expounds the results of *In-silico* docking studies on the interaction of ZnO nanoparticles with BSA, α-glucosidase and α-amylase.

Industrial waste water possesses non-biodegradable and organic dyes that are toxic to living organisms. Photodegradation is an important and superior eco-friendly technique for industrial impurities which are highly toxic and difficult to treat by common chemical pathways. Photocatalytic degradation of organic pollutants is highly sought, because dye contaminants from various industries enter into the aquatic ecosystem, which affects the aquatic flora and fauna. Semiconducting nano zinc oxide is a renowned photocatalyst. The degradation efficiency is related to the synthetic root, surface characteristics and dopant effects if any. The photodegradation of organic dyes (Methylene Blue and Rhodamine B) has been studied using ZnO nanoparticles under UV and direct sunlight and the results

have been presented in **Chapter 7.** This chapter also encompasses the thermally stimulated luminescence (TL) emission of the synthesized ZnO nanoparticles. It is a phenomenon associated to the thermally stimulated light emission after a material sample is exposed to a beam of ionizing radiation or UV light. Both synthetic and natural TL-phosphors were introduced for low and high dosage applications in diverse areas including industrial, environmental and domestic sectors. Thermoluminescence technique has been applied in the field of radiation dosimetry and found to be highly successful in dating ancient pottery samples. It is also used in the study of biological and biochemical systems, forensic and geosciences. The thesis ends up with the **future outlook**.

Introduction and Literature Review

Zinc oxide (ZnO) nanostructures constitute the cutting edge of modern innovative research due to their distinct properties and their employment in an array of applications. The versatile nature enabling to use in various fields such as medicine, environmental remediation, antimicrobial activity and agriculture. Over the past few decades, the term "green synthesis" has received great attraction in materials science for synthesising inclusive nanomaterials in a sustainable and eco-benevolent route. The biological materials itself or their specified components play the dual role of reducing agent and the stabilizer/capping agent. The green synthesis of metal oxide nanoparticles has the foremost choice of using plants.

"Green chemistry is replacing our industrial chemistry with natures' recipe book. It's not easy, because life uses only a subset of elements in the periodic table, and we use all of them, even the toxic ones"

Janine Benyus

1.1. Background

Materials are produced in nano dimensions to achieve novel characteristics and properties which is absent in its bulk form. The nanoparticles have high surface to volume ratio, small size, quantum confinement and their unique physicochemical properties which accounts for the enhanced potential. Nano science and technology is a wide and interdisciplinary area of science being explosively developed in past few years.Nanomaterials have been integrated into health, food, feed, space, chemical, and cosmetics industries which calls for a green and benign approach to their synthesis.They are capable to addresses challenges in energy consumption, environmental pollution control and health remediations. Nanoparticles are used widely in mechanics, chemical industries, optics, catalysis, optoelectronics, biomedical sciences, and energy science [1–5]. Nanocrystalline transition-metal oxides have received wide attention due to unique properties that are technologically sound and used in device fabrications.Different physical and chemical synthesis strategies have been reported for the development of nanomaterials and well-defined nanostructures. For industrial applications, it is necessary for the synthetic strategy to be simple and viable. Thus, for the past few decades enormous attention was received on green synthesis strategies which minimizes or completely avoids chemical by-products, employs less hazardous chemicals, environmentally benign solvents and renewable precursors [6-8].Researchers are focused on developing various metal oxides via more environment friendly ('green')synthesis routes. Green synthesis of nanoparticles is an approach of developing nanoparticles using different biological components such as microorganisms, plants and bio-regenerable materials [9]. The natural strains and plant extract secrete some phytochemicals that act as both reducing agent and capping/stabilizing agents. Microorganisms have their intracellular enzymes capable of reducing

metal ions which accounts for the feasible formation of nanoparticles. Plant based nano synthesis gained preference owing to the great biodiversity, safest implementation, cost effectiveness and easy synthesis of nanoparticles in large scale.

1.2. Green synthesis of metal oxide nanoparticles

Over the past few decades, the term 'green synthesis' has received great attraction in materials science for synthesising inclusive nanomaterials in a sustainable and eco-benevolent route. The green strategies are viable and remediate the adverse effect of chemical synthesis by curtailing or completely eradicating the chemical by-products, applying less hazardous chemicals, environmentally benign solvents and renewable precursors. In a classical chemical synthesis, capping agents or stabilising agents are mandatory in order to control the particle size by passivating or preventing particle aggregation and thereby achieving particles of desired morphology with high degree of uniformity. Hetero atom functionalised long chain hydrocarbons (hexadecylamine, octadecylamine, oleic acid, linolinic acid, triphenylphosphene, 2-mercapto ethanol, etc), polymers (polyvinyl pyrrolidone, polyvinyl alcohol, etc), dendrimers and block co-polymers are some common capping agents used in nano synthesis [10]. A large number of biological materials, such as plant extracts, microorganisms, algae and biodegenerable materials (like amino acids, proteins and vitamins) have been adopted in scene of alternative green remedies, especially for the development of metal/metal oxide nanoparticles. The nanomaterials of such methodical origin are branded as 'biogenic' [9]. Fig.1 presents the general approaches of nanoparticle synthesis, their comprised classes and sub-classes of green synthesis.
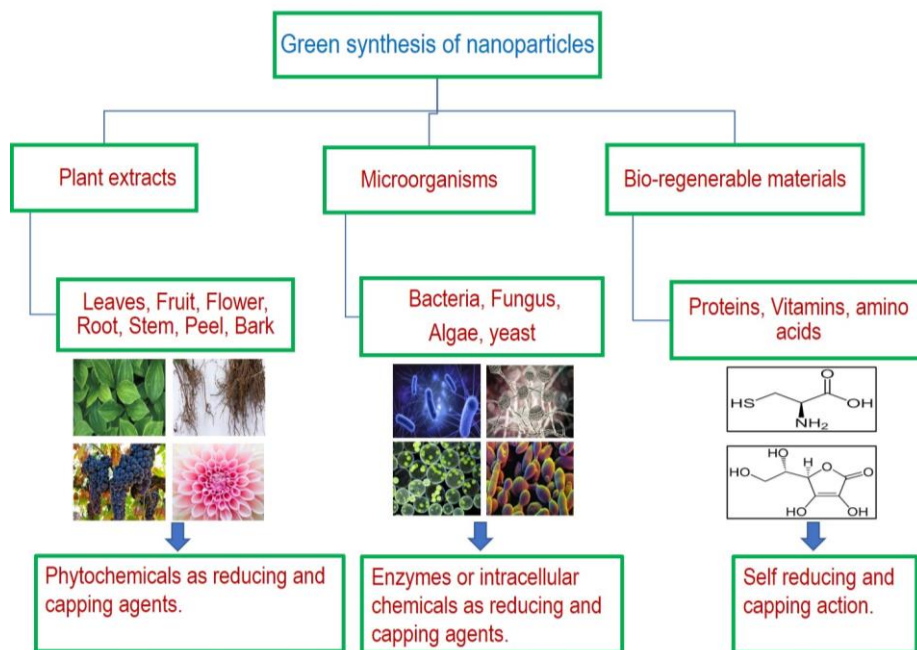
Fig.1. Green synthesis routes for metal oxide nanoparticles.

The biological materials itself or their specified components play the dual role of reducing agent and the stabilizer/capping agent. Some bacterial strains inherently possess the ability to reduce metal ions and their ease of manipulation made momentous contenders in metal/metal oxide nanoparticle synthesis [11, 12]. *Lactobacillus casei, Prokaryotic bacteria, Enterobacter cloacae, Pseudomonasproteolytica, Bacillusindicus, Aeromonas sp. SH10 PhaeocystisAntarctica, Bacillus amyloliquefaciens, Bacillus cecembensis, actinomycetes, Escherichia coli, Bacilluscereus,* are some extensively employed bacterial strains for nano metal oxide synthesis. A competent fungus is able to produce bulk quantity of nanoparticle than of bacterial strains [13]. Also, the method exploiting fungi for the nano synthesis is highly efficient in producing monodispersed metallic nanoparticles with distinct morphology. The intracellular enzymes capable of reducing metal

ions accounts for the feasible formation [14]. Yeasts are another momentous biological candidate applied in nanoparticle synthesis. There is numerous successful yeast-assisted green synthesis reported for the production of diverse metallic nanoparticles. Silver, gold, zinc and titanium nanoparticles are immensely developed with the micro-organism assisted reduction. These are also extensively synthesized with the plant extracts which has an exclusive storage of reducing phytochemicals such as polyphenols, flavanones, terpenoids, amino acids, alkaloids and some aldehydes/ketones [15]. The phyto-mediated synthesis strategies are highly preferred owing to the great biodiversity and safest execution. In addition to the eco-safety, the overall energy conception, cost reduction and effortless production of nanomaterials in large scale are viable [9, 16].

1.3. Phyto mediated synthesis of metal oxide nanoparticles

The green synthesis of metal oxide nanoparticles has the foremost choice of using plants. A biogenic synthesis of nanoparticles using bacteria, fungi or other microorganisms has to deal with some issues that are related to cell culture preparation, incubation period and their further analysis which makes them tedious and time consuming. Several limitations in the microbes assisted synthesis can be resolved in the phytogenic green synthesis that is comparatively simple and fast. The plant mediated nano synthesis has become a current nanobiotechnology research which involves the mechanism of bio-assisted reduction, nucleation, particle growth and stabilization of nanoparticles [9, 16]. Here the research instigates with an experiential selection of the plants from the widespread diversity [16]. The secondary metabolites can synergistically reduce the precursor metal ion. However, different plant fragments (seed, root, leaf etc) have a typical phytochemical content with varying proportions and concentrations [17, 18]. This varying

profile is attributed to the function of the specific parts and biotic and abiotic stress on the plant [16]. Consequently, the green strategy utilizes the different plant parts since the nanoparticles derived could have variable characteristics and functions.
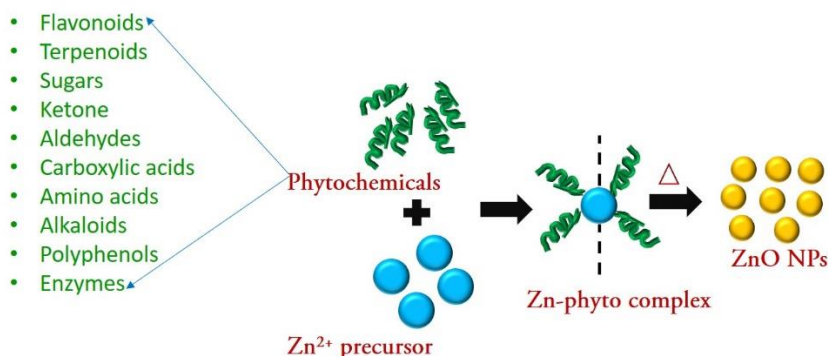
Fig.2. Schematic representation of mechanism involved in plant-based ZnO nanoparticle synthesis and possible active phytochemicals.

Leaves are extensively used for the synthesis amid different plant parts. In fact, they own the prime storage of active phytochemicals. Moreover, the choice become renewable, profuse and non-destructive to the source plant rather than using other plant parts [16]. In the similar sense the consumption of fruits and crops are benign. The altered experimental conditions can influence the yield and characteristics of particular nanoparticle obtained. The major constraints are the concentration of precursor metallic salt, concentration of plant extract, temperature, pH and reaction time [19]. Different plant parts or their extracts of leaf, stem, fruit, flowers, root etc are used in the synthesis procedures. The parts are either dried or grinded to form the powder or used directly to obtain extract. The plant, plant extracts or their products used in nanoparticle synthesis contain natural entities that can supplant the chemicals (surfactants or polymers) that act as reducing agent, capping agent or as stabilising agent.

5

Phyto synthesis are frequently practiced for the development of various metal oxide nanoparticles including ZnO, CuO, TiO$_2$ etc. In most of the recent reports, the phytogenic synthesis of nano ZnO is achieved by simply mixing the extract prepared from plants rich with phytochemicals and the zinc precursor solution. In a typical phyto- mediated synthesis, plant parts such as leaves, etc. are collected from different sources, thoroughly washed with tap water and distilled water to remove debris and other unwanted materials. The plant parts are chopped into small pieces or grinded to powder and boiled in different solvents (water, ethanol, etc.) and heated to prepare extract. Different concentration of zinc precursor and extract under different pH and temperatures can be applied for the preparation of nanoparticles.Commonly, the synthesised nanoparticles are annealed to intensify the crystalline nature. According to the tentative mechanisms suggested for the formation of ZnO nanoparticles via plant extracts, initially the phytochemicals coordinate (mainly through donor oxygens) with the Zn^{2+} leading to the formation of some Zn-phyto complex. The complex gets decomposed on calcination resulting ZnO nanoparticles.Fig.2 shows the list of major secondary metabolites believed to be the primary candidates causing metal reduction and the possible formation mechanism in general.

1.4. Zinc Oxide nanoparticles

The group II-IV semiconductors have either cubic zinc blend or hexagonal wurtzite crystal structure. Each anion will be enclosed by four number of cations in an archetypal tetrahedral sp^3 coordination and vice-versa. However, their band gap energies are higher beyond the values anticipated from the covalent bonding owing to the substantial ionic nature owned. Zinc oxide belongs to this class of II-IV semiconductors possessing a border line ionicity and exhibits three types of crystal structures wurtzite, zinc blend and

rock salt as schematically depicted in Fig.3. The wurtzite ZnO is the thermodynamically most stable crystalline symmetry under ambient conditions. A stable zinc blend structure is feasible only if the crystal grown on a cubic substratum and the rock salt symmetry requires high pressure conditions. The electronic band gap structure is allotted with 3d orbitals of zinc contributing the valance band and oxygen 2p orbitals to the conduction band [20].
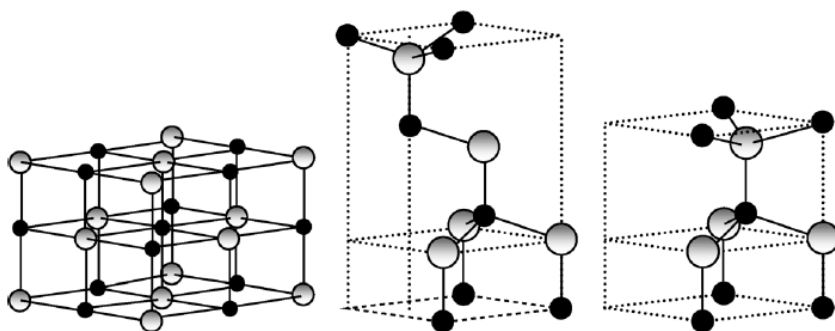
Fig.3. Crystal structures of ZnO.

Among metal oxides, ZnO has gained special attention due to its wide band gap (3.37 eV), non-toxicity, high photosensitivity, physico-chemical stability, and large exciton binding energy (60 meV). ZnO nanoparticles are used in catalysis, piezoelectric devices, pigments, chemical sensors and cosmetic materials, especially for ultraviolet (UV) protection [21-25]. Zinc oxide is an inorganic semiconductor, crystalline, biocompatible, less toxic, inexpensive, easily producible and available material which is highly demanded in nanoscale dimensions owing to exclusive potentials in all science stadia. Over the past few years zinc oxide-based nanomaterials are governing attention and extensively applied in diverse environmental and biological applications including water remediation, energy storage, gas sensors, cosmetics, nanomedicines, solar cells, photonic devices, biosensors, spin

electronics, catalyst, paints/coatings, optoelectronic devices, enzyme inhibition, microbial action, anti-inflammation, drug delivery and cancer therapy [26-42]. Moreover, the material has good photostability, thermal stability, broad adsorption range and wide band gap which made cost-effective substitute for titania nanomaterials in photocatalysis [8, 43].ZnO nanoparticles have received wide attention for the biomedical applications including drug delivery, antimicrobial, biological sensing, bio labelling, larvicidal and antibacterial applications [44, 31]. Moreover, zinc is the most common trace element in human body after iron, and present in the structure of more than 300 enzymes as a cofactor. ZnO nanoparticles is an eco-friendly, nontoxic, biocompatible, low cost, and naturally abundant documented as safe material by U.S. Food and Drug Administration [45–49].

1.5. Photodegradation of organic dyes

Non-biodegradable organic dyes are common colouring agents in textile, leather, cosmetics, paper, printing, plastic, rubber and pharmaceutical industries and their direct discharge to water sources or ecosystems create adverse effects. The rate of dye conception has been increased proportionally with the global population and during the last 30 years there is a similar growing production-conception statistics. Fig.4 portrays the world conception statistics of synthetic dyes. For the industry environmental issues and toxicity concerns are enduring challenges. Major classes of industrial dyes are highly reactive and they are non-biodegradable, recalcitrant, stable oxidizing agents, thermo stable, toxic and mutagenic in nature [50-55]. Persistence of dyes even in small concentrations will inhibit the solar light penetration in to water which retards the photosynthetic action, stunt the biota growth thereby impart toxicity in aquatic life and makes the water source undesirable for usage [55-61]. Thus, serious attention and severe struggle

should be paid to remove the dye pollutants from the contaminated media before its release in to natural streams. There are some common physicochemical methods employed for dye/impurity removal from aquatic systems including photodegradation, membrane separation, irradiation, ozonisation, chemical coagulation, electrochemical coagulation and biosorption [62, 63].
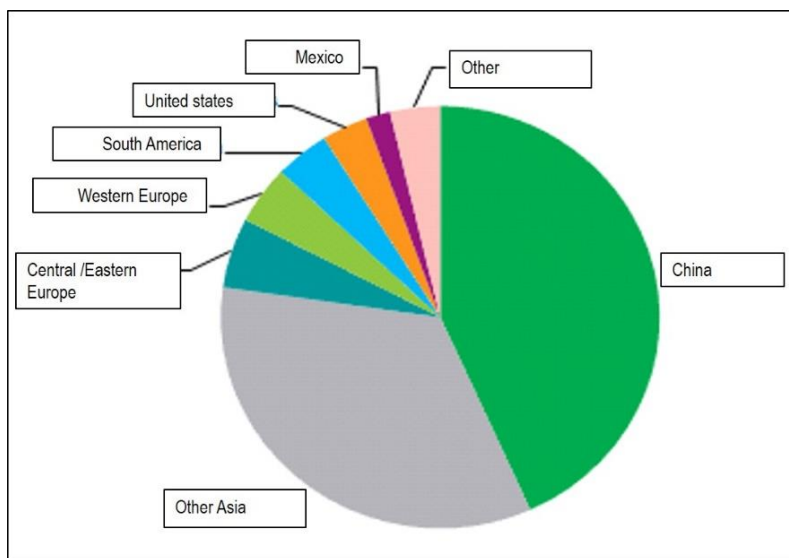
Fig.4. World consumption statistics of synthetic dyes.

Photodegradation is an important and superior eco-friendly technique for industrial impurities which are highly toxic and difficult to treat by common chemical pathways [8].The process makes the catalytic oxidation of organic molecules present in aquatic systems by generating highly reactive hydroxyl radical. Semiconductor metal oxide nanoparticles such as ZnO, TiO_2, ZrO_2, MnO_2, Fe_2O_3 and CuO are generally used for the photodegradation of dye pollutants in water matrices. ZnO has more quantum efficiency as it absorbs comparatively large portion of UV spectrum than other metal oxide nanostructures and is the most promising inorganic semiconductor

photocatalyst [64, 65]. The degradation efficiency is related to the synthetic root, surface characteristics and dopant effects if any [66]. According to the semiconductor photocatalysis, illumination of ZnO catalyst with appropriate UV-light having energy equal or more than the photo-threshold energy cause electronic excitations and consequent generation of electron-hole pairs. These e–h pairs later diffuse to the catalyst surface and combine with the molecular oxygen and hydroxide ions forming super strong oxidizing hydroxy and hydroperoxy radicals capable of organic dye degradation [8, 67, 68]. A schematic mechanism of photo dye degradation has been presented in Fig.5.
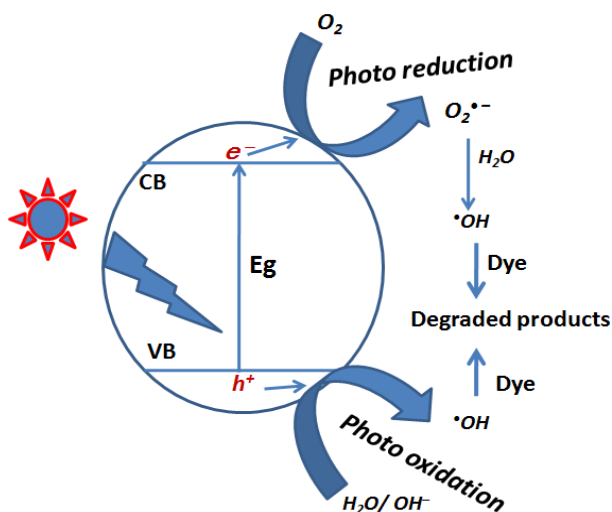
Fig.5. Schematic mechanism of photodegradation of organic dyes.

1.6. Thermoluminescence/Thermally stimulated luminescence (TSL)

Thermally stimulated luminescence (TL/TSL) is one of the basic experimental techniques employed for obtaining information about the characteristics of energy levels existing due to the presence of defects and impurities in semiconductors and insulators [69-72]. It is a phenomenon associated to the thermally stimulated light emission after a material sample

is exposed to a beam of ionizing radiation or UV light. Both synthetic and natural TL-phosphors were introduced for low and high dosage applications in diverse areas including industrial, environmental and domestic sectors [73, 74].
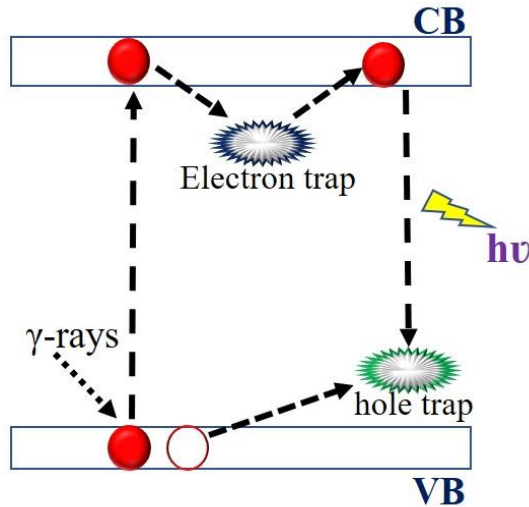
Fig.6. Mechanism of Thermoluminescence emission.

Fig.6 represents the mechanism of TL phenomenon. Here the electron(s) get excited with the ionizing radiation (gamma) to the conduction band leaving hole(s) in valance band. This excited electron then captured by the electron trap(s) occupying underneath the conduction band. Similarly, the hole generated can move to the hole trap(s) situating slightly above the valance band. On progressive heating of the material, at a specific temperature defined for the energy level of the trap, the electron receipts the thermal energy and get re-excited back to the conduction band. When the thermal energy supplied is not sufficient to liberate the trapped holes, the released electrons migrate to the nearby trapped hole with the emission of photon [75].

Thermoluminescence technique has been applied in the field of radiation dosimetry and found to be highly successful in dating ancient pottery samples. It is also used in the study of biological and biochemical systems. Further in forensic sciences it helps to evolve and standardize methods to compare evidentiary materials with similar materials of known origin, which are invariably available only in minute quantities and are required to be analyzed non-destructively for evidences. In geosciences, TL is being used as chronometers to provide the ages of the last resetting event. The thermoluminescence properties of pure and doped ZnO at low temperature using different types of radiation, where studied in the form of powders and thin films. Further, ZnO is inert to environmental conditions, nontoxic and insoluble in water. However, a few reports related with TL features above room temperature and with the potential application of ZnO in TL dosimetry are now available.

1.7. Antibacterial activity

Nanomaterials especially metal oxide nanoparticles provide activity against a broad spectrum of pathogens. The metal oxide nanoparticles such as ZnO, MgO, CaO and some noble metal oxides were extensively studied during the past few years for their antimicrobial activity [76-78]. Antimicrobial agents invariably enable to prevent and also to treat infectious diseases in animals and humans. Many of the antimicrobial agents play a pivotal role in the promotion of growth and development in humans and animals and also helps to increase the feed function. Due to its antimicrobial properties, ZnO has been incorporated into the linings of food cans in packages for meat, fish, corn, and peas to preserve colours and also to avoid spoilage [7]. The nanoparticles have a very high prominent antimicrobial properties than its large particles because of the small size (<100nm). During waste water

processing, the bacterial decontamination is essential and challenging [7]. Moreover, nanoparticles in the antimicrobials could also be a novel strategy that can be exploited in the drug delivery systems to overcome the challenges associated with antibiotic therapy.
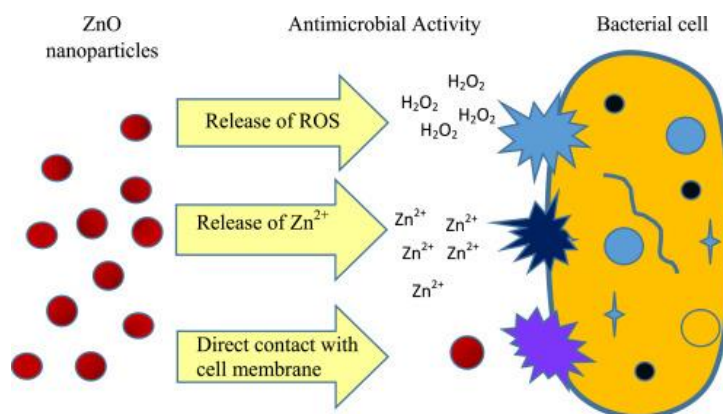
Fig.7. Possible mechanisms for the anti-bacterial activity of ZnO nanoparticles.

The exact mechanism of antibacterial properties of nanoparticles is still ambiguous while several possible premises have been predicted by researchers. The management of oxidative stress imparted by the production of reactive oxygen species/reactive oxygen radicals (ROS) by ZnO nanoparticles is the one proposed by majority of research groups. This ROS can disrupt the DNA, proteins, lipids etc. resulting bacterial cell death [79, 80]. According to Costa and team, nanoparticles with small size can easily penetrate through the cell membranes [81, 82]. The nanoparticle accumulation in cell membrane and their concentration inside the cell result in loss of membrane integrity causing bacterial destruction. Binding of Zn^{2+} ions released to the cell membrane arresting bacterial growth is also proposed [79].Fig.7 shows the all possible mechanisms suggested for the anti-bacterial activity of zinc oxide nanoparticles.

1.8. Antidiabetic activity

Diabetes mellitus has been recognized as one of the major deaths causing diseases in the world. Globally a large patient population around 200 million are currently seeking treatments while the heterogeneous nature of the disease demands cost effective and multifunctional therapies [83, 84]. The International Diabetes Federation (IDF) estimates inflation in the population of diabetic patients beyond 592 million in the coming 25 years [85, 86]. Chronic metabolic disorders characterized by hyperglycemia; elevated blood sugar level due to insufficient insulin production or the loss of cell response to the produced insulin leading to the rise in blood glucose level are often associated with diabetics [87-89]. Inhibition of the enzymatic activity of carbohydrate hydrolysing enzymes in the digestive track can delay the carbohydrate digestion and thereby reduce glucose uptake [83]. The diabetic management strategy of employing enzymatic inhibitors with strong α-glucosidase and mild α-amylase inhibition is effective for diabetic control [89, 91]. Fig.8 represents the function of α-glucosidase and α-amylase in glucose metabolism. Since the consequent gastro-intestinal side effects of many of the established therapeutic medicines (inhibitors) such as acarbose, miglitol and voglibose were revealed, the development and practice of new enzymatic inhibitors are still a worthy research platform [89,91]. Even though some of the polyphenols from green extracts exhibited remarkable α-amylase inhibition, their application is limited due to easy decomposition in intestinal tract [92].
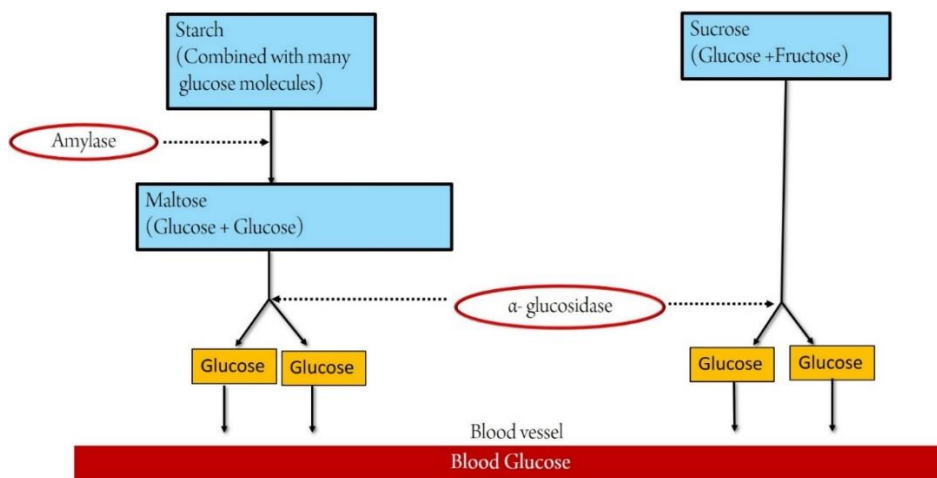
Fig. 8. Function of α-glucosidase and α-amylase in glucose metabolism.

Zinc plays important role in various biological processes including glucose metabolism wherein improves the glucose conception by stimulating hepatic glycogenesis [84,93]. Even though many of the inorganic materials especially those derived from green strategies have been investigated for the α-glucosidase and α-amylase inhibition, zinc-based inhibitors are being preferentially investigated.

1.9. Metal oxide- Serum albumin interaction

The electron-deficient metal and electron-rich biomolecule like proteins are assumed to have strong interaction [94]. Study of biomolecule interactions with metal is of great significance for the design of novel nano-drugs [95]. When nanoparticles enter in to a biological system, its surface gets covered with protein layers which is called corona. Therefore, a proper understanding and control on its physiological behaviour is crucial in the field of nanomedicine and environmental protection. Blood plasma is composed of some special proteins such as albumin, globulin and fibrinogen among which albumin is a macromolecular carrier and most abundant one [96]. Serum

albumins contribute to the colloidal osmotic pressure of blood in major and manage the transportation of drugs and nutrition through our body and also responsible for drug deposition [97–100]. Bovine Serum Albumin (BSA) is a water-soluble protein with molecular weight 66000 Da, contains 20 tyrosine, 30 phenylalanine and 2 tryptophan residues which take part in various physiological functions including delivery of fatty acids, bindings and transports [97,101]. The fluorescence emission spectra of BSA provides the best on local micro environment of its intrinsic fluorophores.

1.10.   Theoretical approaches in Nanoparticle-biomolecule interactions

Nanobiotechnology is an emerging interdisciplinary area of science for the twenty first century. Even though the experimental studies have made remarkable advancement in the area, it is essential to investigate and envisage the nano-bio interactions, which is hard to accomplish due to the limited resolution of currently available analytical instruments. The theoretical approaches using computational simulations can provide some complementary evidences for the binding of nanoparticles with the biomolecules, better understanding and visualization of the surface interactions. Computational modelling can be a guide to design nanomaterials for the future biomedical experiments. Moreover, theoretical calculations can provide a near-idea of these experimental results, rather than conducting numerous trials. Ab initio methods, density functional theories, molecular dynamics, dissipative particle dynamics, Monte Carlo techniques, coarse-grained models, and other multiscale methods are the frequently used computational techniques for investigating the nanoparticle-biomolecule interactions [102].

1.11.   Literature Review

"The more you know about your topic, the more effectively you can tackle your own research problem; it all start with a literature review"

Unknown

ZnO nanoparticles has been extensively prepared by employing plant extracts during the last few decades. Syed Md Humayun Akhter et al. fabricated ZnO nanoparticles using *Swertia chirayita* leaf extract. The Zn^{2+} are reduced to Zn which finally ends to well-defined zinc oxide nanoparticles that are spherical in shape. The reduction is favoured due to the polyols present in the reaction system [103]. Fig.9 represents the possible formation mechanism of ZnO nanoparticles obtained using *Nepheliumlappaceum* peel extract. The polyphenolic ellagic acid ligates with zinc ions to form zinc-ellagate complex through the aromatic hydroxyl group present in the molecule. Further, the complex gets converted to ZnO nanoparticles after calcination at 450ºC [104]. Similarly, the phyto-synthesis employing *Carica papaya* milk and V*itex negundo* leaves extract synopses the major reaction steps as (i) complexation, (ii) aggregation of nanoparticles and (iii) oxidation of phyto-components [105, 106].

The fruit extract of *Rosa canina* was used in the bio-fabrication of ZnO nanoparticles which was reported by Saeed Jafarirad et al. The major metabolites in fruits are phenolic acids, flavonoids, carotenoids, sugars, proanthocyanidins, tannins, flavonoids, fatty acids, pectin and fruit acids. They stated that the nanoparticles designed was stabilized by *in-situ* bio-capping ZnO by its attachment phenolic or carboxylic acid groups [107]. Plants with medicinal value have also been utilised for the synthesis of ZnO nanoparticles, for instance, N. Supraja et al. produced ZnO nanoparticles

using *Boswellia ovalifoliolata* stem bark-extract. The nanoparticles showed effective antimicrobial action against some selected bacteria and fungus [108].
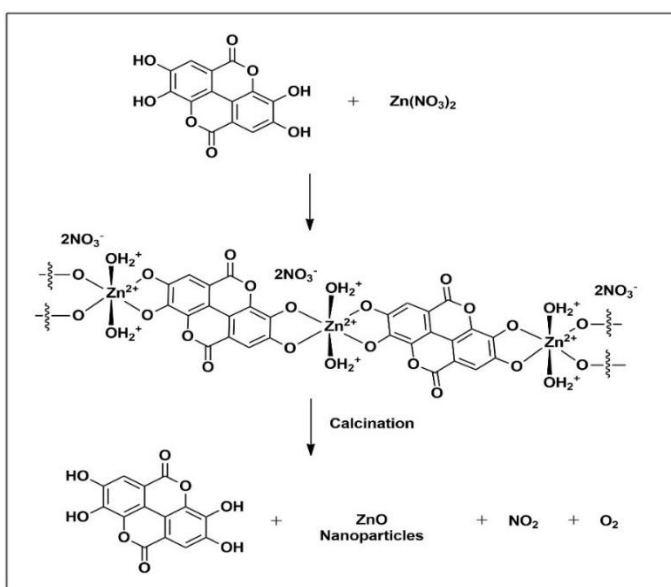
Fig.9. Formation mechanism of ZnO nanoparticles obtained using *Nepheliumlappaceum* peel extract

A detailed protocol of the synthesis of ZnO nanoparticles by *Jacaranda mimosifolia* flower extract is described by Sharma *et.al*. in 2016 [109]. The formation of nanoparticles was recognizable by visual observation and monitored using UV–visible spectrophotometer and the particle recovery was achieved further by centrifugation at high rpm, and washing thoroughly with solvents. ZnO nanoparticles were also synthesized by *Camellia sinensis* (green tea) leaf extract showed higher absorbance of 325 nm in UV–visible spectroscopy analysis. In this preparation, the nanoapraticles possess an average size of 16 nm with hexagonal morphology (Senthilkumar*et.al*. 2014) [110]. The green synthesis of ZnO nanoparticles was performed by an efficient, low-cost method using *Plectranthusamboinicus* leaf extract which

was studied and reported by Vijayakumar et al. 2013 [111]. The resultant nanoparticles were ranging in size from 20 to 50 nm. The morphological studies revealed the hexagonal shape of nanoparticles. Here ZnO nanoparticles obtained owned remarkable antibacterial and larvicidal action. Some recent reports on phytogenic ZnO nanoparticles have been listed in Table 1.

Table 1. ZnO nanoparticles synthesized using various plant products.

No	Source	Part	Shape/morphology	Ref
1	*Trifoliumpratense*	Flower	-----	[112]
2	*Aloe vera*	Leaves	Spherical, oval and hexagonal	[113]
3	*Nepheliumlappaceum L.*	Peel	Spherical	[114]
4	*Azadirachtaindica*	Leaves	Spherical	[115]
5	*Carica papaya*	Milk	Variable	[105]
6	*Polygala tenuifolia*	Roots	Spherical	[116]
7	*Vitex negundo*	Leaves	Spherical	[106]
9	*Anchusa italic*	Flower	Hexagonal	[117]
10	*Jacaranda mimosifolia*	Flowers	Variable	[109]
11	*Heritierafomes and Sonneratiaapetala*	Bark and leaves–	-----	[118]
12	*Carissa edulis*	Fruits	Flower shaped	[119]
13	*Plectranthusamboinicus*	Leaves	Spherical and hexagonal 20–50	[111]
14	*Solanum nigrum*	Leaves	Hexagonal	[120]
15	*Tamarindusindica*	Leaves	Spherical	[121]
16	*Artocarpusgomezianus*	Fruits	Spherical	[122]
17	*Moringa oleifera*	Leaves	Spherical	[123]
18	*Zingiber officinale*	Rhizome	Spherical	[124]
19	*Azadirachtaindica*	Leaves	Hexagonal, buds, cones, bundles and closed pine cone	[125]
20	*Black tea*	Waste	Rod shaped	[126]
21	*Citrus aurantifolia*	Fruits	Spherical	[121]

The USA Food and Drug Administration (FDA) has listed ZnO as 'GRAS' (Generally Recognized As Safe) material [127]. ZnO in nano size is more easily absorbed by the body. Phytogenic ZnO nanoparticles have been extensively studied for their biological applications and environmental remediations. Among the metal oxide nanoparticles, ZnO has been used widely as a semiconductor photocatalyst due to its high reaction rate, large number of reactive sites available, high efficiency in generating hydrogen peroxide, low cost and eco-friendly nature [128]. It has been established that ZnO, exhibits high efficiency in photodegradation of pollutants and can be used in large scale waste-water treatment. Due to the abundant release in industrial effluents and serious environmental impacts, organic dye pollutants are most investigated under photodegradation. ZnO nanoparticles obtained via normal chemical routes and green strategies are established as catalysts for the photodegradation of different water pollutants. Table 2 summarizes the recent reports on phytogenic ZnO nanoparticles employed for photodegradation.

Table 2. Photocatalystic performance of phytogenic ZnO nanoparticles

No.	Green source	Shape of ZnO nanoparticles	Size of ZnO nanoparticles	Pollutant	Irradiation source	Ref
1	*Artocarpus Heterophyllus leaf extract*	sponge-like agglomerated structures	15-25 nm	Rose Bengal dye	UV light	[129]
2	*Garcinia mangostana fruit pericarp*	Spherical	21 nm	Malachite Green	Sunlight	[130]
3	*Anisochilus carnosus leaf extract*	Spherical	20-40 nm	Methylene blue	UV light	[28]
4	*Phyllanthus niruri leaf extract*	rectangle, triangle, radial hexagonal, rod and spherical shapes	25.61 nm	Methylene Blue	UV light	[124]
5	*Aegle marmelos fruit pulp*	Spherical	30 nm	Methylene blue	UV light	[131]

6	*Azadirachtaindica leaf extract*	Spherical	9.6-25.5 nm	Methylene blue	UV light	[132]
7	*Dolichos Lablab L. leaf extract*	Hexagonal and triangular	7 to 49 nm	Methylene blue, Rhodamine B and Orange II	Visible light and near UV	[133]
8	*Hibiscus rosasinensis leaf extract*	Spherical	15-170 nm	palm oil mill effluent	UV light	[134]
9	*Scutellariabaicalensis root extract*	Sphere like	50 nm	Methylene blue	UV light	[135]
10	*Sechium edule leaf extract*	Spherical	32.6 nm	reactive blue 160	UV light	[136]
11	*Vitex trifolia L leaf extract*	Variable	28 nm	Methylene blue	UV light	[137]
12	*Carissa edulis extract*	Flower	50-55 nm	Congored	UV light	[119]
13	*Plectranthusamboinicus leaf extract*	rod	88 nm	Methyl red	UV light	[138]
14	*Calotropis procera leaf extract*	Spherical	15-25 nm	Methyl orange	UV light	[139]
15	*corriandrum sativum leaf extract*	--	9 nm	Anthracene	UV light	[140]
16	*Hippophaerhamnoides leaf extract*	Flower like	20.17 nm	Eosin Y and Malachite Green	UV light	[141]
17	*Ulva lactuca seaweed extract*	sponge-like asymmetrical shaped	10-50 nm	Methylene blue	Sunlight	[142]
18	*Nepheliumlappaceum L. Peel extract*	Aggregated clusters	25-40 nm	Methyl orange	UV light	[104]
19	*Azadirachtaindica leaf extract*	Spherical-agglomerated	35 nm	Methylene blue	Visible light	[143]
20	*Kalopanaxseptemlobus bark exttract*	Flower like	500 nm	Methylene blue	UV light	[144]
21	*Neem plant leaf extract*	Plates Bullets Flower Prismatic tip Closed pine cone	10-30 nm	Methylene blue	Sunlight and UV light	[125]
22	*Pithecellobium dulce peel extract*	Spherical	30 nm	Methylene blue	UV light	[145]
23	*Garcinia xanthochymus extract*	spongy cave like	20-30 nm	Methylene blue	Sunlight and UV light	[146]
24	*Citrus maxima juice*	agglomerated	10-20 nm	Methylene blue	UV light	[147]
27	*Tabernaemontanadivaricata green leaf extract*	spherical	20-25 nm	Methylene blue	Sunlight	[148]

28	*Carica papaya leaf extract*	Spherical	50 nm	Methylene blue	UV light	[128]
29	*Rubuscoreanus fruit extract*	leaf like	23.16 nm	Malachite green	tungsten bulb	[149]
30	*Lagerstroemia Speciosa leaf extract*	Variable	40 nm	Methyl orange	Sunlight	[150]
31	*ferulagoangulata boiss extract*	spheroid	44 nm	Rhodamine B	Visible light	[151]
32	*Suaeda japonica extract*	oval-shaped structures	100 nm	Methylene blue	UV light	[152]
33	*Citrullus lanatus rind extract*	Flower	100-200 nm	Methylene blue	UV light	[153]
34	*Eucalyptus globulus leaf extract*	Spherical	11.6 nm	Methylene blue, and Methyl orange	UV light	[154]
35	*oak fruit hull extract*	Spherical	34 nm	Basic violet 3	Visible light	[155]
36	*Allium sativum Allium cepa Petroselinum crispum*	Spherical	14-70 nm	Methylene blue	UV light	[156]
37	*Artocarpus Gomezianus extract*	Spherical	11.53 nm	Methylene blue Methyl orange	Sunlight and UV light	[122]
38	*Buchananialanzan leaf extract*	Agglomerated foam like	61.6-98.8 nm	Malachite green	Sunlight and UV light	[157]
39	*Cassiafistula plant extract*	Sponge like irregular shaped	5-15 nm	Methylene blue	Sunlight and UV light	[158]
40	*Arabic gum*	Spherical	10 nm	Direct blue 129	Visible light	[159]
41	*Vitislabruska skin extract*	Mysore pak canine teeth Hollow Pyramids Gems	50 nm	Methylene blue	Mercury lamp	[160]
42	*Cyanometraramiflora leaf extract*	Flower	13.33 nm	Rhodamine B	Sunlight	[161]
43	*ArtocarpusHeterophyllus leaf extract*	Spherical	10-30 nm	Congo red	UV light	[162]
44	*Thymus vulgaris leaf extract*	Irregular	50-60 nm	Methylene blue	UV light	[163]
45	*Apple pectin*	hollow double-caged peanut-like	6 μm (Biul form nanorods of 100 nm)	Methyl orange	UV light	[164]

The metal oxide nanoparticles exhibit remarkable antimicrobial action against a wide range of infectious microbes. Zinc oxide nanoparticles synthesized using plant extract shows an excellent antibacterial activity towards wide verity of Gram negative and Gram-positive bacterial strains including Escherichia coli, Staphylococcus aureus, Salmonella paratyphi, Vibrio cholerae, Bacillus subtilis, Listeria monocytogenes, Salmonella typhimurium, Pseudomonas aeruginosa, Klebsiella aerogenes, etc. The antibacterial action of ZnO nanomaterials is extended to food preservations and packaging, mainly to avoid spoilage and to increase the shelf-life of the packed food. This is achieved by the incorporation of ZnO nanoparticles to linings of cans and packages carrying the edible items. Deepali Sharma et al synthesized ZnO Nanoparticles using *Jacaranda mimosifolia* flower extract which showed antibacterial activity more prominent towards gram-positive bacterial strains. Gram positive bacteria have mainly an outer peptidoglycan layer which forms 80% of the cell wall and which is not an effective permeability barrier. The Gram-negative bacteria has only 10% of peptidoglycan and the remaining major content is lipopolysaccharides present in the outer cell membrane which makes it more compact and less permeable to ZnO nanoparticles. Also, the antibacterial activity was dependent on the size of the synthesized nanoparticles and the sensitivity of the different strains [109]. So far, a lot of research work is advancing in these fields where a variety of plants and their extracts have been made involved in the synthesis of ZnO nanoparticles. Some recent reports on phytogenic ZnO nanoparticles having substantial antibacterial activity has been provided in Table 3.

Table 3. Antibacterial studies of phytogenic ZnO nanoparticles

Phyto source	Size (nm)	Morphology	Bacteria	Ref
Acalyphaindica	19.9 53.39 65.13	irregular irregular spherical	*Escherichia coli, Staphylococcus aureus*	[165]
Anisochilus	30-40	quasi-spherical	*Salmonella paratyphi, Vibrio cholerae, Staphylococcus*	[28]

carnosus			*aureus, Escherichiacoli*	
Ceropegia candelabrum	12-35	hexagonal	*Staphylococcus aureus, Bacillus subtilis, Escherichia coli, Salmonella typhi*	[166]
Vitex negundo	75-80	spherical	*Staphylococcus aureus, Escherichia coli*	[106]
Aegle marmelos	30	spherical	*Escherichia coli, Pseudomonas aeruginosa, Staphylococcus aureus*	[131]
Murrayakoenigii	12	Spherical	*Staphylococcus aureus, Bacillus subtilis*	[167]
Rutagraveolens	20-30	spherical shaped nanoparticles agglomerated to cluster-like structure	*Klebsiella aerogenes, Escherichia coli, Pseudomonas desmolyticum, Staphylococcus aureus*	[168]
Monsoniaburkeana	5 -15	-	*Staphylococcus aureus, Enterococcus faecalis, Escherichia coli, Pseudomonas aeruginosa*	[169]
Glycosmis pentaphylla	32-36	spherical	*Bacillus cereus, Staphylococcus aureus, Shigella dysenteriae and Salmonella paratyphi*	[170]
Bauhinia tomentosa	22-94	hexagonal	*Bacillus subtilis, Staphylococcus Aureus, Escherichia coli and Pseudomonas aeruginosa*	[171]
Salvadoraoleoides	26.22 (pH 5) 38.62 (pH 8)	spherical and round irregular	*Bacillus cereus, Bacillus subtilis, Staphylococcus aureus, Corynebacterium rubrum, Escherichia coli, Pseudomonas aeruginosa, Klebsiella Pneumonia, Salmonella typhimurium*	[172]
Tectonagrandis	50-150	spherical	*Staphylococcus aureus, Bacillus subtilis, Escherichia coli, Salmonella paratyphi*	[173]
Swertia chirayita	2- 10	spherical shape	*Staphylococcus aureus, Escherichia coli, Salmonella enterica*	[103]

ZnO based thermoluminescent phosphors are often studied with different types of ionizing radiation including alpha, beta, gamma and X-rays. Nanocrystalline ZnO obtained via oxalyldihydrazide (fuel) combustion method exhibited a single broad TL glow curve centered at 343ºC stimulated with gamma radiation [174]. ZnO nanophosphors produced by glycine-based solution combustion synthesis on exposure to beta rays shown glow curves of two maxima located at ~149∘ C and another at ~308∘ C [175]. Pure ZnO nanoparticles derived by the thermal annealing of chemically synthesized ZnO was thermoluminescent on exposure to beta irradiation. It showed the high temperature glow curve situated around 341∘C and evidently belongs to a high temperature thermoluminescent material [73]. The gamma ray stimulated well-resolved TL glow curve centered ~354ºC was observed for ZnO nanorods prepared by surfactant free hydrothermal synthesis [176]. H. A. Borbo´n-Nun˜ez *et.al.,* have investigated the beta rays exposed thermoluminescence kinetics of pellet-shaped ZnO samples synthesized using chemical precipitation. The samples shown low temperature TL emission and promising for low dose TL dosimetry [177]. Beta rays induced high temperature TL emission profile was observed for nanocrystalline ZnO prepared by co-precipitation [178].

Most of the literature finds pure ZnO nanophosphors having thermoluminescence emission at higher temperatures. The thermoluminescence of ZnO can be tuned and enhanced by doping. For instance, gamma irradiated (m 0.05 to 4 kGy) Co^{2+} doped ZnO phosphor showed high intensity TL glow curves at ~411 K and ~575 K compared to the undoped sample. Here doping has made a low temperature thermoluminescence applicable for high dose TL dosimetry [179]. Whereas, Fe doped ZnO sample has exhibited single, well-resolved high temperature TL glow (368ºC) on gamma irradiation [180]. Ce^{4+}, Mn^{2+} and Mg^{2+} doped

ZnO samples have enhanced thermoluminescence emission under gamma irradiation [181, 182]. Similarly, high intensity glow curves were obtained for Mg^{2+} and Yb^{3+} samples exposed to beta irradiation compared to corresponding undoped ZnO samples [183-185]. X-ray induced thermoluminescence emission of pure and doped ZnO samples are also reported. They have comparatively low temperature emission profiles [186, 187].

There are reports of ZnO nanoparticles exhibiting both selective and cooperative inhibition of diabetic enzymes. For instance, *Costusigneus* leaf extract derived ZnO nanoparticles found to be efficient at *in-vitro* α-glucosidase and α-amylase inhibition even though the rate was higher for α-glucosidase [188]. A set of phyto-based ZnO nanoparticles using the aqueous plant extracts of *Azadirachtaindica*, Hibiscus *rosa-sinensis*, *Murrayakoenigii*, *Moringa oleifera*, and *Tamarindusindica* exhibited superior in-vitro enzyme inhibition than chemically obtained ZnO nanoparticles. The highest inhibition was obtained for those synthesized using, *Tamarindusindica* and *Moringa oleifera* extracts owing to the proteins and amino acid functionalization of resulting nanoparticles [189]. ZnO nanoparticles produced via aqueous extracts of *Andrographis paniculata, Heritierafomes* and *SonneratiaApetala* displayed moderate inhibition on α-amylase activity [190, 191]. In addition to the carbohydrate enzymes protein kinase B has important function in glucose metabolism by attending a key role in the stimulation of glucose uptake by insulin. *Silybummarianum* extract assisted ZnO nanoparticles showed moderate α-amylase and protein kinase B inhibition in the in-vitro monitoring [192].

Biological experiments frequently conduct the *in-vivo* monitoring over the in-vitro results since it explores better understanding on the net effects on the living organisms. The in-vivo research includes animal testing and various clinical trials. ZnO nanoparticles obtained with *Silybummarianum* L seed

extract was used for treating alloxan-induced diabetic rats and exhibited remarkable effect in curing the diabetic ailments. There were potential effects in reducing the levels of fasting blood sugar insulin level, triglycerols, and total cholesterol when compared to other treatments. Furthermore, ZnO nanoparticles was efficient for the preferment of high-density lipo-protein levels in the diabetic rats [118]. Biosynthesized ZnO nanoparticles using *Vaccinium arctostaphylos L.* leaf and fruit extract exhibited analogous results on alloxan-induced diabetic rats [118, 193]. The in-vivo studies on streptozotocin (STZ) induced diabetic mice monitored via enzyme linked immunosorbent assay (ELISA) and real time polymerase chain reaction (RT-PCR) revealed that ZnO nanoparticles can stimulate the function of Th1, Th2 cells and expressions of insulin receptors and other genes of the pancreas associated with diabetes [194].

Nanoparticle-protein interaction is currently an exclusive area of research. *In-vitro* ZnO-BSA interactions are generally monitored with spectrofluorimetric techniques. The experimental studies demonstrate the conjugation of nanoparticles with this model protein. ZnO quenches the fluorescence of BSA through complex formation. Colloidal ZnO nanoparticles exhibited considerable interaction with the BSA protein and the synchronous spectra recognized conformational changes in protein associated with the interaction [195, 196]. Chaitali Hansda*et.al.,* have investigated the photophysical behaviour of BSA on binding with ZnO nanoparticles in aqueous solution and a layer-by-layer self-assembled film. BSA molecules formed a regimented network in the layer- by-layer film linked with the ZnO nanoparticles [197]. Polyethylimine modified ZnO bind with BSA through stronger electrostatic interaction than uncapped ZnO nanoparticles obtained via sol-gel route where hydrophobic forces were prominent. The structure, stability and activity of BSA was consistent even after the PEI-ZnO binding, whereas the structural deformations accompanied with the uncapped sample reveals the hydrophobic interactions [198]. Similarly, 3-mercaptopropionic

acid (3-MPA) coated ZnO nanoparticles exhibited effective binding with BSA with no significant structural perturbation than bare ZnO [199]. Furthermore, Raman spectroscopy was employed to investigate the ZnO-BSA interactions by Rasa Žūkienė and ValentinasSnitka [200].A.E. Ledesma et.al has introduced the approach of *In-silco* docking studies to investigate the interactions in BSA and ZnO nanoparticles, for the first time ZnO clusters were generated to model the nanoparticles [201].

1.12.   Present Investigation

"Each of us is a unique strand in the intricate web of life and here to make a contribution."

Deepak Chopra

Being versatile and benign material, biogenic/green synthesis of ZnO nanoparticles, characterization and its environmental and biological applications is the matter of our present study. Accounting the benefits and need to promote green synthesis routes, ZnO nanoparticles is prepared by using the plant extracts including the citrus lemon extract, *Abelmoschus esculents* mucilage and *Gliricidia sepium* leaf extract. These bio-sources are inexpensive, renewable, biodegradable, non-toxic and available in plenty in our locality in the state of Kerala, India. Thus, the synthesis route of ZnO becomes cost-effective, facile and apposite for large-scale production. Lemon juice which contains citric acid (CA) as major component forming soluble and stable complex with zinc in solvents like ethylene glycol. Whereas, mucilage is a thick and slimy hydrocolloid, which is a common constituent present in plants, where it is highly soluble in water with inherent viscosity, plasticity, and elasticity. The okra mucilage contains proteins, carbohydrates, polysaccharides, minerals, polyphenols, and flavanol derivatives. These secondary metabolites can easily make complex with the Zn^{2+} ion. Likewise, *Gliricidia sepium* leaf extract is also rich in the phytochemical profile

including alkaloids, flavonoids, polyphenols, saponins and tannins. We investigate the antidiabetic activity (α-amylase and α-glucosidase inhibition), interaction with BSA, photocatalytic activity (photodegradation under UV and Sun light), anti-bacterial activity and thermoluminescence property of the ZnO nanoparticles prepared by using these plant extracts. Also, we attempt to generate some docking models on BSA, α-amylase and α-glucosidase interaction with ZnO nanoparticles using computational simulations.

Reference

1.   S. TaghaviFardood, A. Ramazani, J. Nanostruct., 2016, 6, 167.

2.   S. TaghaviFardood, A. Ramazani, S. Moradi, J. Sol-Gel Sci. Technol., 2017, 82, 432.

3.   F. Sadri, A. Ramazani, H. Ahankar, S. TaghaviFardood, P. AzimzadehAsiabi, M. Khoobi, S.W. Joo, N. Dayyani, J. Nanostruct., 2016, 6, 264.

4.   B. Zeynizadeh, M. Karimkoshteh, J. Nanostruct. Chem., 2013, 3, 57.

5.   V.V. Gawade, N.L. Gavade, H.M. Shinde, S.B. Babar, A.N. Kadam, K.M. Garadkar, J. Mater. Sci. Mater. Electron., 2017, 28, 14033.

6.   S.T. Fardood, A. Ramazani, S. Moradi, P.A. Asiabi, J. Mater. Sci. Mater. Electron., 2017, 28, 13596.

7.   A.R. Prasad, M. Anagha,K.O. Shamsheera, Abraham Joseph, NJC., 2020, 44, 8273.

8.   A.R. Prasad, P.R. Ammal, A. Joseph, Mater. Res. Bull., 2018, 102, 116.

9.   J. Singh, T. Dutta, K.H. Kim, M. Rawat, P. Samddar, P. Kumar, J. Nanobiotechnol., 2018, 16, 84.

10.   C. Vidya, S. Hiremath, M.N.Chandraprabha, I. Venugopal, A. Jain, K. Bansal, Int J CurrEng Technol., 2013, 1,118.

11.   S. Iravani, Int Sch Res Not., 2014, 2014,1.

12.   K.N. Thakkar, S.S. Mhatre, R.Y. Parikh,Nanomed NanotechnolBiol Med., 2010, 6,257.

13.   P. Mohanpuria, N.K. Rana, S.K. Yadav, J Nanoparticle Res., 2008, 10, 507.

14. K.B. Narayanan, N. Sakthivel, J Hazard Mater., 2011, 189, 519.

15. M. Doble, A.K.Kruthiventi, Green chemistry and engineering. Cambridge: Academic Press; 2007.

16. L.P. Silva, I.G. Reis, C.C.Bonatto, Green Processes for Nanotechnology, edited by V.A. Basiuk, E.V. Basiuk, Springer International Publishing Switzerland 2015.

17. O.V. Kharissova, H.V.R. Dias, B.I. Kharisov, B.O. Pérez, V.M. JiménezPérez,Trends Biotechnol., 2013, 31,240.

18. M. Rai, A. Yadav, A.Gade, Crit Rev Biotechnol., 2008, 28, 277.

19. A.D. Dwivedi, K. Gopal, Colloids Surf APhysicochemEng Asp., 2010, 369,27.

20. H. Morkoç, Ü.Özgur, Zinc Oxide: Fundamentals, Materials and Device Technology., 2009, WILEY-VCH Verlag GmbH & Co. KGaA, Weinheim, ISBN: 978-3-527-40813-9.

21. S. Fujihara, H. Naito, T. Kimura, Thin Solid Films, 2001, 389, 227.

22. F.A. Sigoli, M.R. Davolos, M. Jafelicci, J. Alloys Compd., 1997, 262, 292.

23. J.Y. Park, D.E. Song, S.S. Kim, Nanotechnology, 2008, 19, 105503.

24. R. Landsiedel, L. Ma-Hock, B. Van Ravenzwaay, M. Schulz, K. Wiench, S. Champ, S. Schulte, W. Wohlleben, F. Oesch, Nanotoxicology, 2010, 4, 364.

25. T. Li, X. Hu, C. Liu, C. Tang, X. Wang, S. Luo, J. Mol. Catal. A., 2016, 425, 124.

26. S. Gunalan, R. Sivaraj, V. Rajendran, Prog. Nat. Sci: Mater., 2012, 22, 693.

27. P. Vanathi, P. Rajiv, S. Narendhran, S. Rajeshwari, P. K. S. M. Rahman, R. Venckatesh, Mater. Lett., 2014, 134, 13.

28. M. Anbuvannan, M. Ramesh, G. Viruthagiri, N. Shanmugam, N. Kannadasan, Mater. Sci. Semicond. Process., 2015, 39, 621.

29. B. N. Patil, T. C. Taranath, Int. J. Mycobacteriol., 2016, 5, 197.

30. V. N. Kalpana, V. Devi Rajeswari, Bioinorg. Chem. Appl., 2018, 2018, 3569758.

31. A. R. Prasad, S. M. Basheer, L. Williams, A. Joseph, Int. J. Biol. Macromol. 2019, 139, 712.

32. N. Matinise, X.G. Fuku, K. Kaviyarasu, N. Mayedwa, M. Maaza, Appl. Surf. Sci., 2017, 406, 339.

33. Ü. Özgür, Y.I. Alivov, C. Liu, A. Teke, M.A. Reshchikov, S. Dǒgan, V. Avrutin, S.J. Cho, H. Morkoc, J. Appl. Phys. 2005, 98, 041301.

34. B. Ludi, M. Niederberger, Dalton Trans. 2013, 42, 12554.

35. A.K. Radzimska, T. Jesionowski, Materials, 2014, 7, 2833.

36. Z.L. Wang, J. Phys. Condens. Matter., 2004, 16, R829.

37. M.D. Hernández-Alonso, F. Fresno, S. Suárez, J.M. Coronado, Energy Environ. Sci., 2009, 2, 1231.

38. C. Tian, Q. Zhang, A. Wu, M. Jiang, Z. Liang, B. Jiang, H. Fu, Chem. Commun., 2012, 48,2858.

39. M. Premanathan, K. Karthikeyan, K. Jeyasubramanian, G. Manivannan, Nanomedicine, 2011, 7, 184.

40. H.M. Xiong, Adv. Mater., 2013, 25, 5329.

41. B. Malaikozhundan, B. Vaseeharan, S. Vijayakumar, K. Pandiselvi, M.R. Kalanjiam, K. Murugan, G. Benelli, Microb. Pathog., 2017, 104, 268.

42. S. Vijayakumar, B. Vaseeharan, B. Malaikozhundan, M. Shobiya,Biomed. Pharmacother., 2016, 84, 1213.

43. A.R. Prasad, J. Garvasis, S.K. Oruvil, A. Joseph, J. Phys. Chem. Solids., 2019, 127, 265.

44. N. Bala, S. Saha, M. Chakraborty, M. Maiti, S. Das, R. Basu, P. Nandy, RSC Adv., 2015, 5, 4993.

45. H.M. Xiong, Adv Mater Weinheim., 2013, 25, 5329.

46. G.K. Prashanth, P.A. Prashanth, B.M. Nagabhushana, S. Ananda, G.M. Krishnaiah, H.G. Nagendra, H.M. Sathyananda, C. Rajendra Singh, S. Yogisha, S. Anand, Y. Tejabhiram, Artif Cells Nanomed. Biotechnol., 2018, 46, 968.

47. Q. Zhong, J. Tian, T. Liu, Z. Guo, S. Ding, H. Li, Mater. Lett., 2018, 212, 58.

48. Y. Wang, X. Xiao, H. Xue, H. Pang, Chemistry Select, 2018, 3, 55.

49. A. R. Prasad, S. M. Basheer, I. R. Gupta, K.K. Elyas, A. Joseph, Mater. Chem. Phys. 2020, 240, 122115.

50.   A. Maleki, A. H. Mahvi, R. Ebrahimi, Y. Zandsalimi, Korean J. Chem. Eng., 2010, 27, 1805.

51.   F. Gholami-Borujeni, A.H. Mahvi, S. Naseri, M.A. Faramarzi, R. Nabizadeh, M. Alimohammadi, Res. J. Chem. Environ., 2011, 15, 217.

52.   S.D. Ashra, S. Rezaei, H. Forootanfar, A.H. Mahvi and M.A. Faramarzi, Int. Biodeterior. Biodegrad., 2013, 85, 173.

53.   M. Shirmardi, A.H. Mahvi, B. Hashemzadeh, A. Naeimabadi, G. Hassani, M.V. Niri, Korean J. Chem. Eng., 2013, 30, 1603.

54.   A. Srinivasan, T. Viraraghavan, J. Environ. Manage., 2010, 91, 1915.

55.   A.R. Prasad, A. Joseph, RSC Adv., 2017, 7, 20960.

56.   V.K. Garg, M. Amita, R. Kumar, R. Gupta, Dyes Pigm., 2004, 63, 243.

57.   H. Sun, L. Cao, L. Lu, Nano Res., 2011, 4, 550.

58.   K. Hunger, Industrial Dyes: Chemistry, Properties, Applications, Wiley-VCH, Weinheim, Germany, 2003.

59.   R.M. Christie, Environmental Aspects of Textile Dyeing, Woodhead Publishing, Great Abington, Cambridge, 2007.

60.   F.I. Hai, K. Yamamoto, K. Fukushi, Crit. Rev. Environ. Sci. Technol., 2007, 37, 315.

61.   Q. Husain, Crit. Rev. Biotechnol., 2006, 26, 201.

62.   A. Dalvand, R. Nabizadeh, M. RezaGanjali, M. Khoobi, S. Nazmara, A. HosseinMahvi, M. Shanehsaz, S. Seidi, Y. Ghorbani, S.M.R. Shoja, S. Rouhani, J. Magn. Magn. Mater., 2016, 404, 179.

63.   S. Maryam, S. Shahram, G. Yousefali, M. R. S. Seyed, R. Shohre, Spectrochim. Acta, Part A, 2015, 149, 481.

64.   S. Bhatia, N. Verma, Mater. Res. Bull., 2017, 95, 468.

65.   Y. Wang, Y. He, T. Li, J. Cai, M. Luo, L. Zhao, Catal. Commun., 2012, 18, 161.

66.   S. Song, Z.W. Liu, Z.Q. He, A.L. Zhang, J.M. Chen, Y.P. Yang, X.H. Xu, Environ. Sci. Technol., 2010, 44, 3913.

67.   Y.J. Jang, C. Simer, T. Ohm, Mater. Res. Bull., 2006, 41, 67.

68.   C.W. Tang, Mod. Res. Catal., 2013, 2, 19.

69.   M.H. Huang, S. Mao, H. Feick, Science, 2001, 292, 1897.

70.   X.Y. Kong, Z.L. Wang, Nano Lett., 2003, 3, 1625.

71.   Y. Tak, K. Yong, J. Phys. Chem. B, 2005, 109, 19263.

72.   X.D. Wang, C.J. Summers, Z.L. Wang, Nano Lett., 2004, 4, 423.

73.   S. E. Burruel-Ibarra, C. Cruz-Vázquez, R. Bernal, J. R. Martínez-Castelo, A. R. García Haro, V. R. Orante-Barrón, Mater Sci Forum., 2013, 755, 139.

74.   R. Chen, S.W.S. McKeever: Theory of Thermoluminescence and Related Phenomena, World Scientific, Singapore, 1997.

75.   N.S. Chang, J.I. Lee, J. L. Kim, M. Aeoh, K.S. Chung, Journal of radiation protection, 2009, 34 (4), 155.

76.   T.K. Jana, S.K. Maji, A. Pal, R.P. Maiti, T.K. Dolai, K. Chatterjee, J. Colloid Sci., 2016, 480,9.

77.   A. Ghosh, A. Mondal, Mater. Lett., 2016, 164, 221.

78.   L. Wang, G. Tian, Y. Chen, Y. Xiao, H. Fu, Nanoscale, 2016, 8, 9366.

79.   E. Zare, S. Pourseyedi, M. Khatami, E. Darezereshki, J. Mol. Struct., 2017, 1146, 96.

80.   L. Zhang, Y. Ding, M. Povey, D. York, Prog. Nat. Sci., 2008,18,939.

81.   H.R. Madan, S.C. Sharma, Udayabhanu, D. Suresh, Y.S. Vidya, H. Nagabhushana, H. Rajanaik, K.S. Anantharaju, S.C. Prashantha, P.S. Maiya, Spectrochim. Acta A Mol. Biomol. Spectrosc., 2015, 152, 404.

82.   C. Costa, A. Conte, G.G. Buonocore, M.A. del Nobile, Int. J. Food Microbiol., 2011, 148, 164.

83.   R. Kitture, K.Chordiya, S. Gaware, S. Ghosh, P. A. More, P. Kulkarni, B.A. Chopade, S. N. Kale, J. Nanosci. Nanotechnol.,2015, 15, 4046.

84.   R. D Umrani, K. M Paknikar, Nanomedicine, 2014, 9, 89.

85.   A. Nazarizadeh, S. A. Rezaie, AAPS Pharm.Sci.Tech., 2015, 17, 834.

86.   International Diabetic Federation. IDF diabetes atlas (ExecutiveSummary). Sixth edition (2013) Page 11. ISBN: 2-930229-85-3.

87.   S. Ghosh, M. Ahire, S. Patil, A. Jabgunde, M. Bhat Dusane, B.N. Joshi, K. Pardesi, S. Jachak, D.D. Dhavale, B.A. Chopade, Evid.-Based Complementary Altern. Med. 2012, 2012, 929051.

88.   S.P. Sanap, S. Ghosh, A.M. Jabgunde, R.V. Pinjari, S.P. Gejji, S. Singh, B.A. Chopade, D.D. Dhavale, *Org*. Biomol. *Chem*., 2010, 8, 3307.

89.   S.S. Nair, V. Kavrekar, A. Mishra, Euro J Exp Bio., 2013, 3, 128.

90.   A.J. Krentz, C.J. Baile, Drugs, 2005, 65, 385.

91.   D. Rehana, D. Mahendiran, R.S. Kumar, A.K. Rahiman,Bioprocess BiosystEng, 2017, 40, 943.

92.   A. Sathya, P. Siddhuraju, Asian Pac J.Trop., 2012, 5, 757.

93.   I.C. Wells, Can. J. Physiol. Pharmacol., 2008, 86, 16.

94.   M. Muralisankar, S.M. Basheer, J. Haribabu, N.S.P. Bhuvanesh, R. Karvembu, A. Sreekanth, Inorg. Chim. Acta, 2017, 466, 61.

95.   K. Jeyalakshmi, Y. Arun, N.S.P. Bhuvanesh, P.T. Perumal, A. Sreekanth, R. Karvembu, Inorg. Chem. Front., 2015, 2, 780.

96.   S.R. Saptarshi, A. Duschl, A.L. Lopata, J. Nanobiotechnol., 2013, 11, 26.

97.   A. Bhogalea, N. Patel, P. Sarpotdar, J. Mariam, P.M. Dongre, A. Miotell, D. C. Kothari, Colloids Surfaces B Biointerfaces, 2013, 102, 257.

98.   Y.Z. Zhang, B. Zhou, Y.X. Liu, C.X. Zhou, X.L. Ding, Y. Liu, J. Fluoresc., 2018, 18, 109.

99.   R.E. Oslon, D.D. Christ, Annu. Rep. Med. Chem., 1996, 31, 327.

100.   B. Friedrichs, Th. Peters, Jr.: All about Albumin. Biochemistry, Genetics, and Medical Applications., Academic Press, New York, 1996.

101.   K.A. Majorek, P.J. Porebski, A. Dayal, M.D. Zimmerman, K. Jablonska, A. J. Stewart, M. Chruszcz, W. Minor, Mol. Immunol., 2012, 52, 174.

102.   R. Zhou, T.Weikl, Y. Ma, Nanoscale, 2020,12, 10426.

103.   S.M.H. Akhter, Z. Mahmood, S. Ahmad, F. Mohammad, Bio.NanoScience., 2018, 8, 811.

104.   T. Karnan, S.A.S. Selvakumar, J. Mol. Struct., 2016, 1125, 358.

105.   S. Sharma, Optik, 2016, 127, 6498.

106.   S. Ambika, M. Sundrarajan, J. Photochem. Photobiol., 2015, 146, 52.

107.   S. Jafarirad, M. Mehrabi, B. Divband, M. Kosari-Nasab, Mater. Sci. Eng. C, 2016, 59, 296.

108. N. Supraja, T. Prasad, T.G. Krishna, E. David, Appl. Nanosci., 2016, 6, 581.

109. D. Sharma, M.I. Sabela, S. Kanchi, P.S. Mdluli, G. Singh, T.A. Stenström, K. Bisetty, J. Photochem. Photobiol. B Biol., 2016, 162, 199.

110. S.R Senthilkumar, T. sivakumar, Int J Pharm Pharm Sci., 2014, 6, 461.

111. S. Vijayakumar, G. Vinoj, B. Malaikozhundan, S. Shanthi, B. Vaseeharan, Spectrochim. Acta A Mol. Biomol. Spectrosc., 2015, 137, 886.

112. R. Dobrucka, J. Długaszewska, Saudi J. Biol. Sci., 2016, 23, 517.

113. K. Ali, S. Dwivedi, A. Azam, Q. Saquib, M.S. Al-Said, A.A. Alkhedhairy, J. Musarrata, J. Colloid Interface Sci., 2016, 472, 145.

114. T. Karnan, S.A.S. Selvakumar, J. Mol. Struct., 2016, 1125, 358.

115. K. Elumalai, S. Velmurugan, Appl. Surf. Sci., 2015, 345, 329.

116. P.C. Nagajyothi, S. Ju, I. Jun, T.V.M. Sreekanth, K. Joong, H. Mook, J. Photochem. Photobiol. B, 2015, 146, 10.

117. S. Azizi, R. Mohamad, A. Bahadoran, S. Bayat, R.A. Rahim, A. Ariff, W.Z. Saadh, J. Photochem. Photobiol. B Biol., 2016, 161, 441.

118. P. Thatoi, R.G. Kerry, S. Gouda, G. Das, K. Pramanik, H. Thatoi, J. K. Patrad, J. Photochem. Photobiol. B Biol., 2016, 163, 311.

119. J. Fowsiya, G. Madhumitha, N.A. Al-dhabi, M. Valan, J. Photochem. Photobiol. B, 2016, 162, 395.

120. M. Ramesh, M. Anbuvannan, G. Viruthagiri, Spectrochim. Acta A Mol. Biomol. Spectrosc., 2015, 136, 864.

121. N.A. Samat, R.M. Nor, Ceram. Int., 2103, 39, 1.

122. D. Suresh, R.M. Shobharani, P.C. Nethravathi, M.A.P. Kumar, H. Nagabhushana, S.C. Sharma, Spectrochim. Acta A Mol. Biomol. Spectrosc., 2015, 141, 128.

123. K. Elumalai, S. Velmurugan, S. Ravi, V. Kathiravan, S. Ashokkumar, Spectrochim. Acta A Mol. Biomol. Spectrosc., 2015, 143, 158.

124. M. Anbuvannan, M. Ramesh, G. Viruthagiri, N. Shanmugam, N. Kannadasan, Spectrochim. Acta A, 2015, 143, 304.

125. H.R. Madan, S.C. Sharma, D. Suresh Udayabhanu, Y.S. Vidya, H. Nagabhushana, H. Rajanaik, K.S. Anantharaju, S.C. Prashantha, P.S Maiyai,Spectrochim. Acta A Mol. Biomol. Spectrosc., 2016, 152, 404.

126. S.S.M. Hassan, H.I. Abdel-Shafy, M.S.M. Mansour, Arab. J. Chem., 2106, 12, 4074.

127. J.W. Rasmussen, E. Martinez, P. Louka, D.G. Wingett, Expert Opin Drug Deliv., 2010, 7, 1063.

128. R. Rathnasamy, P. Thangasamy, R. Thangamuthu, S. Sampath, V. Alagan, J Mater Sci: Mater Electron., 2017, 28, 10374.

129. C. Vidya, M.N. Chandra Prabha, M.A.L. Antony Raj, Environ. Nanotechnol. Monit. Manag.,2016, 6, 134.

130. M. Aminuzzaman, L.P. Ying, W.S. Goh, A. Watanabe, Bull. Mater. Sci., 2018, 41,0050.

131. C. Anupama, A. Kaphle, Udayabhanu, G. Nagaraju, J. Mater. Sci.: Mater. Electron., 2018, 29, 4238.

132. T. Bhuyan, K. Mishra, M. Khanuja, R. Prasad, A. Varma, Mater. Sci. Semicond. Process., 2015, 32, 55.

133. M.H. Kahsay, A. Tadesse, D. RamaDevi, N. Belachew, K. Basavaiah, RSC Adv., 2019, 9, 36967.

134. H.Y. Chai, S.M. Lam, J.C. Sin, Mater. Lett., 2019, 242, 103.

135. L. Chen, I. Batjikh, J. Hurh, Y. Han, Y. Huo, H. Ali, J.F. Li, E.J. Rupa, J. C. Ahn, R. Mathiyalagan, D.C. Yang, Optik, 2019, 184, 324.

136. N. Elavarasan, K. Kokila, G. Inbasekar, V. Sujatha, Res Chem Intermed., 2017, 43, 3361.

137. K. Elumalai, S. Velmurugan, S. Ravi, V. Kathiravan, G.A. Raj, Adv. Powder Technol., 2015, 26, 1639.

138. L. Fu, Z. Fu, Ceram. Int., 2015, 41, 2492.

139. V.V. Gawade, N.L. Gavade, H.M. Shinde, S.B. Babar, A.N. Kadam, K.M. Garadkar, J. Mater. Sci: Mater. Electron., 2017, 28, 14033.

140. S.S.M. Hassan, W.I. M. El Azab, H.R. Ali, M.S.M Mansour, Adv. Nat. Sci.: Nanosci. Nanotechnol., 2015, 6, 045012.

141. O.K. Hee, E.J. Rupa, G. Anandapadmanaban, M. Chokkalingam, J.F. Li, J. Markus, V. Soshnikova, Z.E.J. Perez, D.C. Yang, Optik, 2019, 181, 1091.

142. R. Ishwarya, B. Vaseeharan, S. Kalyani, B. Banumathi, M. Govindarajan, N.S. Alharbi, S. Kadaikunnan, M.N. Al-anbr, J.M. Khaled, G. Benelli, J. Photoch. Photobio B, 2018, 178, 249.

143. K.C. Lalithambika, A. Thayumanavan, K. Ravichandran, S. Sriram, J.Mater Sci: Mater Electron., 2017, 28, 2062.

144. J. Lu, I. Batjikh, J. Hurh, Y. Han, H.Ali, R. Mathiyalagan, C. Ling, J.C. Ahn, D.C. Yang, Optik, 2019,182, 980.

145. G. Madhumitha, J. Fowsiya, N. Gupta, A. Kumar, M. Singh, J. Phys. Chem. Solids., 2019, 127, 43.

146. P.C. Nethravathi, G.S. Shruthi, D.Suresh, Udayabhanu, H. Nagabhushana, S.C. Sharma, Ceram. Int., 2015, 47, 8680.

147. N.S. Pavithra, K. Lingaraj, G.K. Raghu, G. Nagaraju, Spectrochim. Acta A Mol. Biomol. Spectrosc., 2017, 185, 11.

148. A. Raja, S. Ashokkumar, R.P. Marthandam, J. Jayachandiran, C.P. Kathiwada, K. Kaviyarasu, R.G. Raman, M. Swaminathan, J. Photoch. Photobio. B, 2018, 181, 53.

149. E.J. Rupa, G. Anandapadmanaban, R. Mathiyalagan, D.C.Yang, Optik, 2018, 172, 1179.

150. V.S. Saraswathi, J. Tatsugi, P.K. Shin, K. Santhakumar, J. Photoch. Photobio. B., 2017, 167, 89.

151. E.S. Mehr, M. Sorbiun, A. Ramazani, S.T. Fardood, J. Mater Sci: Mater Electron., 2018, 29, 13.

152. Y.J. Shim, V. Soshnikova, G. Anandapadmanaban, R. Mathiyalagan, Z.E.J. Perez, J. Markus, Y.J. Kim, V. Castro-Aceituno, D.C. Yang,Optik., 2019, 182, 1015.

153. S.Singh, M. Joshi, P. Panthari, B. Malhotra, A.C. Kharkwal , H. Kharkwal, Nano-Structures & Nano-Objects, 2017, 11,1.

154. S.B. Reddy, B.K. Mandal, Adv. Powder Technol., 2017, 28, 785.

155. M. Sorbiun, E.S. Mehr, A. Ramazani, S.T. Fardood, J Mater Sci: Mater Electron., 2018, 29, 2806.

156. M. Stan, A. Popa, D. Toloman, A. Dehelean, I. Lung, G. Katona, Mater. Sci. Semicond. Process., 2015, 39, 23.

157. D. Suresh, P.C. Nethravathi, Udayabhanu, M.A.P. Kumar, H.R. Naika, H. Nagabhushana, S.C. Sharma, Mater. Sci. Semicond. Process.,2015, 40, 759.

158. D. Suresh, P.C. Nethravathi, Udayabhanu, H. Rajanaika, H. Nagabhushana, S.C. Sharma, Mater. Sci. Semicond. Process.,2015, 31, 446.

159. S.T. Fardood, A. Ramazani, S. Moradi, P.A. Asiabi, J Mater Sci: Mater Electron., 2017, 28, 13596.

160. Udayabhanu, G. Nagaraju, H. Nagabhushana, D. Suresh, C. Anupama, G.K. Raghu, S.C. Sharma, Ceram. Int., 2017, 43, 11656.

161. T. Varadavenkatesan, E. Lyubchik, S. Pai, A. Pugazhendhid, R. Vinayagam, R. Selvaraj, J. Photoch. Photobio. B., 2019, 199, 111621.

162. C. Vidya, C. Manjunatha, M.N. Chandraprabha, M. Rajshekar, A. Raj. M.A. L, J. Environ. Chem. Eng., 2017, 5,3172.

163. M. Zare, K. Namratha, M.S. Thakur, K. Byrappa, Mater. Res. Bull., 2019, 109, 49.

164. A.J. Wang, Q.C. Liao, J.J. Feng, P.P. Zhang, A.Q. Li, J.J. Wang, CrystEng Comm.,2012, 14, 256.

165. S. Karthik, P. Siva, K.S. Balu, R. Suriyaprabha, V. Rajendran, M. Maaza, Adv. Powder Technol., 2017, 28, 3184.

166. M. Murali, C. Mahendra, N. Rajashekar, M. Sudarshana, K. Raveesha, K. Amruthesh, Spectrochim. Acta A Mol. Biomol. Spectrosc., 2017, 179, 104.

167. K. Elumalai, S. Velmurugan, S. Ravi, V. Kathiravan, S. Ashokkumar, Mater. Sci. Semicond. Process.,2015, 34, 365.

168. K. Lingaraju, H.R. Naika, K. Manjunath, R. Basavaraj, H. Nagabhushana, G. Nagaraju, D. Suresh, Appl. Nanosci.,2016, 6, 703.

169. N.M. Ngoepe, Z. Mbita, M. Mathipa, N. Mketo, B. Ntsendwana, N. Hintsho-Mbita, Ceram. Int., 2018, 44, 16999.

170. S. Vijayakumar, C. Krishnakumar, P. Arulmozhi, S. Mahadevan, N. Parameswari, Microb. pathog., 2018, 116, 44.

171. G. Sharmila, C. Muthukumaran, K. Sandiya, S. Santhiya, R.S. Pradeep, N.M. Kumar, N. Suriyanarayanan, M. Thirumarimurugan, J. Nanostructure Chem.,2018, 8, 293.

172. H. Padalia, S. Baluja, S. Chanda, BioNanoScience., 2017, 7, 40.

173. N. Senthilkumar, E. Nandhakumar, P. Priya, D. Soni, M. Vimalan, I.V. Potheher, New J. Chem., 2017, 41, 10347.

174. A. J. Reddy, M.K. Kokila, H. Nagabhushana, J.L. Rao, C. Shivakumara, B.M. Nagabhushana, R.P. Chakradhar, Spectrochim Acta A., 2011, 81, 59.

175. V.R. Orante-Barrón, F.M. Escobar-Ochoa, C. Cruz-Vázquez, R. Bernal, J. Nanomater.,2015.

176. A.J Reddy, R.H Krishna, B.M. Nagabhushana , M.K. Kokila , H. Nagabhushana , C. Shivakumara , R.P.S. Chakradhar, Spectrochim Acta A., 2015, 139, 262.

177. H.A. Borbo´n-Nun˜ez, J.L. Iriqui-Razcon, C. Cruz-Vazquez, R. Bernal, C. Furetta , V. Chernov , V.M. Castano, J. Mater Sci., 2017, 52,5208.

178. A.F. Soares, S.H. Tatumi, T.M. Mazzo, R.R. Rocca, L.C. Courrol, J. Lumin., 2017, 186, 135.

179. N. Pushpa, M.K. Kokila, Journal of luminescence.,2017, 190, 100.

180. A.J. Reddy, M.K. Kokila , H. Nagabhushana, S.C. Sharma, J.L. Rao , C. Shivakumara , B.M. Nagabhushana , R.P.S. Chakradhar, Mater Chem Phys.,2012, 133, 876.

181. M. Mazhdi, J. Saydia, M. Karimi, J. Seidi, F. Mazhdi, Optik.,2013 124, 4128.

182. N. Pushpa, M.K. Kokila, K.R. Nagabhushana, Nucl. Instrum. Methods Phys. Res., B., 2016, 379, 62.

183. U. Pal, R. Meléndrez, V. Chernov, M. Barboza-Flores, Appl Phys Lett.,2006, 89, 183118.

184. C. Cruz-Vázqueza, H.A. Borbón-Nuñeza, R. Bernalb, J.A. Gaspar-Armentab, V.M. Castaño, Radiat Eff Defect S.,2014, 169, 380.

185. N.R. Panda, B.S. Acharya, T.B. Singh, R.K. Gartia, Mater. Lett.,2013, 95, 205.

186. M. Isika, N.M. Gasanly, Ceram.,2018, 44, 13929.

187. Larisa Grigorjeva, A. Zolotarjovs, S.Y. Sokovnin, D. Millers , K. Smits , V. G. Ilves, Ceram.,2017, 43, 6187.

188. I.C. Wells, J. Physiol. Pharmacol., 2008, 86, 16.

189. V. Vinotha, A. Iswarya, R. Thaya, M. Govindarajan, N.S. Alharbie, S. Kadaikunnane, J.M. Khalede, M.N. Al-Anbr, B. Vaseeharan, J. Photoch. Photobio B., 2019, 197,111541.

190. D. Rehana, D. Mahendiran, R.S. Kumar, A.K. Rahiman, Bioprocess Biosyst Eng., 2017, 40, 957.

191. G. Rajakumar, M. Thiruvengadam, G. Mydhili, T. Gomathi, I.M. Chung, Bioprocess Biosyst Eng.,2018, 41,21.

192. A. Bayrami, S. Alioghlia, S.R. Pouran, A.H. Yangjeh, A. Khataeed, S. Ramesh, Ultrason. Sonochem.,2019, 55, 57.

193. H.R. Rajabi, A. Naghiha, M. Kheirizdeh, H. Sadatfaraji, A. Mirzaei, Z. M Alvand, Mater. Sci. Eng. C., 2017, 78, 1109.

194. Y. Song, J. Wang, X.K. Li, L. Cai, Bio. Metals., 2005, 18, 325.

195. A. Kathiravan, G. Paramaguru, R. Renganathan, J. Mol. Struct.,2009, 934, 129.

196. P. Kumar, P. Kumar, A. Deep, L. M. Bharadwaj, Appl. Nanosci.,2013, 3,141.

197. C. Hansda, P. Maiti, T. Singha, M. Pal, S. A. Hussain, S. Paul, P. K. Paul, J Phys Chem Solids., 2018,121,110.

198. S. Chakraborti, P. Joshi, D. Chakravarty, V. Shanker, Z. A. Ansari, S. P. Singh, P. Chakrabarti, Langmuir., 2012, 28,11142.

199. G. Simonelli, E.L. Arancibia, J. Mol. Liq.,2015, 211,742.

200. R. Žūkienė, V.Snitka, Colloids Surf. B., 2015, 135,316.

201. A.E. Ledesma, D.M. Chemes, M. de los Angeles Frías, M.D. Torres, Appl Surf Sci., 2017, 412, 177.

Review

Applications of phytogenic ZnO nanoparticles: A review on recent advancements

Anupama R. Prasad [a], Linda Williams [a], Julia Garvasis [a], K.O. Shamsheera [a], Sabeel M. Basheer [b], Mathew Kuruvilla [c], Abraham Joseph [a] ☒

Show more ⌄

+ Add to Mendeley   ⋄ Share   ❞ Cite

Get rights and content

Highlights

- The green synthesis of nanoparticles is highly encouraged during the past few decades.

- Phytogenic nanoparticles have preference due to great diversity, safe,

Various physical and chemical methods are employed to synthesise nanoparticles are becoming tedious, exorbitant, catastrophic affecting the flora and fauna adversely. Enormous attention was received on green strategies which minimizes or completely eliminate chemical byproducts, employs less hazardous chemicals, environmentally benign solvents and renewable precursors. The use of plant extracts as reducing agents and stabilizers in nano synthesis got wide acceptance. Here, ZnO nanoparticles is prepared by using the plant extracts including the citrus lemon extract, *Abelmoschus esculents* mucilage and *Gliricidia sepium* leaf extract.

Chapter 2
Materials and Methods

"Observation, reason and experiment make up what we call the scientific method."

Richard P. Feynman
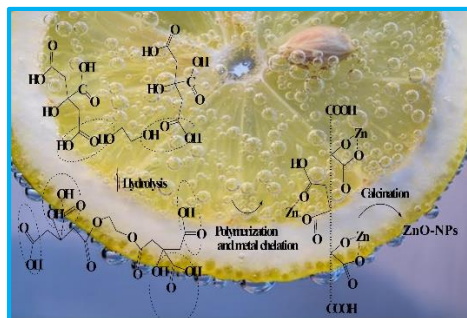
2.1. Synthesis of ZnO nanoparticles using *Citrus lemon* extract

Zinc acetate $Zn(OOCCH_3)_2(H_2O)_2$, (98%) and ethylene glycol (99%) was obtained from Merk Pvt. Ltd and used as obtained. Fresh lemon fruits were collected from local market. Scheme: I represent the pictorial representation of synthesis route.
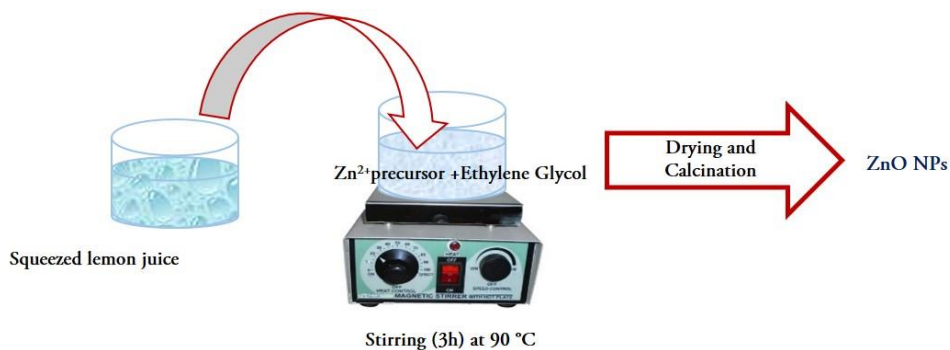
Scheme: I. Synthesis of ZnO nanoparticles uing citrus lemon extract.

2.5 g of zinc acetate was dissolved in 20 ml of ethylene glycol. Lemon fruits obtained from local market was cleaned, squeezed in to smooth muslin cloth and the solid particles were filtered off. 20ml of clear lemon extract was dropped in to the precursor solution in 1 h with vigorous stirring. The reaction was further conducted for 3 h keeping in 90°C. Resulting suspension was dried and calcined at 300, 500, and 700°C for 2 h to obtain ZnO powder.

2.2. Synthesis of ZnO nanoparticles using *Abelmoschus esculents mucilage*

Zinc acetate dihydrate (98%) was provided by MerkPvt. Ltd and used as obtained. Fresh okra crops were purchased from the local market near Calicut University, Malapuram, Kerala, India. The pictorial representation of the synthesis route is depicted in Scheme: II.
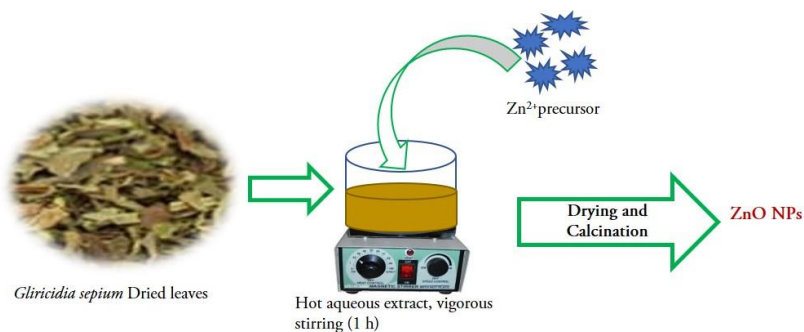
Scheme: II. Synthesis of ZnO nanoparticles using *Abelmoschus esculents* mucilage.

The okra crop was washed thoroughly, chopped into small pieces, and approximately 10 g was soaked overnight in 100 mL of distilled water at room temperature. The okra mucilage was extracted in water and the solution obtained was filtered to obtain the clear viscous mucilage extract, which was diluted with an equal quantity of distilled water. Next, 20 mL of this diluted extract was slowly added to 20 mL of 0.25M zinc acetate solution with vigorous stirring at room temperature. The reaction was conducted for 4 h and the clear mixture was then heated in an air oven at 150°C to obtain a dried mass. The product was calcined at 300, 500, and 700°C for 2 h to obtain ZnO nanoparticles.

2.3. Synthesis of ZnO nanoparticles using *Gliricidia sepium* leaf extract

Zinc acetate dihydrate (98%) was obtained from Merk Pvt. Ltd and used as received. *Gliricidiasepium* leaves were collected from Calicut University campus, Kerala, India. Scheme: III represents the synthesis route.

Scheme: II. Synthesis of ZnO nanoparticles using *Gliricidiasepium* leaf extract.

Fresh leaves of *Gliricidiasepium* leaves were washed with distilled water and shadow dried. The crispy collections were crumbled finely, 3.5g weighed and boiled with 100 ml distilled water for 15 minutes. The solution was cooled and filtered to yield a clear brownish-yellow solution. 25 ml of this prepared extract was taken, diluted to 75 ml, heated to 80°C, kept vigorously stirred and 2.5 g of precursor zinc acetate was added. The reaction was allowed to proceed for an hour resulting in a cloudy yellow solution. This solution was placed in an air oven, dried and powdered to get a fine yellow mass which thereafter subjected to calcination at 300, 500, and 700°C for 2 h ensuing ZnO powder.

2.4. Characterization Techniques

The samples were characterized using different analytical methods. A FT/IR-4100 spectrophotometer (Jasco) and v-550 UV/Vis spectrophotometer (Jasco) were used for fourier transform infrared (FTIR) spectroscopy and UV diffuse reflectance spectroscopy (UV-DRS), respectively. The X-ray diffraction (XRD) pattern of samples was recorded using a diffractometer (2y = 20–901, Cu-Kα radiation; Rigaku). X-ray photoelectron spectroscopy (XPS) was done using PHI 5000 Versa Probe III (Physical Electronics). Field emission

scanning electron microscopy (FESEM) was done using a Zeiss system. High-resolution transmission electron microscopy (HRTEM) was done using a 2100 system (JEOL/JEM) to monitor the morphology and particle dimensions of the material. The average particle size was determined from the selected areas of HRTEM analysed using Gatan Microscopy Suite v3.x (Gatan). Energy dispersive X-ray analysis (EDAX) was performed on the EDAX attachment to the same FESEM instrument.Thermoluminescence was investigated using a TLD-96 setup (Nucleonix). The zeta potential of the sample was measured with a PALS zeta potential analyser, v5.60 (Brookhaven Instruments).

2.4.1. UV-Visible Spectroscopy

UV-Visible spectroscopy is an important technique being frequently used in material characterization and analytical applications. The technique quantitatively measures the absorbed and scattered light from the sample. Since the optical properties of nanoparticles are sensitive towards their morphology, shape, concentration (when measured in solution form), refractive index near the particles surface and state of agglomeration, the UV-Visible spectroscopy is an effective tool for the characterization of nanoparticles. In context of semiconducting metal oxide nanoparticles like ZnO it is essential to determine the optical band gap. The UV-diffuse reflectance spectra (DRS) is commonly used to resolve the band gap which measures the absorbance/ reflectance from the sample in its power form.

2.4.2. FTIR spectroscopy

Infrared or vibrational spectroscopy involves the interaction of matter with IR radiation. During the IR exposure sample selectively absorb the radiation with a particular wavelength. Consequently, the molecules experience a

change in dipole moment and their vibrational energy levels. Thus, each IR absorption peaks are related to the different vibrational modes in a particular molecule. The FTIR spectra is commonly used to determine the molecular structure, analytical experiments, qualitative and quantitative determinations. FTIR characterization of ZnO samples can provide the vibrational mode and the purity and throw light into the actual composition of the material.

2.4.3. XRD analysis

XRD is a non-destructive analytical technique essential to investigate the crystal structure, chemical composition and phase purity of materials. Since, the crystal structure possesses a well-ordered arrangement of composed atoms, the incident X-rays experience repetitive diffraction by constructive interference in accordance with the Braggs' law. XRD patterns are referred as the finger print of a crystalline compound since no two crystals will have identical unit cells, composition of atoms and their position. Powder XRD is used for the materials which cannot be produced in single crystal form.

2.4.4. XPS analysis

X-ray photoelectron spectroscopy is a surface sensitive analytical technique used to detect the elemental composition, chemical state and electronic state of the elements in a particular material. It is alternatively named as 'Electron spectroscopy for chemical analysis (ESCA). XPS works on the principle of photoelectric effect. The electrons emitted from each atom makes corresponding peaks on the XPS spectra at their characteristic energy values. Thus, the intensity and energy values appear in the XPS spectra of the samples facilitate to identify composition and chemical state of elements except hydrogen and helium.

2.4.5. FESEM analysis

FESEM is an electron microscope which is used to produce the surface image of a sample. The sample surface is scanned with the electron beam in Raster patterns (surface get scanned in horizontally and vertically) and the electrons interact with the atoms in the sample to generate signals. Depending on the type of interaction with the sample, the signals are produced as back scattered electrons, secondary electrons, X-rays or light and modern instruments are equipped with multiple detectors. Detection of secondary electrons is the most preferred mode as it can provide images with high-resolution and explore the surfaces below 1nm size. FESEM analysis is frequently conducted to study the morphology, topography and composition of nanomaterials.

2.4.6. EDX analysis

Energy dispersive X-ray analysis (EDX, EDAX or EDS) is the analytical technique used to determine the elemental composition of materials. EDX is usually equipped in attachment to the electron microscopes SEM or TEM. The EDX profile presents the elemental peaks comprising the particular material and the composition of the sample are thus analysed. In addition, elemental mapping and imaging of the samples are also possible with the technique. EDX relies on the X-ray excitation and characteristic X-ray emission from the sample. When source x-rays incident on the sample, the electron from inner shell of an atom at ground state excited and the electron get ejected from the shell leaving an electron hole. An electron from the higher energy level fills this electron hole accompanied by characteristic X-ray emission

2.4.7. HRTEM analysis

TEM is an important tool being used for the characterization of nanomaterials. It belongs to the class of electron microscopy working on the electronic beam transmission through an ultra-thin sample. The transient electron beam interact with the atoms of the material and the transmitted electrons are sensed to provide the image of the sample. The images thus created can be magnified and resolved using a fluorescent or photographic screen. Good quality sensors like CCD cameras are also used for this purpose. Advanced high resolution TEM instruments are available and obviously they can provide a high-resolution image of the sample, in fact we are able to see the atoms. In nanomaterials research   HRTEM micrographs are used to determine the particles size, distribution and morphology of the samples. TEM can provide the selected area electronic diffraction patterns (SAED) ensuing from the elastic scattering of electron beam by the sample lattice satisfying Braggs' law.   The diffraction spots thus obtained can provide the information about the structure and crystallinity of the sample.

2.4.8. Selected area diffraction

Selected area diffraction (SAD or SAED) is a crystallographic technique which is used to identify the crystal structure and crystal defects in materials. The technique is performed inside the TEM system and the selected area diffraction patterns are obtained as a series of spots. Each spot in the SAED pattern represents the diffraction form the lattice planes of corresponding crystal structure.

2.4.9. Zeta potential analyser

Zeta potential value simply gives the indirect assessment of the surface charge of the nanoparticles. It is one of the accessible methods that are used

to study the peripheral characteristics of nanoparticles in solution. The nanoparticle when dispersed in some liquid, if they are charged get surrounded by the oppositely charged ions forming a thin charged layer (Stern layer). The Stern layer is accompanied by a secondary outer layer (diffusive layer) formed by the loosely attached ions. These electrical double layers move in the liquid under the influence of electric field, gravity or kinetic energy a boundary is formed between ions in the diffusive layer and the ions remain in the bulk. The electrostatic potential at this boundary is measured as zeta potential. The zeta potential nanoparticles affect their physical state in solution.

2.4.10. Thermoluminescence measurement

Thermoluminescence is a widely accepted dosimetry technique which measures the amount of pre-absorbed radiation that emitted from a material stimulated by heat. High-performance TL phosphors are being used in various dosimeters. In the typical procedure, ~10mg of the sample is mixed with acetone and allowed to settle as fine grains. The sample is usually deposited on aluminium disks and dried before measurements. The sample column is pre-heated around ~400°C and the whole measurement is conducted in nitrogen atmosphere to minimize the background peaks and other interfering phenomena. After the exposure to the ionizing radiation (gamma in our study) the sample is heated (heating rate 2°C/sec). Since the TL emission is limited to very few centres, generally the phenomenon is weak, sensitive photomultiplier tubes are used as detector. The glow curves are resolved as the variation of output light with temperature.

2.5. Alpha-amylase and Alpha-glucosidase inhibition

Alpha-amylase activity was carried out by DNSA (3,5-dinitrosalicyclic acid) method. 10 µL of α-amylase solution (10 mg/ml) was mixed with 390 µL of phosphate buffer (0.02 M phosphate buffer pH 7.0 containing 0.006 M NaCl, pH 7.0) containing different concentration of nanoparticles. After incubation at 37°C for 10 min, 100 µL of starch solution (1 %) was added, and the mixture was re-incubated for 1 hour. 1 mL of DNSA solution was added, boiled for 5 minute and added 5 ml distilled water, and the absorbance was taken at 565 nm. Sample, substrate and α-amylase blank determinations were carried out under the same reaction conditions. Inhibition of enzyme activity was calculated as

$$(\%) = \frac{(A - C)}{(B - C)} \times 100 \qquad (1)$$

where, A = absorbance of the sample, B = absorbance of blank (without α-amylase), and C = absorbance of control (without starch).

The effect of nanoparticles on α-glucosidase activity was determined according to the method described by Kim et al., using α-glucosidase from Saccharomyces cerevisiae. 200 µL of α-glucosidase (0.067 U/ml) was preincubated with different concentrations of the sample for 10 min. The substrate solution p-nitrophenyl glucopyranoside (pNPG) was prepared in 0.1 M sodium phosphate buffer (pH 6.9). Then 200 µL of 3.0 mM (pNPG) was dissolved in 0.1 M sodium phosphate buffer (pH 6.9) and then added to start the reaction. The reaction mixture was incubated at 37°C for 20 min and stopped by adding 2 ml of 0.1 M Na_2CO_3. The α-glucosidase activity was determined by measuring the yellow-colored paranitrophenol

released from pNPG at 400 nm. The results were expressed as percentage of inhibition.

$$(\%) = \frac{(B - T)}{(B - C)} \times 100 \qquad (2)$$

where, T is the absorbance in the presence of test substance and C is the absorbance of control.

2.6. ZnO-BSA binding studies

Fatty acid free BSA lyophilized powder of 99% purity was obtained from Sigma Aldrich. 10-120μL, solution of ZnO nanoparticles (1mg/10ml) was sequentially added in to 2.5 ml of 1 μM BSA stock solution in phosphate buffer of pH 7.4 and the fluorescence spectra recorded at a fixed excitation wavelength corresponding to BSA at 280 nm in the range of 290–550 nm, using Cary Eclipse Fluorescence Spectrophotometer (PMT voltage: 590 eV). Synchronous fluorescence spectra were also monitored for tryptophan and tyrosine residues in BSA in order to assess the preferential interaction with ZnO nanoparticles.

2.6.1. Spectrofluorometer

Spectrofluorometers operate according to the principle of fluorescence spectroscopy which quantitatively measures the fluorescence properties exhibited by the compounds. The sample is excited with the light source at a particular wavelength and the emitted fluorescence can be measured at another specific wavelength. Florescence spectra is a fast and sensitive analytical method for the characterization of molecular components. The technique is usually used in analytical chemistry to determine the concentration and chemical environment of test samples. In polyatomic

fluorescent samples the fluorophore molecules (mostly contain some aromatic rings, for instance tryptophan, tyrosine etc.) plays the important role. For such complex samples like proteins synchronous fluorescence spectra is often conducted. Here, the spectra are recorded by the simultaneous scanning of excitation and emission monochromators such that we can concurrently analyse the multiple fluorophores in a complex sample. The method provides improved sensitivity without compromising the sensitivity.

2.7. Invitro cytotoxicity determination by MTT assay

Chang liver cell line were initially procured from National Centre for Cell Sciences (NCCS, Pune, India and maintained Dulbecos modified Eagles medium Himedia). The cell line was cultured in 25 cm^2 tissue culture flask with DMEM supplemented with 10% FBS, L-glutamine, sodium bicarbonate and antibiotic solution containing: Penicillin (100U/ml), Streptomycin (100µg/ml), and Amphoteracin B (2.5µg/ml). Cultured cell lines were kept at 37ºC in a humidified 5% CO$_2$ incubator (Galaxy® 170 Eppendorf, Germany).

2.7.1. Cells seeding in 96 well plate

Two days old confluent monolayer of cells were trypsinized and the cells were suspended in 10% growth medium, 100µL cell suspension (5x10^4 cells/well) was seeded in 96 well tissue culture plate and incubated at 37ºC in a humidified 5% CO$_2$ incubator.

2.7.2. Preparation of compound stock

1 mg of each compound was added to 1ml of DMEM and dissolved completely by cyclomixer. After that the extract solution was filtered through 0.22 µm Millipore syringe filter to ensure the sterility.

2.7.3. Cytotoxicity Evaluation

After 24 hours the growth medium was removed, freshly prepared samples in 5% DMEM were five times serially diluted by two fold dilution (6.25μg, 12.5μg, 25μg, 50μg, 100μg in 100μL of 5% MEM) and each concentration of 100μL were added in triplicates to the respective wells and incubated at 37ºC in a humidified 5% CO_2 incubator.

2.7.4. Cytotoxicity effect by MTT Method

Fifteen mg of MTT (Himedia, M-5655) was reconstituted in 3 ml PBS until completely dissolved and sterilized by filter sterilization. After 24 hours of incubation period, the sample content in wells were removed and 3.0μL of reconstituted MTT solution was added to all test and cell control wells, the plate was gently shaken well, then incubated at 37ºC in a humidified 5% CO_2 incubator for 4 hours. After the incubation period, the supernatant was removed and 100μL of MTT solubilisation solution(DMSO) was added and the wells were mixed gently by pipetting up and down in order to solubilise the formazan crystals. The absorbance values were measured by using micro plate reader at a wavelength of 570 nm.

The percentage of growth inhibition was calculated using the formula

$$\%of\ viability = \frac{Mean\ OD\ of\ samples}{Mean\ OD\ of\ controle\ group} \times 100 \qquad (3)$$

2.8. Preparation of molecular docking models

Molecular docking helps to characterize the binding sites of target protein and thus to illustrate the biochemical processes. *In silico* docking studies were carried out using Autodock 4.2 version and the images were viewed in Accelry's Discovery Studio Visualizer version 4.0 and Autodock 4.2

interfaces. The hexagonal wurtzite structure of ZnO obtained from American mineralogical crystal data (AMC) with lattice parameters a ¼ 3.818 Å, b ¼ 3.818 Å and c ¼ 6.260 Å.Three dimensional ZnO crystal structure imitating the nanoparticle curvature was generated using Gauss View 6 and Mercury (3.8 version) packages. The crystal structure of BSA was obtained from RCSB protein data bank (ID: 3V03). The chain A of 3V03 was used for the docking studies. The missing atoms in the crystal structure were repaired using repair command module of Autodock.

The crystal structure of target protein α-glucosidase from S. cerevisiae was still not available in protein data bank. For docking studies, we generated homologous 3-D structure of S. cerevisiae α-glucosidase via computational method. We obtained the target protein sequence from NCBI Gene Bank sequence data base and made a homology of the model with existing mould of PDB ID: 2ze0, which is the protein corresponds to α-glucosidase. The new protein was moulded (or developed) using Easy Modeller 4.0 software. The sequence similarities of constructed model were checked with original protein sequences via p Blast analysis, and found 100% sequence identity over 584 protein length. Further, the stereochemical quality of the model protein was ensured via Ramachandran plot conducted using   SAVES 5.0 programme. The 3D macro-structure of α-amylase was obtained employing homology modelling technique. The amino acid sequence of (*Saccharomyces cerevisiae)* alpha Glucanase (1, 4-alpha-glucan-branching enzyme) (ID: P32775) was obtained from UniProt database. Befitting homologous template structures (4bzy & 5clt) were identified by performing BLASTp (Basic local alignment search tool program). Model of the target protein were generated using protein structure modelling program, GUI based Easy Modeller running Modeller 9.24, and the generated model was furthur validated using webserver PROCHECK and RC (Ramachandran plot) plot was generated.

Prior to docking, the protein structures were modified by deleting the water molecules and by adding polar hydrogen atoms for exact ionization and tautomeric states of amino acid residues and was used for semi flexible docking. United atom charges were realized by assigning Kollman charges and flexible movement of protein structure, ZnO planes were ensured by considering a proper grid volume ($126 \times 126 \times 126$) with 0.37Å grid spacing, covering all its surfaces. In addition, a force field was applied for both the components. Lamarckian Genetic Algorithm was applied and all other default Auto dock parameters were assigned. From all possible models obtained the best one with lowest binding energy represents the most probable binding mode.

2.9. Photodegradation of Organic dyes

Target dye Methylene blue (MB: $C_{16}H_{18}ClN_3S$) and Rhodamine B (RhB: $C_{28}H_{31}ClN_2O_3$) were supplied by Qualigens Pvt. Ltd, India and used as received. Fig.1 depicts the structure of dye molecules.
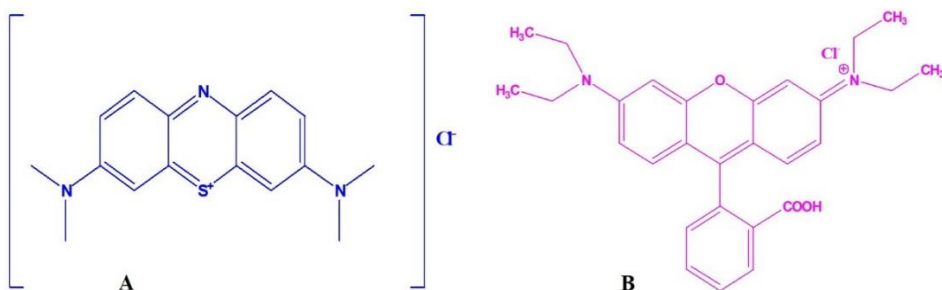
Fig.1. Structure of A) Methylene blue and B) Rhodamine B.

The photodegradation of dyes using ZnO nanoparticles (50 mg) was investigated with (MB) (15ppm) and RhB (10 ppm) dye solutions under UV illumination (Luzchem LZC-4X model photoreactor, ~7300 lux intensity)

and under natural sunlight (76000±100 lux). The reaction medium was kept constantly stirred and in regular intervals fixed, the quantity of dye solutions was retrieved from the ampule. The catalyst was separated by centrifugation and the remained dye concentration was determined by recording the UV absorption spectra. Photocatalytic degradation efficiency was calculated using equation

$$\%Degradation = \frac{A_0 - A}{A_0} \times 100 \qquad (4)$$

where A_0 and A are the initial and final absorbance of dye solution at λ_{max}. The control experiments were carried out under dark conditions to determine the adsorption loss.

2.9.1. Effect of scavengers

Various quenchers were introduced to determine the role of active species involved in the photocatalytic degradation of MB. 0.5 M KI (quencher for holes, h^+, and surface bounded hydroxyl radicals), ethanol (quencher for electron e^-), sodium azide (quencher for oxygen O_2) and isopropyl alcohol (IPA, quencher for hydroxyl radicals, $\cdot OH$), were individually supplied in the reaction medium and studied the photodegradation under direct sunlight.

2.9.2. Recyclability of the photocatalyst

The catalyst was collected after each cycle, thoroughly washed with 1:1 water- acetone mixture, heated to eliminate residual dye molecules if any and re-introduced to the test dye solution. The recycling experiments of ZnO for photocatalytic degradation of methylene blue under sunlight irradiation were carried out for four consecutive cycles.

2.10. Antibacterial activity of ZnO

The target bacterial strains *Klebsiella pneumoniae* MTCC3384, *Staphylococcus aureus* MTCC87 were collected from Microbial Type Culture Collection (MTCC), Chandigarh, India. Antibacterial activity of the sample was evaluated via Agar well diffusion method. Same amount 15-20 ml of Mueller-Hinton agar was allowed to solidify on sterile glass petriplates of identical dimension. Standardized bacterial inoculum was homogenously spread over the solidified agar medium using sterile cotton swab. Four wells with a diameter of 8 mm (20 mm apart from one another) were punched aseptically with a sterile cork borer. The ZnO sample solution (40 and 80 μL) at desired concentrations from the stock solution was added in two of the wells. A positive control (Gentamycine) and the negative control (compound solvent) were introduced in the other two wells. The petri plates were incubated at 37°C for 24 hours. The diameter of zone of inhibition around the wells was measured in mm.

Zinc oxide belongs to this class of II-IV semiconductors possessing a border line ionicity and exhibits three types of crystal structures wurtzite, zinc blend and rock salt. A stable zinc blend structure is feasible only if the crystal grown on a cubic substratum and the rock salt symmetry requires high pressure conditions. The wurtzite ZnO is the thermodynamically most stable crystalline symmetry under ambient conditions. ZnO nanoparticles prepared by using the citrus lemon extract, *Abelmoschus esculents* mucilage and *Gliricidia sepium* leaf extract were characterized using XRD, SAED, FESEM, HRTEM, FTIR, UV-Vis DRS, XPS, EDX and zeta potential analytical techniques.

Chapter 3

Characterization of ZnO nanoparticles synthesized using citrus lemon extract, Abelmoschus esculents mucilage and Gliricidia sepium leaf extract.

"It is important to get results from experiment, but the most important is the process in getting that results."

Dr. Nik Ahmad Nizam

Various analytical techniques were employed to characterize the synthesized ZnO nanoparticles. The surface morphology, size, and shape of the nanoparticles were determined by field emission scanning electron microscopy (FESEM) and high-resolution transmission electron microscopy (HRTEM). Structure, crystallinity and purity of the samples were analysed using X-Ray diffraction (XRD) patterns and Selected area diffraction patterns (SAED). Further, Fourier transform infrared (FTIR) spectra was analysed. Diffuse reflectance spectra (DRS) was recorded to determine the optical band gap of the ZnO nanoparticles. The Elemental and chemical state analysis were performed using an energy dispersive X-ray spectroscopy (EDX) and X-ray photoelectron spectroscopy (XPS). Surface charge of the nanoparticles were determined via zeta potential analysis.

3.1. XRD and SAED analysis

The crystal structure of the samples was confirmed with X-ray diffraction patterns. The X-ray diffraction pattern of ZnO nanoparticles synthesized using *Citrus lemon* extract (ZL), *Abelmoschus esculents* mucilage (ZM), and *Gliricidiasepium* leaf extract (ZG) are depicted in Fig. 1- 3 respectively. Well defined diffraction peaks obtained at 2θ values 31.6°, 34.6°, 36.3°, 47.5°, 56.8°, 62.7°, 66.3°, 67.9°, 69.0°, 72.7° and 77.1° are indexed to the lattice planes (100), (002), (101), (102), (110), (103), (200), (112), (201), (004) and (202) respectively associated to the hexagonal wurtzite ZnO structure in accordance with the JCPDS card No. 36-1451. The patterns with highly intense characteristic peaks especially for the (100), (002) and (101) planes and devoid of any secondary phases indicates crystalline, pure single-phase wurtzite ZnO nanoparticles.

The average crystallite size of the samples was determined using Scherrer formula.

$$D_C = \frac{0.9\lambda}{\beta Cos\theta} \qquad\qquad (1)$$

where D_C is the scattering domain particle size, λ is the wavelength of Cu Kα radiation in Å, β is the full width at half maximum (FWHM) in radian and θ is the Bragg diffraction angle in degree. FWHM was calculated with the most intense peak for the plane (101). The average crystallite size obtained for ZL, ZM, and ZG samples are listed in Table1.
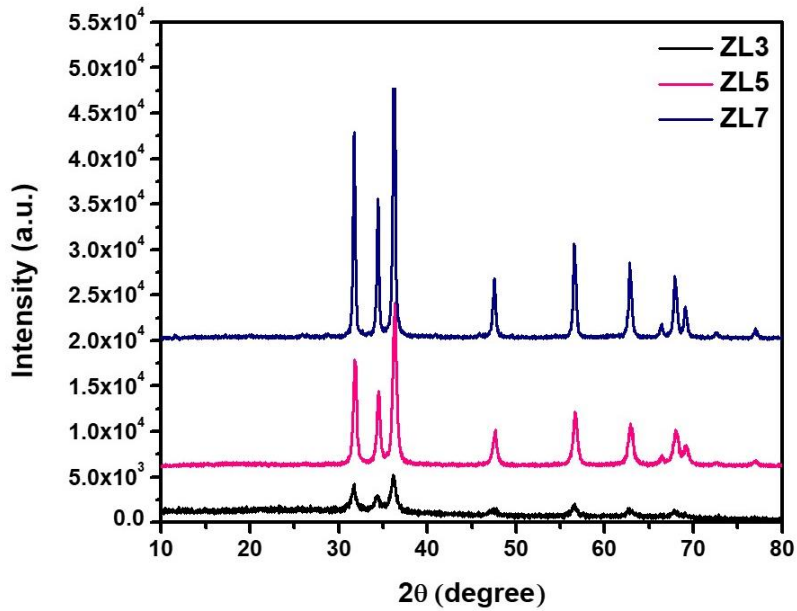
Fig. 1. X-ray diffraction patterns of ZL3, ZL5, and ZL7 ZnO nanoparticles.
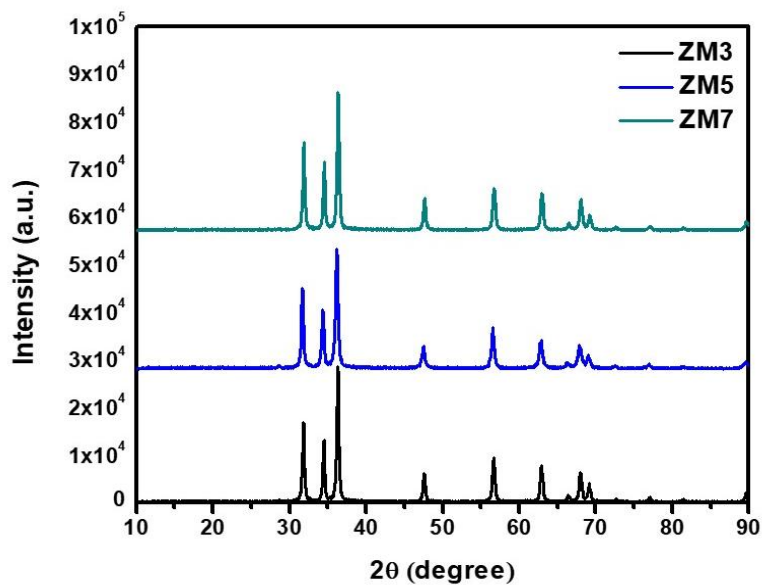
Fig. 2. X-ray diffraction patterns of ZM3, ZM5, and ZM7 ZnO nanoparticles.
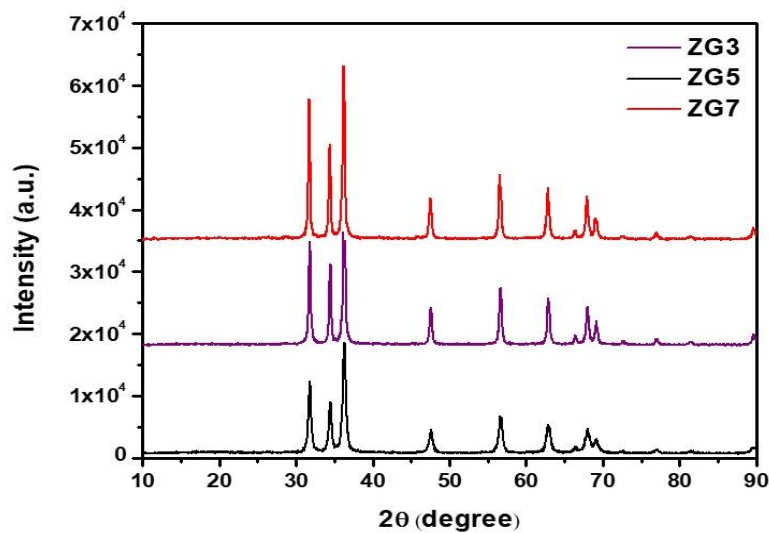
Fig. 3. X-ray diffraction patterns of ZG3, ZG5, and ZG7 ZnO nanoparticles.

Fig. 4-6 represents the SAED patterns of ZL, ZM, and ZG samples respectively. The bright and well-spotted electron diffraction patterns imply the high crystallinity of the nanoparticles obtained [1]. Moreover, spots represent major diffractions in the hexagonal wurtzite structure of ZnO [2]. The X-ray diffraction studies and SAED analysis reveals that the crystallinity of the samples improves with the increase in calcination temperature.
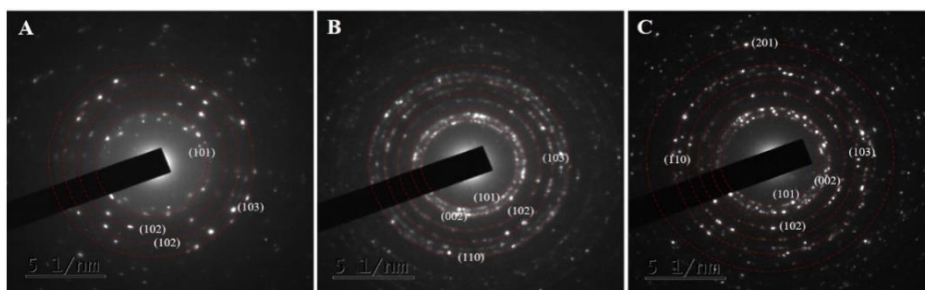
Fig. 4. SAED pattern of ZnO nanoparticles A) ZL3, B) ZL5, and C) ZL7.
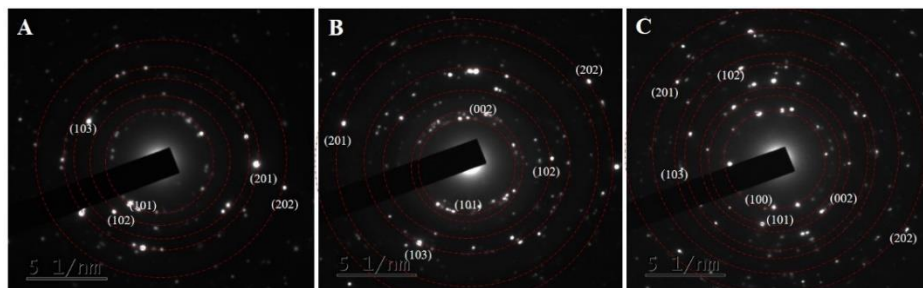
Fig. 5. SAED pattern of ZnO nanoparticles A) ZM3, B) ZM5, and C) ZM7.
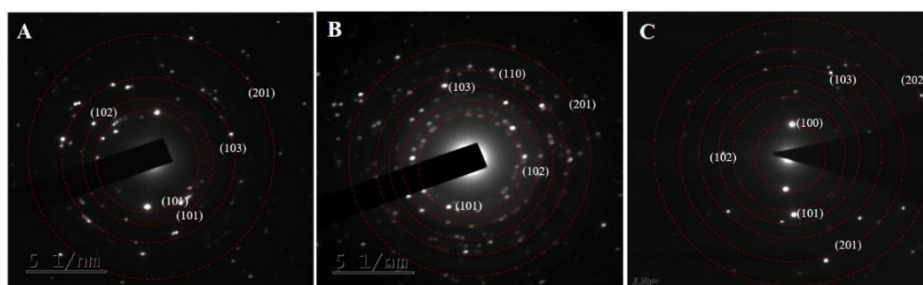
Fig. 6. SAED pattern of ZnO nanoparticles A) ZG3, B) ZG5, and C) ZG7.

Table 1. Average Crystallite size of ZL, ZM, and ZG ZnO nanoparticles calculated from XRD pattern.

No.	Sample	Crystallite size (nm)
1	ZL3	10.78
2	ZL5	13.24
3	ZL7	34.32
4	ZM3	23.20
5	ZM5	20.32
6	ZM7	21.36
7	ZG3	25.66
8	ZG5	30.01
9	ZG7	28.79

3.2. FTIR spectra of ZnO nanoparticles

Structure and purity of ZnO nanoparticles was further confirmed using FTIR spectrum. Fig. 7 shows the FTIR spectra of ZL nanoparticles obtained. The spectra of ZL3 shows characteristic –OH stretching vibrations around 3400 cm^{-1} associated with the surface adsorbed water molecules. Peaks appeared at 1575 cm^{-1} and 1410 cm^{-1} were attributed to the carbonyl vibrations of carboxylate/ester residues owing to the low temperature of calcination. Here the Zn-O characteristic stretching can be observed at ~470 cm^{-1}. The residual peaks are very weak for ZL5 sample and the characteristic Zn-O stretching appeared around 470 cm^{-1}. The spectra of ZL7 is almost devoid of residual peaks and intense characteristic Zn-O vibration appeared around 470 cm^{-1} [3].
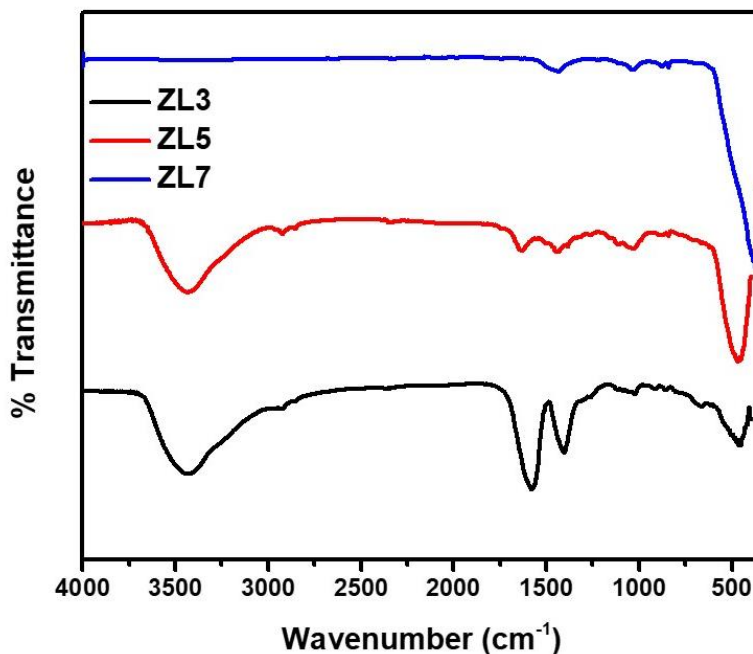
Fig.7. FTIR spectra of ZL3, ZL5, and ZL7 ZnO nanoparticles.

Lemon juice contains 5-6% citric acid in addition to its water content and other components include limonin, vitamin C, flavonoids, folate and minerals [4]. The typical reaction root for the synthesis involves the esterification of citric acid takes place rapidly in presence of ethylene glycol at moderate temperature. Zinc forms stable chelate complex with citric acid and is known to be soluble in ethylene glycol. Extended heating of the reaction mixture with simultaneous evaporation of the solvent results in randomly branched polymeric ester chain with Zn^{2+} ions uniformly distributed throughout the binding sites. This polymeric structure breaks down when calcined forming ZnO nanoparticles [5].

The FTIR spectra obtained for the ZM samples are shown in Fig. 8. There are -OH stretching and bending vibrations located at ∼3500 cm^{-1} and 1500 cm^{-1} in the spectra of ZM3 and ZM5 samples associated with the water molecules adsorbed on the surfaces of the nanoparticles. The spectra of ZM7 have weak peaks related to -OH stretching and bending vibrations located at ∼3500 cm^{-1} and 1529 cm^{-1} respectively. The stretching vibration due to carboxylic acid -OH stretching was indicated by an IR peak near 2350 cm^{-1} and corresponding bending vibrations were appeared at 900-1040cm^{-1}. In addition, peak appeared at ∼1388cm^{-1} in the FTIR spectra of ZM3, and ZM5 is associated with the carbonyl stretching vibrations indicating the persistence of organic residues from the reaction medium. These peaks were comparatively pronounced in ZM3 and the intensity was reduced for ZM5. The residual peaks are minimally appeared or absent in ZM7 sample. A sharp and intense spectroscopic band located around 470 cm^{-1} was attributed to the characteristic Zn-O vibrational mode, which confirms the formation of ZnO [6].

According to the tentative mechanisms suggested for the formation of ZnO nanoparticles via plant extracts, initially the phytochemicals coordinate (through donor atoms) with the Zn^{2+} leading to the formation of some Zn-phyto complex. The complex gets decomposed on calcination resulting ZnO nanoparticles [7]. Mucilage is a thick and slimy hydrocolloid, which is a common constituent present in plants, where it is highly soluble in water with inherent viscosity, plasticity, and elasticity [8-11].Carbohydrates, proteins, some neutral sugars, amino acids, and other secondary metabolites are mainly present in the mucilage of *Abelmoschus esculents* [12, 13]. The studies on chemical composition of okra mucilage estimates the mean total phenolic content as 37.42% and flavonoid content about 13.67%. Moreover, remarkable metal-chelating property of this mucilage was reported by

Gemede et al., which can be attributed to the polyphenolic and flavonoid contents [11]. These compounds can effectively bind zinc ions from an aqueous medium and they function as natural reducing and stabilizing agents during the synthesis of nanoparticles [14, 15].
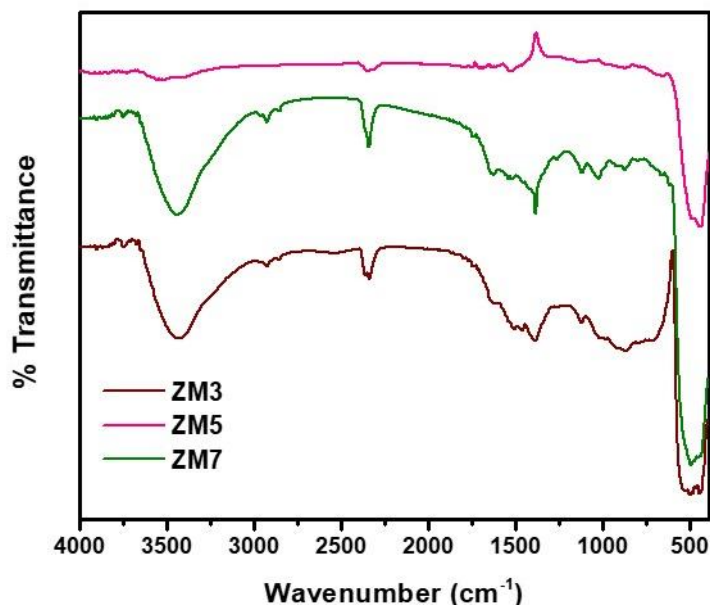

Fig.8. FTIR spectra of ZM3, ZM5, and ZM7 ZnO nanoparticles.

The FTIR spectra of the ZG nanoparticles exhibited a sharp characteristic peak of the Zn–O stretching vibration at 470 cm-^{1}. The –OH stretching and bending vibrations were present at 3451 cm^{-1} and 1620 cm^{-1}, respectively. The stretching and bending vibrational modes of C–H groups from the organic residues were observed at 2837–2918 cm^{-1} and 1374 cm^{-1}. The residual peaks were prominent for ZG3 owing to the low calcination temperature of the sample. The peaks were reduced for ZM5, and ZM7 as prepared at higher calcination temperatures. Fig. 9 represents the FITR spectra of ZG samples.
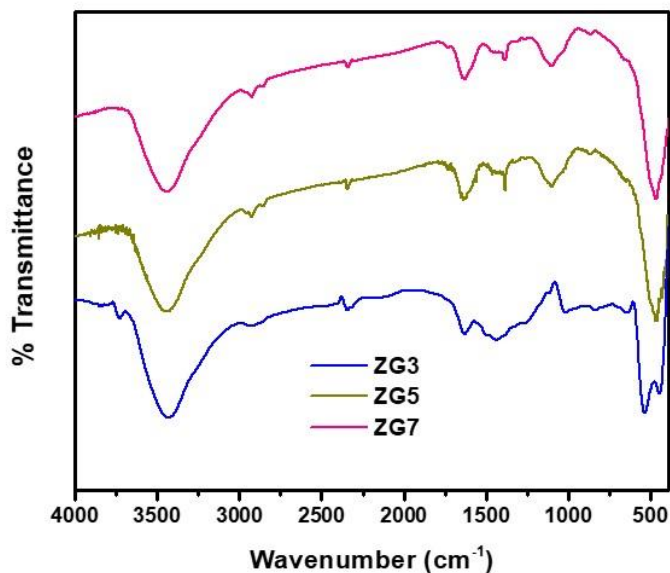
Fig.9. FTIR spectra of ZG3, ZG5, and ZG7ZnO nanoparticles.

Gliricidia sepium is readily available in many parts of India, does not require special effort to cultivate, and carries leaves even in the dry season. The leaves are known for nitrogen fixation and mosquito-repellent (larvicidal) properties [16]. Reports on the phytochemical profile of *G. sepium* leaf extracts in different media are available in literatures. Quantitative and qualitative phytochemical studies of the watery leaf extracts have revealed substantial amounts of phytochemicals: alkaloids, flavonoids, and polyphenols [17, 18]. During synthesis, such phytochemicals act as natural reducing agents and stabilizers for formation of ZnO nanoparticles. Table 2 summarizes the qualitative and quantitative phytochemical profile of aqueous leaf extract of *G. sepium* as available in the literatures.

Table 2. Qualitative and quantitative phytochemical profile of aqueous leaf extract of *G. sepium* [18, 17].

Phytochemicals	Occurrence	Amount
Alkaloids	+	6.80 (%)
Flavonoids	+	0.45 mg/mL
Saponins	+	5.85 mg/mL
Phenols	+	0.12 mg/mL
Tannins	+	1.56 mg/mL
Glycosides	-	-
Terpenoids	+	-

3.3. FESEM and HRTEM analysis

The surface morphology and size of the nanoparticles were monitored via FESEM and HRTEM micrographs. Fig. 10.A-C represents the FESEM micrographs and Fig. 10.D–F depicts the HRTEM images of the ZL nanoparticles obtained. A spherical and near- spherical morphology was observed for the three samples and the average particles size of 11.31 nm, 32.61 nm and 49.42 nm was obtained for Z3, Z5 and Z7 respectively. This indicates agglomeration tendency at higher temperatures due to the successive losing of binders and high surface energy of the particles.

The FESEM morphology of ZM3 exhibited a spherical and elongated shapes with average particles size of 42.66 nm. ZM5 and ZM7 is comprised of spherical and rod-like particles of average dimension 20-70 nm. Fig. 11.A-C represents the FESEM micrographs and Fig. 11.D–F depicts the HRTEM images of the ZM nanoparticles. The ZG samples have shown near-spherical and elongated particles in the FESEM morphology. The average particles size of ZG3, ZG5, and ZG7 samples obtained are 45.63 nm, 62.91 nm, and 55.70 nm respectively. The FESEM and HRTEM micrographs of ZG samples are depicted in Fig. 12.A-C and Fig. 12.D-F respectively. The particle size and shape of ZnO nanoparticles has been summarized in Table 3.
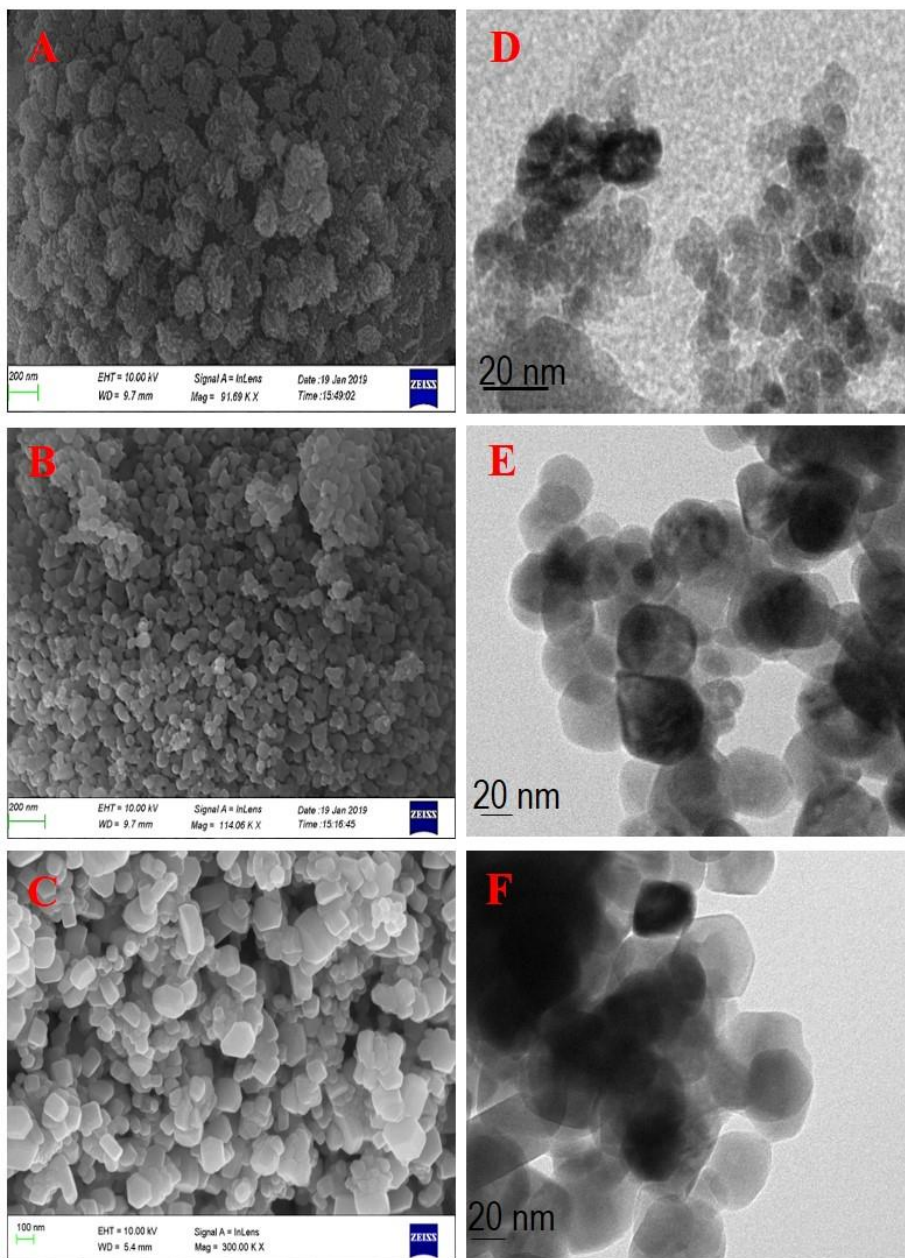
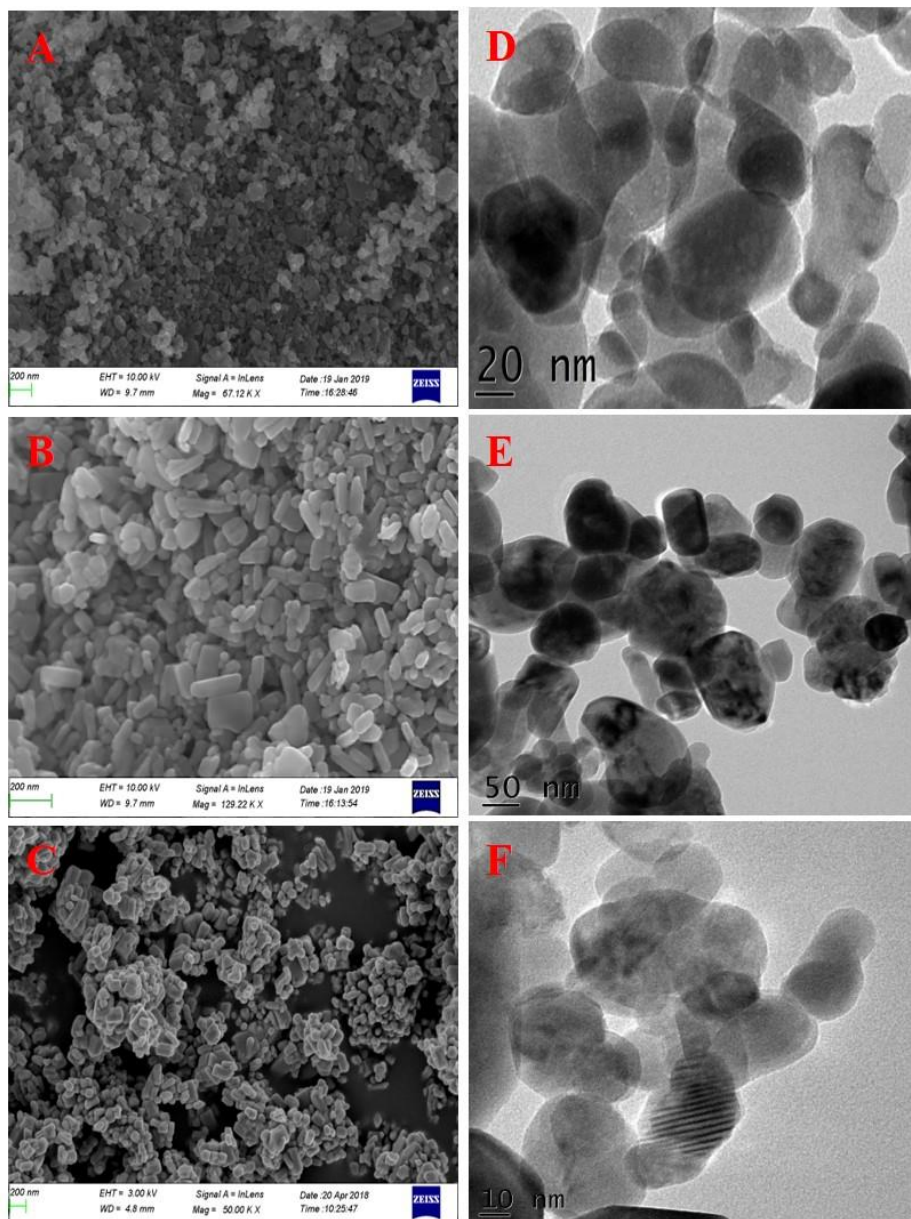**Fig.10.** A–C) FESEM micrographs and D–F) HRTEM images of ZL3, ZL5 and ZL7 nanoparticles.

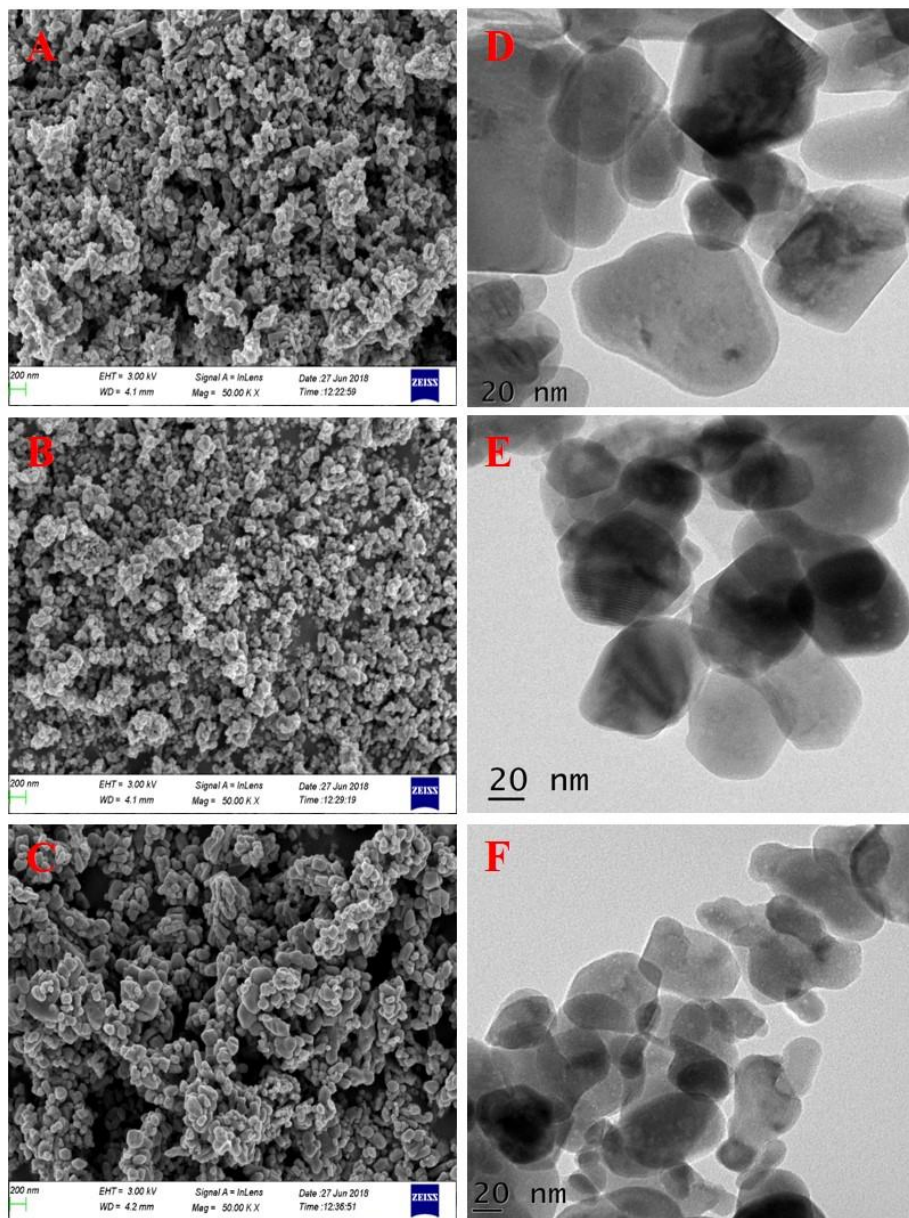**Fig. 11.** A–C) FESEM micrographs and D–F) HRTEM images of ZM3, ZM5 and ZM7 nanoparticles.

Fig. 12. A–C) FESEM micrographs and D–F) HRTEM images of ZG3, ZG5 and ZG7 nanoparticles.

Table 3. The morphology and size of ZL, ZM, and ZG ZnO nanoparticles determined from FESEM and HRTEM analysis.

No.	Sample	Size (nm)	Shape
1	ZL3	11.31	Spherical
2	ZL5	32.61	Spherical
3	ZL7	49.42	Spherical and near-spherical
4	ZM3	42.66	Spherical and elongated
5	ZM5	20-70	Spherical and rod-like
6	ZM7	20-70	Spherical and rod-like
7	ZG3	45.63	Near-spherical and elongated
8	ZG5	62.91	Near-spherical and elongated
9	ZG7	55.70	Near-spherical and elongated

3.4. EDX and XPS profiles of ZnO nanoparticles

The composition of the material was studied further by conducting EDX analysis. Fig. 13-15 shows the typical EDX profile of ZL, ZM, and ZG samples respectively. ZnO nanoparticles exhibits characteristic peak lines located around 1.0 and 8.6 KeV corresponds to Lα and Kα elemental spot for Zn. Characteristic oxygen (Kα) peaks can be seen in the profile around 0.55 KeV. The traces of some organic residues remained in the sample placed a weak peak line about 0.28 KeV attributed to Kα of carbon.
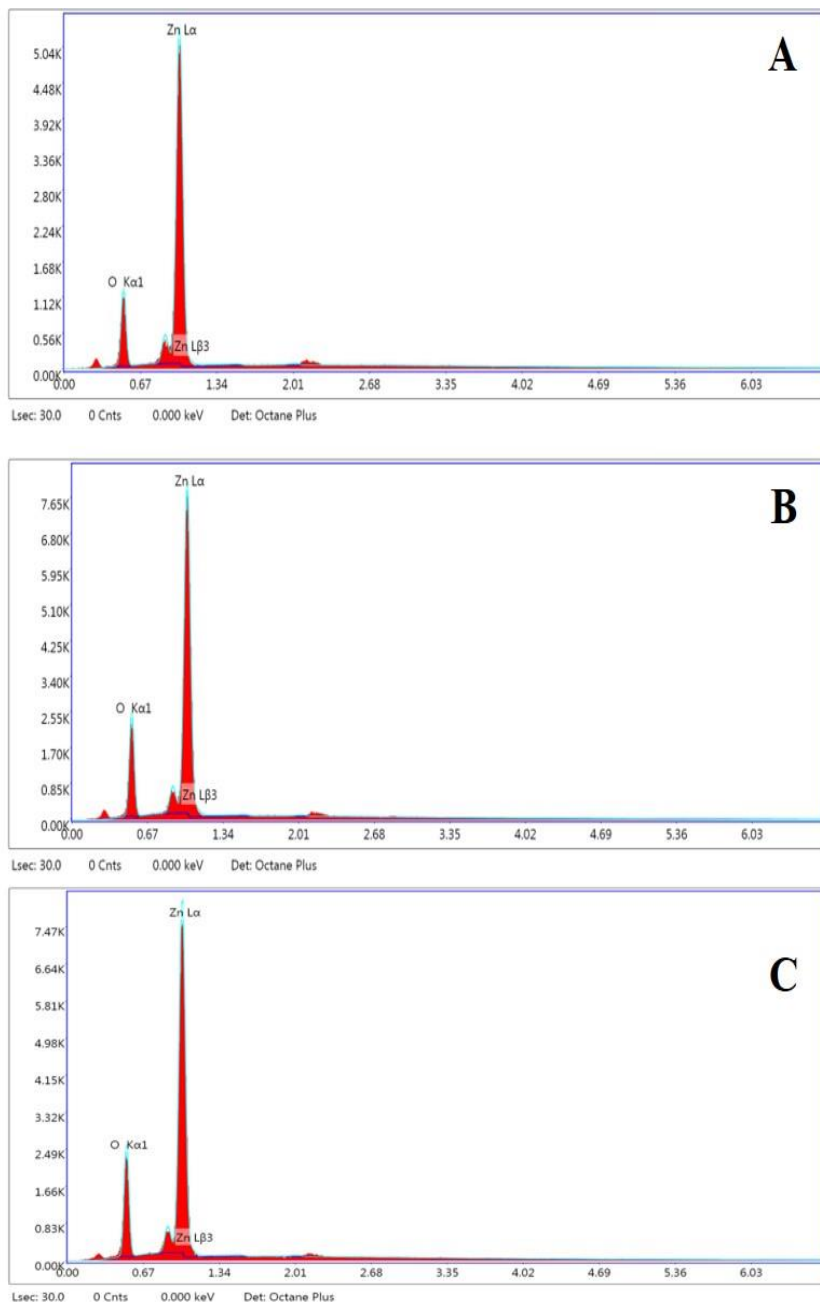
Fig. 13. EDX profile of ZnO nanoparticles A) ZL3, B) ZL5, and C) ZL7
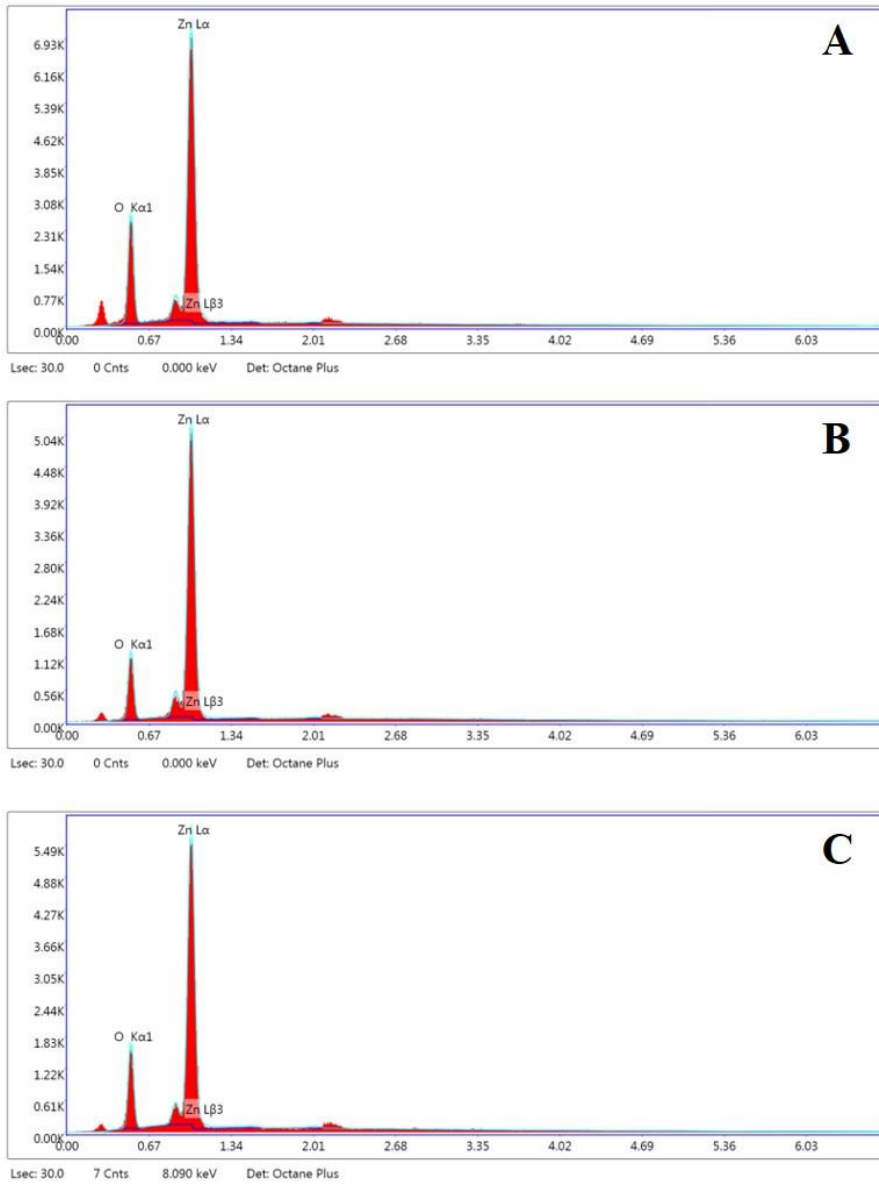
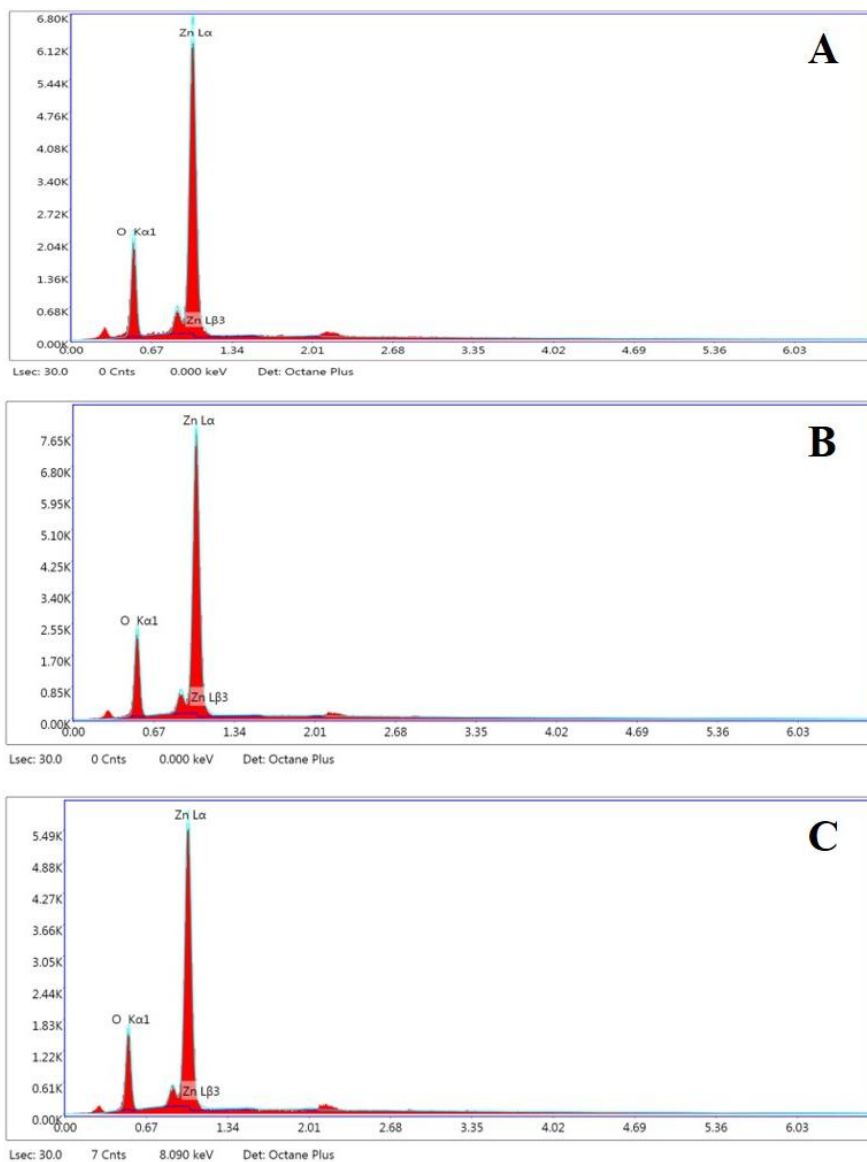**Fig. 14.** EDX profile of ZnO nanoparticles A) ZM3, B) ZM5, and C) ZM7

Fig. 15. EDX profile of ZnO nanoparticles A) ZG3, B) ZG5, and C) ZG7

The composition and chemical state of elements in the sample were obtained via XPS. Fig. 16-21 represents the XPS profile of ZL, ZM, and ZG samples. The full-scan survey XPS of the samples shows the presence of zinc, oxygen,

and carbon. Zn ($2p_{3/2}$) and Zn ($2p_{1/2}$) peaks were encountered at 1020.81 eV and 1042.67 eV, in the elemental XPS scan corresponding to Zn^{2+} ($2p_{3/2}$) and Zn^{2+} ($2p_{1/2}$). The XPS peak for O (1s) was located at 529.28 eV, and indicated O^{2-} [1]. The peak for C (1s) at 285.8 eV could have been due to trace levels of phytochemical residues which acted as reducing and stabilizing agents.
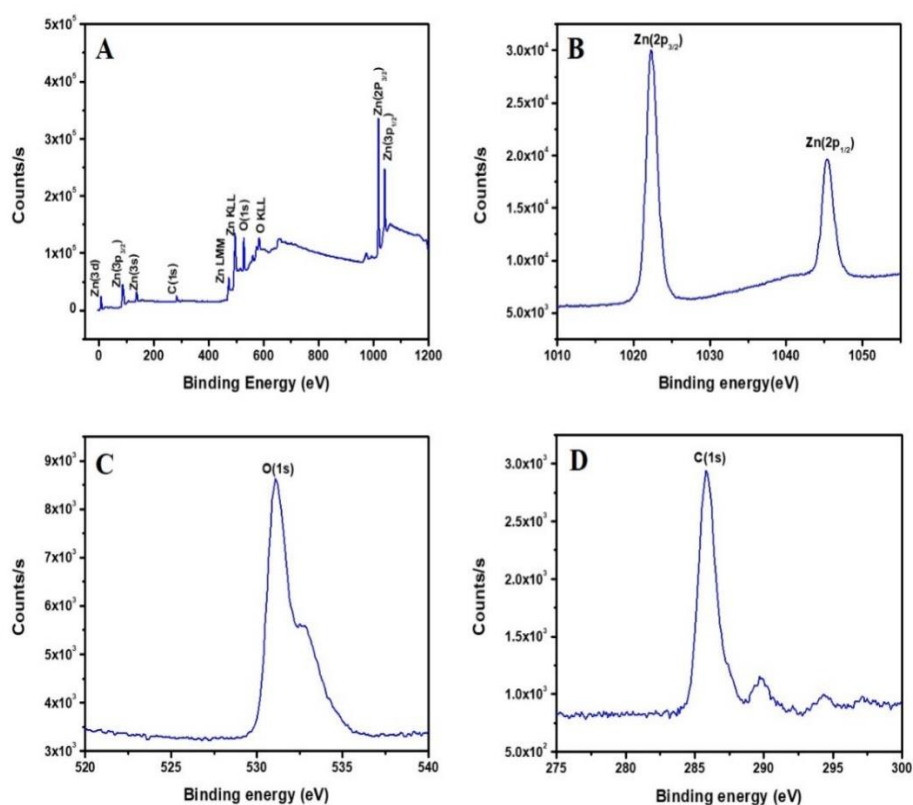
Fig. 16.A) Full-scan survey XPS and elemental-scan XPS for B) Zn 2p, C) O 1s and D) C 1s of ZL5 nanoparticles.
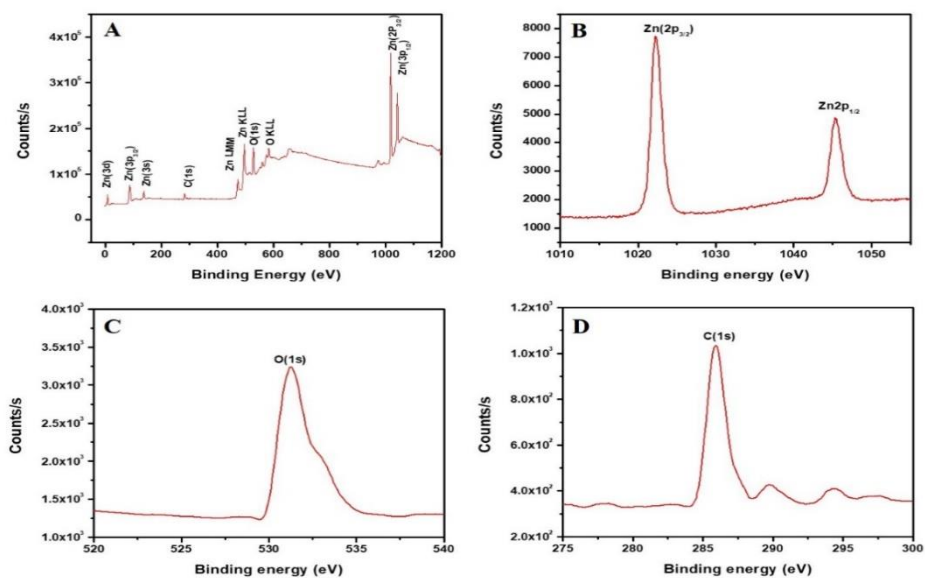
Fig. 17.A) Full-scan survey XPS and elemental-scan XPS for B) Zn 2p, C) O 1s and D) C 1s of ZL7 nanoparticles.
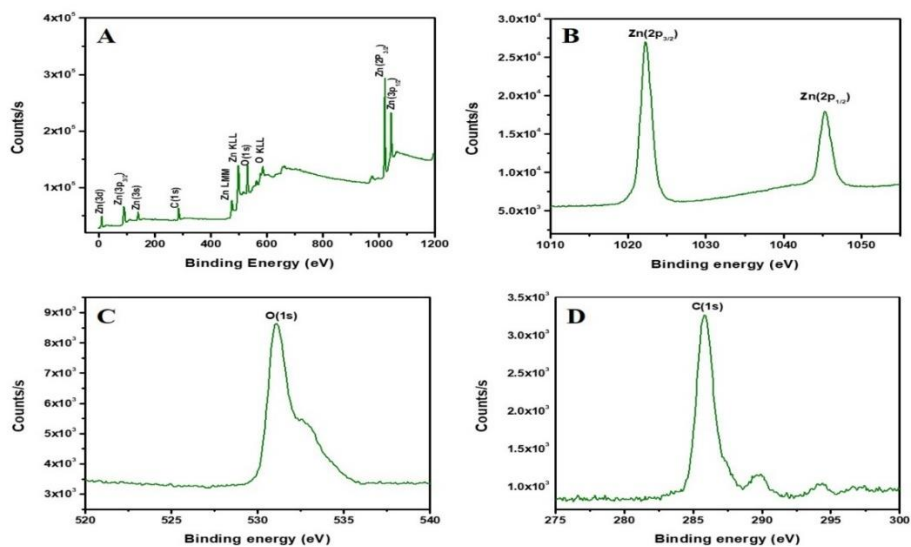
Fig. 18.A) Full-scan survey XPS and elemental-scan XPS for B) Zn 2p, C) O 1s and D) C 1s of ZM5 nanoparticles.
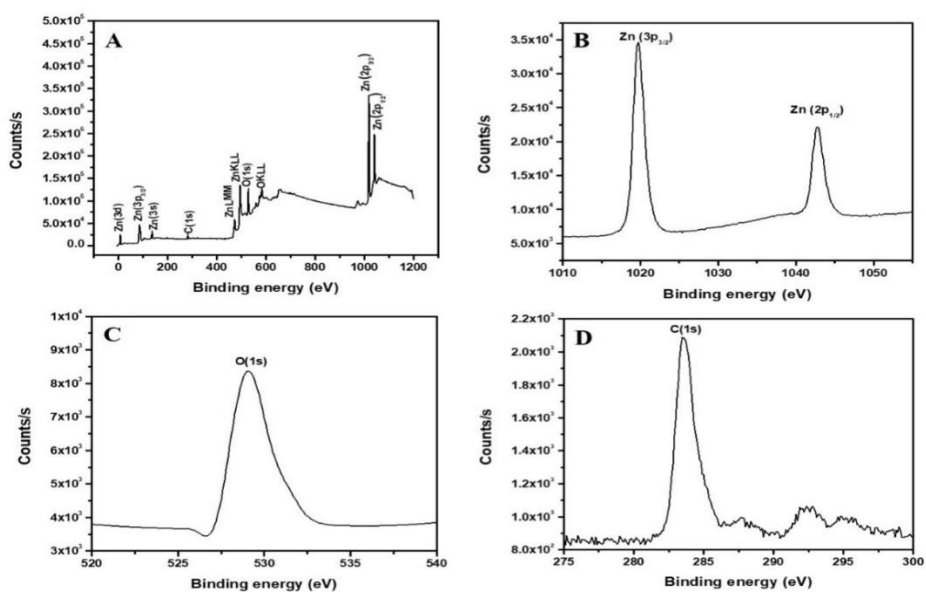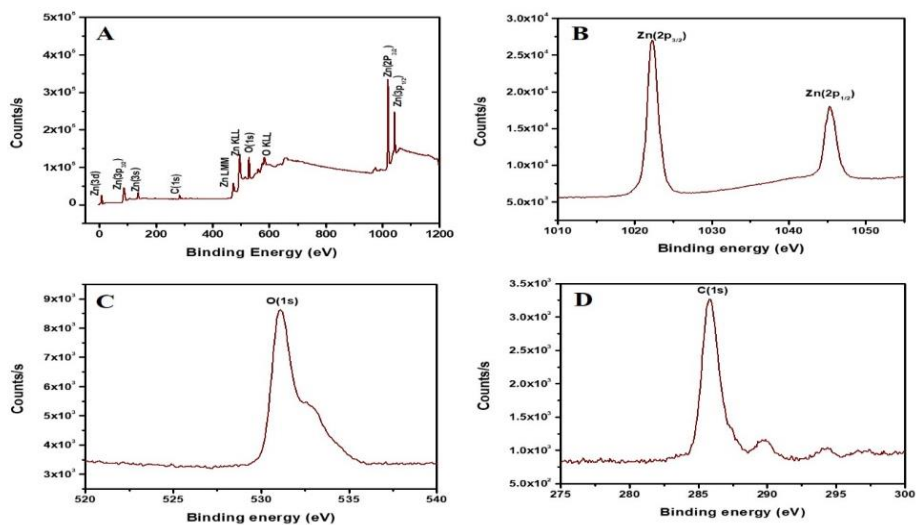
Fig. 19.A) Full-scan survey XPS and elemental-scan XPS for B) Zn 2p, C) O 1s and D) C 1s of ZM7 nanoparticles.

Fig. 20.A) Full-scan survey XPS and elemental-scan XPS for B) Zn 2p, C) O 1s and D) C 1s of ZG5 nanoparticles.

Fig. 21.A) Full-scan survey XPS and elemental-scan XPS for B) Zn 2p, C) O 1s and D) C 1s of ZG7 nanoparticles.

3.5. UV-Vis DRS-Optical band gap of ZnO nanoparticles

The optical band gap is a crucial constraint for the photocatalytic materials since the electronic excitation between the valance and conduction band occurs with the incident photon having energy equal or greater than the band gap energy. Tauc proposed the following expression for obtaining the optical band gap

$$(hv\alpha) = A\big(hv - E_g\big)^n \qquad (2)$$

where A is the absorption constant and α is the absorption coefficient and n is a constant depends on the material (here n=0.5). Fig. 22-24 represents the Tauc plots obtained for ZL, ZM, and ZG samples respectively. The optical band gap of the samples is listed in Table 4.

Table 4. Optical band gap energy of ZL, ZM, and ZG ZnO nanoparticles derived from Tauc Plot.

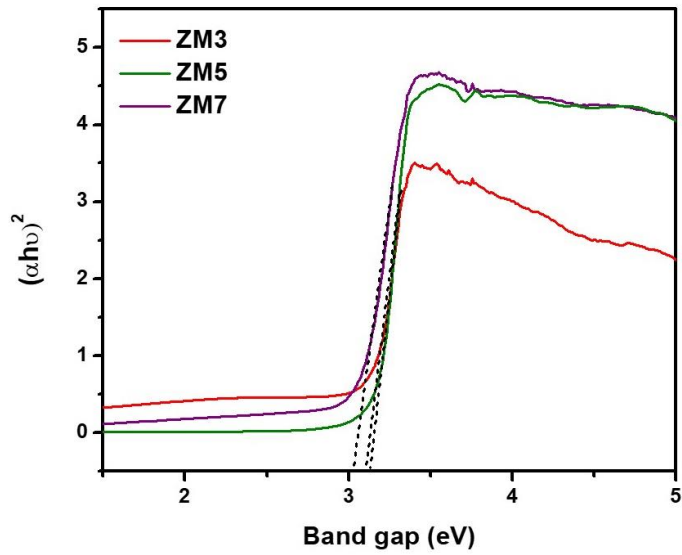| No.	sample	Optical band gap (eV)
1	ZL3	3.25
2	ZL5	3.12
3	ZL7	3.12
4	ZM3	3.12
5	ZM5	3.10
6	ZM7	3.04
7	ZG3	3.13
8	ZG5	3.08
9	ZG7	3.08
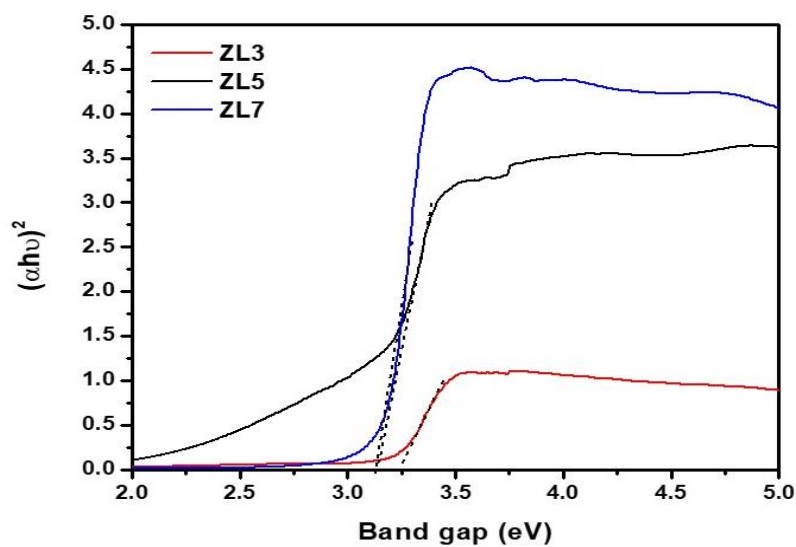
Fig. 22. Tauc plot showing the optical band gap obtained for ZL3, ZL5, ZL7 nanoparticles.
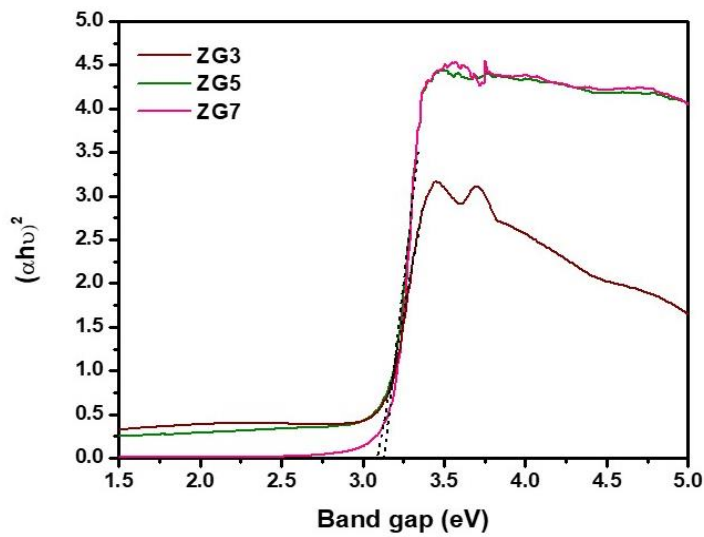
Fig.23. Tauc plot showing the optical band gap obtained for ZM3, ZM5, ZM7 nanoparticles.

Fig.24. Tauc plot showing the optical band gap obtained for ZG3, ZG5, ZG7 nanoparticles.

3.6. Surface charge of ZnO nanoparticles: Zeta potential

The surface charge of nanoparticles affects their physical state in solution. Zeta potential is a method for the direct measurement of surface charge and used to study the peripheral characteristics of nanoparticles in solution. Nanoparticles in their dispersed state attract the oppositely charged ions towards the surface. The resulting thin layer moves along with the nanoparticle (electric double layer) under the influence of electric filed, gravity or kinetic energy and a boundary is formed between ions in the diffusive layer and the ions remain in the bulk. The electrostatic potential at this boundary is measured as zeta potential and the values typically in rage of +100 to -100 mV [19].

Table 5. Zeta potential of ZL, ZM, and ZG ZnO nanoparticles.

No.	Sample code	Zeta potential (mV)
1	ZL3	-13.67
2	ZL5	-19.0
3	ZL7	-31.52
4	ZM3	2.55
5	ZM5	8.33
6	ZM7	-38.37
7	ZG3	7.32
8	ZG5	-17.2
9	ZG7	-36.74

Generally, nanoparticles having high zeta potential values (negative or positive) own high degree of colloidal stability. The values that are less negative than -15 mV indicate the tendency to agglomerate and zero values

represents the propensity to precipitate as solid particles [20]. The zeta potential was measured for the synthesized ZnO nanoparticles and the values are presented in Table 5. According to the zeta potential values obtained the stability of nanoparticles in solution follows the order ZM7>ZG7>ZL7>ZL5>ZG5>ZL3>ZG3>ZM5>ZM3.

3.7. Summary

➢ Present chapter covers the characterization ZnO nanoparticles prepared using *Citrus lemon* extract (ZL), *Abelmoschus esculents* mucilage (ZM), and *Gliricidiasepium* leaf extract (ZG).

➢ The XRD and SAED pattern reveals the hexagonal wurtzite structure of ZnO nanoparticles formed with substantial crystallinity. Higher the calcination temperature, more crystalline the samples become. The average crystallite size of the samples was determined from the XRD patterns.

➢ The morphology of the nanoparticles was monitored with FESEM micrographs and average particle size was determined from the HRTEM analysis. The morphology and size of the samples varies with the synthesis method and calcination temperatures.

➢ FTIR spectra contains the characteristic vibrational peaks of ZnO samples. Some residual peaks were also present.

➢ XPS, and EDX profiles reveals the presence of elemental composition and chemical state. The samples contain zinc and oxygen along with trace amount of carbon residues remained from the reaction medium.

> Optical band gap of the samples was determined using Tauc plot derived from the UV-Vis- DRS spectra. The values ranges from 3.08 to 3.25 eV.

> The surface charge of the samples was determined via zeta potential analysis. According to the zeta potential values obtained the stability of nanoparticles in solution follows the order ZM7>ZG7>ZL7>ZL5> ZG5>ZL3>ZG3>ZM5>ZM3.

Reference

1. A. R. Prasad, J. Garvasis, S. K. Oruvil and A. Joseph, J. Phys. Chem. Solids, 2019, 127, 265.

2. T. Zhai, S. Xie, Y. Zhao, X. Sun, X. Lu, M. Yu, M. Xu, F. Xiaoc and Y. Tong, Cryst. Eng. Comm, 2012, 14, 1850.

3. G. Zhang, X. Shen, Y. Yang, J. Phys. Chem. C, 2011, 115, 7145.

4. A. Rauf, G. Uddin, J. Ali, Org Med Chem Lett., 2014, 4, 5.

5. F. Davar, A. Majedi, A. Mirzaei, J. Am. Ceram. Soc., 2015, 98, 173.

6. C. Anupama, A. Kaphle, Udayabhanu, G. Nagaraju, J. Mater. Sci. Mater. Electron., 2018, 29, 4238.

7. R.Chokkareddy, G.G. Redhi, SuvardhanKanchi and Shakeel Ahmed (eds.) Green Metal Nanoparticles, 2018 Scrivener Publishing LLC, 2018.

8. H.F. Gemede, N. Ratta, G.D. Haki, A.Z. Woldegiorgis, FB. Gemede, J. Food Process. Technol., 2015, 6, 6.

9. J.N. BeMiller, R.L. Whistler, D.G. Barkalow, C.C. Chen, Aloe, Chia, Flax Seed, Okra, Psyllium Seed, Quince Seed, and Tamarin Gums, Academic Press, New York, 1993.

10. J.K. Ahiakpa, H.M. Amoatey, G. Amenorpe, J. Apatey, E.A. Ayeh, W.S.K. Agbemavor, Scientia Agriculturae, 2014, 2, 96.

11. H.F. Gemede, G.D. Haki, F. Beyene, S.K. Rakshit, A.Z. Food Sci. Nutr., 2018, 6, 563.

12. I.M. Liu, S.S. Liou, T.W. Lan, F.L. Hsu, J.T. Cheng, Med., 2005, 71, 617.

13. R. Kumar, M.B. Patil, S.R. Patil, M.S. Paschapur, Intl. J Pharm. Tech. Res., 2009, 1, 658.

14. J. Suresh, G. Pradheesh, V. Alexramani, M. Sundrarajan, S.I. Hong, Adv. Nat. Sci. Nanosci. Nanotechnol., 2018, 9, 015008.

15. A. Pavan Kumar, H. Nagabhushana, S.C. Sharma, spectrochim. Acta A Mol. Biomol. Spectrosc., 2015, 141, 128.

16. K.V. Krishnaveni, R. ThaiyalNayaki, M. Balasubramanian, J. Phytol., 2015, 7, 26.

17. N.S. Kumar, N. Simon, J. Pharmacogn. Phytochem., 2016, 5, 131.

18. S. N. Sinha, Int. J. Biomed. Sci., 2013, 3, 87.

19. E. Joseph, G.Singhvi, Nanomed. Drug Delivery Ther., 2019, 1, 91.

20. G.W. Lu, P. Gao, Handbook of Non-Invasive Drug Delivery Systems, 2010, Pages 59-94.

Diabetes mellitus has been recognized as one of the major deaths causing diseases in the world. Globally a large patient population around 200 million are currently seeking treatments while the heterogeneous nature of the disease demands cost effective and multifunctional therapies. Diabetic control through the inhibition of carbohydrate hydrolysing enzymes is established as an effective strategy. Many of the inorganic materials have already been investigated as enzyme inhibitors. ZnO nanoparticles have received wide attention for the biomedical applications. Even though many of the inorganic materials especially those derived from green strategies have been investigated for the α-glucosidase and α-amylase inhibition, zinc-based inhibitors are being preferentially investigated.

Chapter 4

In-vitro alpha-amylase and alpha-glucosidase inhibition: antidiabetic activity of ZnO nanoparticles
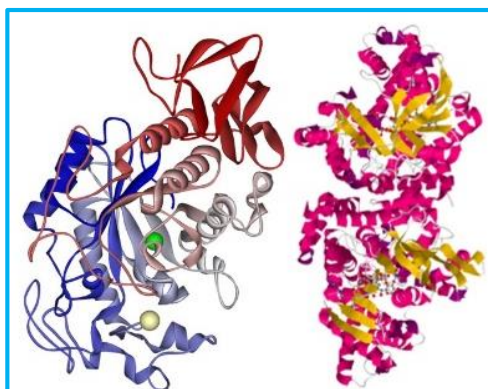
"Nanotechnology in medicine is going to have a major impact on the survival of human race."

Bernard Marcus

Diabetes mellitus is a multifunctional disease identified as one among the major death causing diseases world-wide and would be the prime cause of illness and decease in coming decades [1]. Currently more than 200 million people are under treatment in global profile while the international Diabetes Federation (IDF) predicts a huge increase in patient population beyond 592 million in coming 25 years [2, 3]. The diabetic disease makes chronic and sever endocrine disorders and diabetes can be categorized as Type 1 (hyperglycemia) arises due to insulin deficiency and Type 2 due to the inefficient response of the cells to the insulin produced [4-6]. Both types are accompanied with consequent rise in blood glucose level while most of the people are being suffered from Type 2 diabetes [7]. Thus, the strategies of stimulation of insulin production and inhibition of carbohydrate hydrolysing enzymes like α-amylase, α-glucosidase etc are proven to be effective for controlling the blood glucose levels in the body [8]. For Type 2 diabetic treatment, the inhibitors having mild amylase and strong glucosidase inhibition are preferred [9], consequently majority of the researches are focused on enzyme inhibitors. Since the existing therapeutic medicines like miglitol, acarbose, voglibose etc induce side effects in gastro-intestinal tracks and abdominal bloating the development and practice of new enzyme inhibitors are of great interest [5, 9]. The application of natural compounds like polyphenolic compounds having notable inhibition towards α-amylase are limited due to their bio-instability in intestinal tract [10].

The *in-vitro* studies on the carbohydrate hydrolysing enzymes are beneficial to sort and exclude inactive candidates when a number of compounds are to be examined, thereby saving substantial time and money [10]. Herein, *in-vitro* α -amylase activity was carried out by DNSA method.The effect of nanoparticles on α-glucosidase activity was determined according to the method described by Kim et al., using pNPG.

4.1. *In-vitro* α-amylase Inhibition

The *in-vitro* inhibition of α-amylase and α-glucosidase was studied by loading 25- 100 μg/mL of ZnO nanoparticles. Fig. 1 shows the percentage inhibition profile of the ZL3, ZL5, and ZL7 samples towards α-amylase activity. It can be noticed that all samples are very mild inhibitors for α-amylase and the maximum inhibition efficiency at the studied dosage of the nanoparticles was offered by ZL5 (22%).
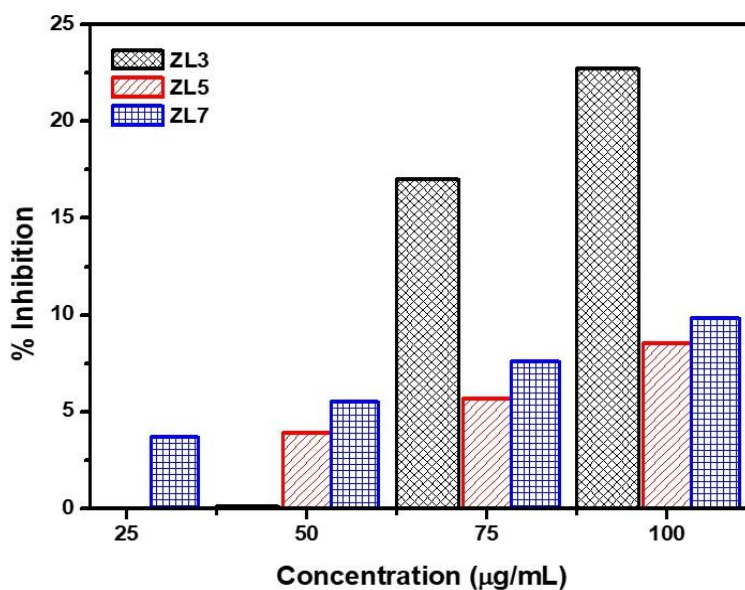

Fig. 1. α-amylase inhibition activity of ZnO nanoparticles synthesised using *citrus lemon* extract.

The α-amylase inhibition activity of ZM3, ZM5 and ZM7 samples has been presented in Fig. 2. The samples are mild amylase inhibitors except ZM5 having maximum inhibition efficiency up to 85.37%. The samples ZM3 and ZM7 exhibited 13.71 and 23.4 percent inhibition efficiency respectively. Also, the efficiency was proportional to the ZnO dose. The IC_{50} value of the ZM5 sample was determined to be 3.58 μg/mL.
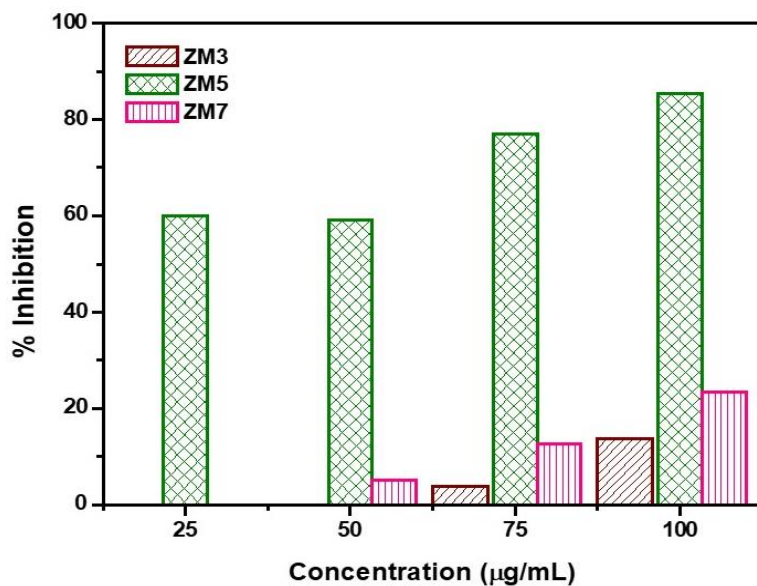
Fig. 2. α-amylase inhibition activity of ZnO nanoparticles synthesised using *Abelmoschus esculents* mucilage.
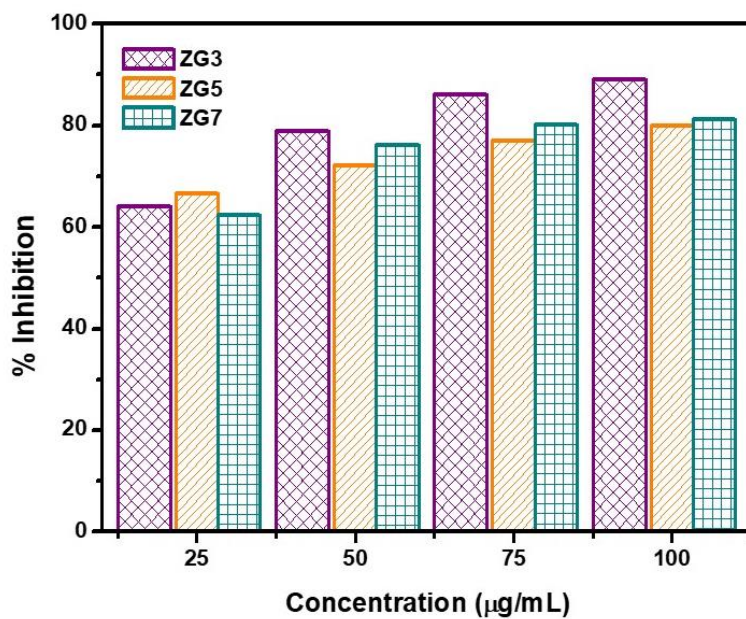

Fig. 3. α-amylase inhibition activity of ZnO nanoparticles synthesised using *Gliricidia sepium* leaf extract.

87

ZnO nanoparticles obtained by using *Gliricidiasepium* leaf *extract* exhibit prominent activity towards α-amylase enzyme. ZG3 sample hold the highest inhibition efficiency 88.99%. All samples inhibit the amylase activity above ~60% on their initial dosage itself and the efficiencies increase with successive nanoparticle dosage. The inhibition efficiency of the samples ZG5 and ZG7 are 79.9% and 81.23% respectively. IC_{50} value of the sample ZG3 having maximum efficiency was measured to be 2.71 µg/mL.Fig. 3 shows the α-amylase inhibition activity of ZG3, ZG5 and ZG7 samples.

4.2. *In-vitro* α-glucosidase Inhibition

Fig. 4 displays the percentage inhibition of α-glucosidase by ZL3, ZL5 and ZL7 samples. The nanoparticles exhibit remarkable activity among which ZL5 (97.87%) have the maximum performance. The inhibition efficiency was increased with concentration of nanoparticles. ZL3 has the least performance with maximum inhibition efficiency of 46.3%. The sample ZL7 could inhibit the enzymatic action up to 76.5% within the studied dosage. ZnO nanoparticles obtained by using the *citrus lemon* extract are thus selective inhibitors for the action of α-glucosidase enzyme. IC_{50} value of the sample ZL5 was obtained 1.24 µg/mL.

The ZnO nanoparticles ZM3, ZM5 and ZM7 exhibit comparable inhibition efficiencies 72.91, 74.4 and 72.19% respectively towards α-glucosidase. ZM5 is a strong inhibitor for both the diabetic enzymes whereas, the samples ZM3 and ZM7 are selective inhibitors for α-glucosidase action. Fig. 5 depicts the α-glucosidase inhibition by ZnO nanoparticles prepared using *Abelmoschus esculents* mucilage. The IC_{50} value of ZM5 was found to be 53.8 µg/mL.
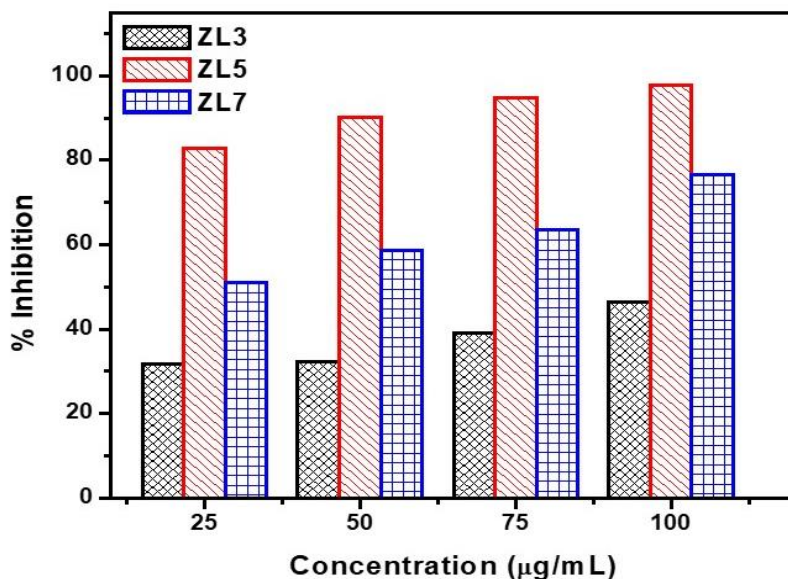
Fig. 4. α-glucosidase inhibition activity of ZnO nanoparticles synthesised using *citrus lemon* extract.
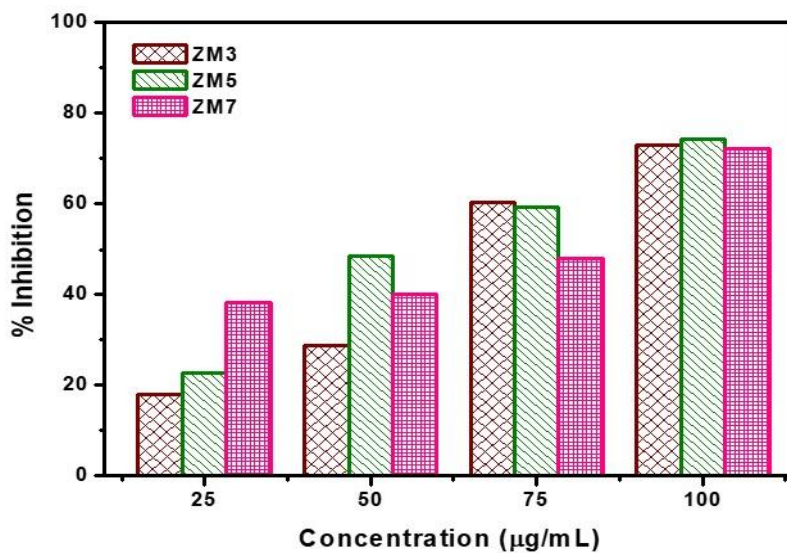

Fig. 5. α-glucosidase inhibition activity of ZnO nanoparticles synthesised using *Abelmoschus esculents* mucilage.
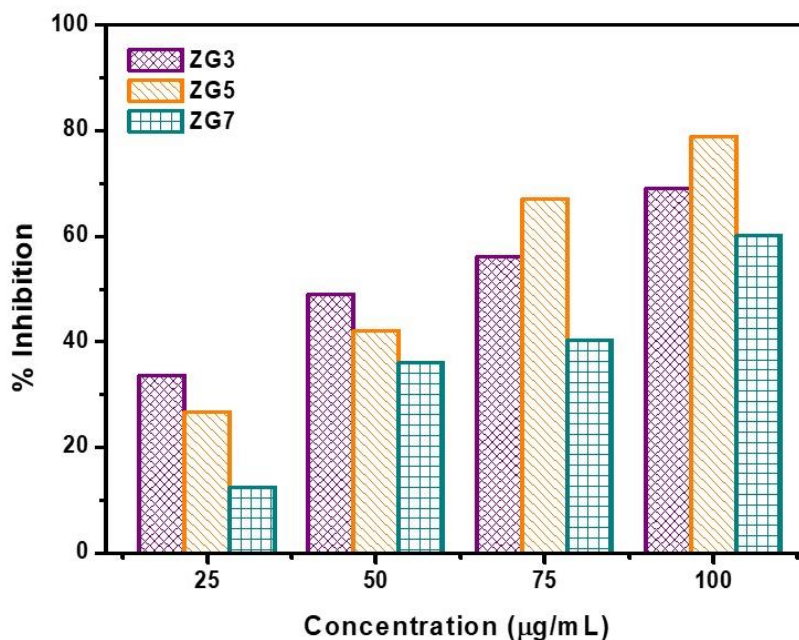
Fig. 6. α-glucosidase inhibition activity of ZnO nanoparticles synthesised using *Gliricidiasepium* leaf extract.

The ZnO nanoparticles ZG3, ZG5 and ZG7 are active towards α-glucosidase enzyme. The percentage inhibition was concentration dependent, there observed an increase with successive dosage of nanoparticles. Fig. 6 shows the α-glucosidase inhibition of ZnO nanoparticles obtained using *Gliricidiasepium* leaf extract. ZG5 sample holds the maximum inhibition efficiency of 78.9% with IC_{50} value 57.6 μg/mL. Being a strong inhibitor for α-amylase the nanoparticle lacks selectivity for the diabetic enzymes.

4.3. Cytotoxicity of ZnO

The cytotoxic effect of the ZnO nanoparticles holding highest inhibition efficiencies was evaluated towards Chang liver cell lines. Loading of ZL5 sample (having selective inhibition of α-glucosidase) at the initial

concentration (6.25µg), 88% of the cells were survived. A gradual reduction in cell viability was observed with the double increment in concentration of the nanoparticles. The CC50 value of the sample was determined to be 88.89µg/mL. The cell viability was shortened to 30% at 100µg/ml concentration of ZnO. Hence, we should concern about cytotoxic nature of the sample above 88.89µg/mL. The selectivity index (SI) of the sample was determined by the ratio of CC50/IC50. To be a new potential drug the contender should possess a SI value equal or greater than 10 [11,12]. Here in the SI value is 71.68 indicates the safety to normal cell lines and selectivity towards the α-glucosidase inhibition [13,14]. Table 1 summarizes the IC50, CC50 and selectivity index calculated for the ZnO nanoparticles.

The CC50 value of the sample ZM5 was calculated to be 94.7 µg/mL. The cell viability was reduced from 91% to 42% with the successive concentrations of ZnO (6.25-100 µg/mL). Thus, in context of α-amylase and α-glucosidase inhibition, since the ZM5 exhibit strong activity towards both, the concentrations above 94.7 µg/mL would be harmful for the normal cell lines. The SI value 26.45 for α-amylase inhibition ensures the safe and selective execution below its cytotoxic concentration. However, the SI value lower than 10 was obtained for α-glucosidase inhibition.

Table 1. CC50, IC50 and selectivity index of ZnO samples

Sample	CC50 (µg/mL)	SD	IC50 (α-amylase) (µg/mL)	SD	IC50 (α-glucosidase) (µg/mL)	SD	SI value (α-amylase)	SI value (α-glucosidase)
ZL5	88.89	3.26×10^{-3}			1.24	5.26×10^{-2}		71.68
ZM5	94.7	2.69×10^{-3}	3.58	2.46×10^{-2}	53.8	4.33×10^{-2}	26.45	1.76
ZG3	87.23	6.41×10^{-3}	2.71	2.98×10^{-2}			32.188	
ZG5	83.51	4.12×10^{-3}			57.6	3.62×10^{-2}		1.44

The CC50 values of ZG3 and ZG5 are 87.23 µg/mL and 85.23 µg/mL exhibiting the highest inhibition efficiency for α-amylase and α-glucosidase respectively. Hence the cytotoxic effect should be considered above these concentrations of the samples. The selectivity index indicates that the ZG3 sample is biologically safe and selective towards the target cites than the normal cells. However, ZG5 sample lacks selectivity over the target enzymes since the SI value is below 10.

4.4. Summary

➢ In-vitro α-amylase and α-glucosidase inhibition of ZnO nanoparticles were studied.

➢ ZnO nanoparticles synthesized using *citrus lemon* extract shows selective inhibition towards α-glucosidase. The maximum inhibition efficiency was obtained with ZL5 while the cytotoxicity has to be considered above 88.89µg/mL. Higher selectivity index ensures the benign and selective nature.

➢ Among the ZnO nanoparticles synthesised using *Abelmoschus esculents* mucilage, ZM5 holds strong α-amylase inhibition while others display very mild activity. The cytotoxicity of ZM5 should be considered when the concentration is above 94.7 µg/mL. SI value was obtained in favourable limit.

➢ Interestingly, ZM5, ZM3, and ZM7 samples shows substantial and comparable activity towards α-glucosidase enzyme. However, the SI value below 10 indicates the sample in addition would act on normal cell lines rather than discerning target enzyme.
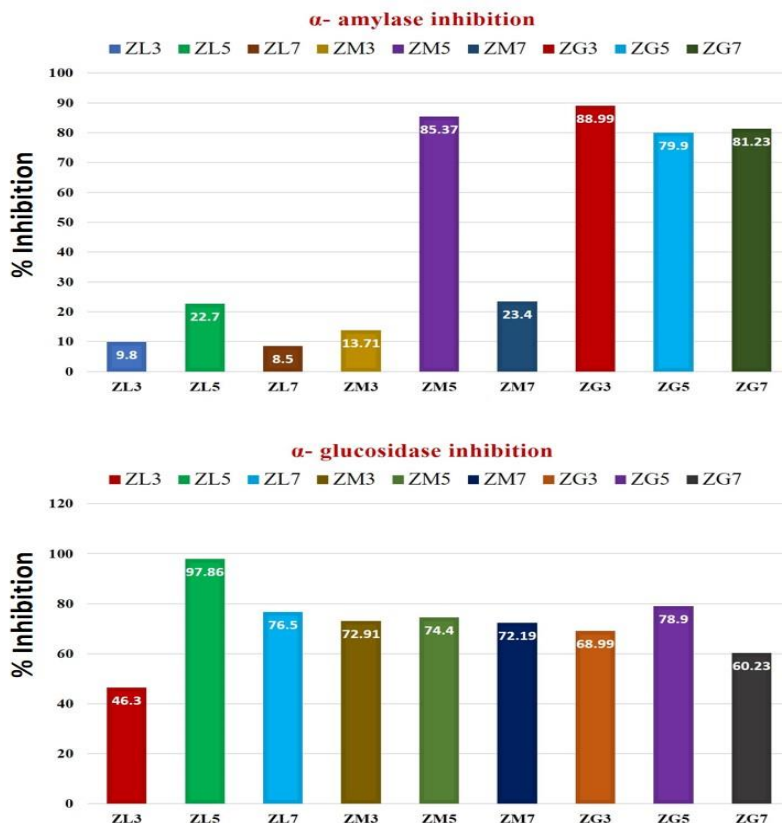
Fig. 7. Statistical summary of α-amylase and α-glucosidase inhibition by ZnO nanoparticles synthesized using *citrus lemon*extract, *Abelmoschus esculents* mucilage, and *Gliricidiasepium* leaf extract

> ➢ ZnO nanoparticles synthesised using *Gliricidiasepium* leaf extract display significant inhibition towards α-amylase. ZG3 have the maximum efficiency and found to be cytotoxic beyond 87.23μg/mL concentration. Higher SI value of the sample designate target selectivity and safety to normal cell lines.

> ➢ ZG3, ZG5 and ZG7 are moderate α-glucosidase inhibitors among which ZG5 have the maximum efficiency. The cytotoxic effect should be concerned for the concentrations higher than 83.51 μg/mL.

Since the SI obtained below 10, the sample may not be selective towsrds the target enzyme. Fig. 7 depicts the statistical summary of α-amylase and α-glucosidase inhibition by ZnO nanoparticles obtained.
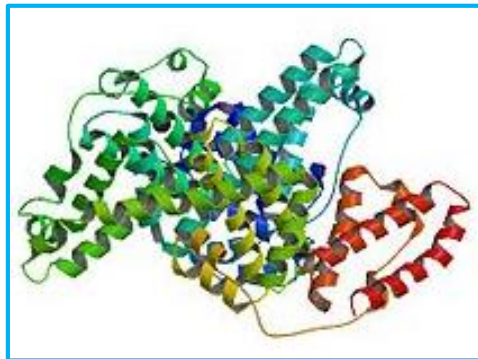
Reference

1.   R. Kitture, K. Chordiya, S. Gaware, S. Ghosh, P.A. More, P. Kulkarni, B.A. Chopade, S.N. Kale, J. Nanosci. Nanotechnol., 2016,15, 4046.

2.   R.D. Umrani, K.M. Paknikar, Nanomedicine, 2014, 9, 89.

3.   A. Nazarizadeh, S.A. Rezaie, AAPS Pharm. Sci. Tech., 2015, 17, 834.

4.   International Diabetic Federation, IDF Diabetes Atlas (Executive Summary), sixth edition, 2013, ISBN 2-930229-85-3 11.

5.   S. Ghosh, M. Ahire, S. Patil, A. Jabgunde, M. Bhat Dusane, B.N. Joshi, K. Pardesi, S. Jachak, D.D. Dhavale, B.A. Chopade, Evid.-Based Complementary Altern. Med., 2012, 2012, 929051.

6.   S.P. Sanap, S. Ghosh, A.M. Jabgunde, R.V. Pinjari, S.P. Gejji, S. Singh, B.A. Chopade, D.D. Dhavale, Org. Biomol. Chem., 2010, 8, 3307.

7.   S.S. Nair, V. Kavrekar, A. Mishra, Euro J. Exp. Bio., 2013, 3, 128.

8.   N. Shobha,N. Nanda, A. S. Giresha,P. Manjappa, P.Sophiya, K.K. Dharmappa,B.M. Nagabhushana, Mater. Sci. Eng. C, 2019, 97, 842.

9.   S. Gunalan, R. Sivaraj, V. Rajendran, Prog. Nat. Sci: Mater., 2012, 22, 693.

10.   F.M. Arvanag, A. Bayrami, A.H. Yangjehb, S.R. Pouran, Mater. Sci. Eng. C, 2019, 97, 397.

11.   E.S. Coimbra, J.A. Santos, L.L. Lima, P.A. Machado, D.L. Campos, F.R. Pavan, A.D. Silva, Chem. Soc., 2016, 27, 2161.

12.   I. Orme, Antimicrob. Agents Chemothe, 2001, 45, 1943.

13.   E.S. Dezaki, H. Mahmoudvand, F. Sharififar, S. Fallahi, L. Monzote, F. Ezatkhah, Pharm. Biol., 2016, 54, 752.

14.   B. Weninger, S. Robledo, G.J. Arango, E. Deharo, R. Aragon, V. Manoz, J. Callapa, A. Lobstein, R. Anton, J. Ethnopharmacol., 2001, 78, 193.

The electron-deficient metal and electron-rich biomolecule like proteins are assumed to have strong interaction. When nanoparticles enter in to a biological system, its surface gets covered with protein layers which is called corona. Therefore, a proper understanding and control on its physiological behaviour is crucial in the field of nanomedicine and environmental protection. Serum albumins contribute to the colloidal osmotic pressure of blood in major and manage the transportation of drugs and nutrition through our body and also responsible for drug deposition. Study of biomolecule interactions with metal is of great significance for the design of novel nano-drugs.

Chapter 5

ZnO-BSA interaction: in-vitro spectrofluorometric monitoring.

"If we can reduce the cost and improve the quality of medicinal technology through advances in nanotechnology, we can more widely address the medical conditions that are prevalent and reduce the level of human suffering."

Ralph Merkle

The study of nanoparticle-protein interactions has great research interest. It is essential to understand these interactions to achieve control on the physiological behaviour of the nanoparticles applied to the biological environment. Metal oxide nanoparticles are assumed to have strong interaction with the electron rich proteins resulting in corona formation when they are introduced in to the biological system. *In-vitro* studies with some model proteins are in common practice to understand these types of interactions. Serum albumin is a water-soluble globular protein [1-8]. Here we have studied the *in-vitro* interaction of ZnO nanoparticles developed with the Bovine Serum Albumin (BSA) model protein. The binding interaction with BSA was monitored from changes in the inherent fluorescent emission of BSA in presence of ZnO nanoparticles. The amino acids tryptophan and tyrosine are responsible for the fluorescence emission of BSA. Being a multicomponent system, synchronous fluorescence spectra was carried out in order to study the conformational changes of the fluorophores in BSA.

5.1. ZnO (ZL)-BSA binding interactions

Fig 1.A shows the changes observed in the fluorescence emission spectra of BSA with the increase in concentration of ZL3 sample. Upon the addition of ZnO nanoparticles, there is a significant quenching of fluorescence intensity of BSA at 347 nm was observed, 50.4% of intensity was reduced with insignificant changes in the wavelength. The considerable decrease in fluorescence intensity indicates the formation of certain complex between the ZnO nanoparticles and BSA. The fluorescence quenching is described by the Stern–Volmer relationship [9],

$$\frac{F_0}{F} = 1 + K_{SV}[Q] \tag{1}$$

where F^o and F demonstrate the fluorescence intensities in the absence and presence of quencher, respectively. [Q] is the quencher concentration and K_{sv} is a linear Stern-Volmer quenching constant, which is defined as $K_{sv} = k_q \times \tau_0$, where k_q is the bimolecular rate constant of the quenching reaction and τ_0 is the average integral fluorescence life time of BSA which is about 10^{-8} s. The values of quenching constant K_{sv} can be calculated using the plot of F^o/F versus[Q].
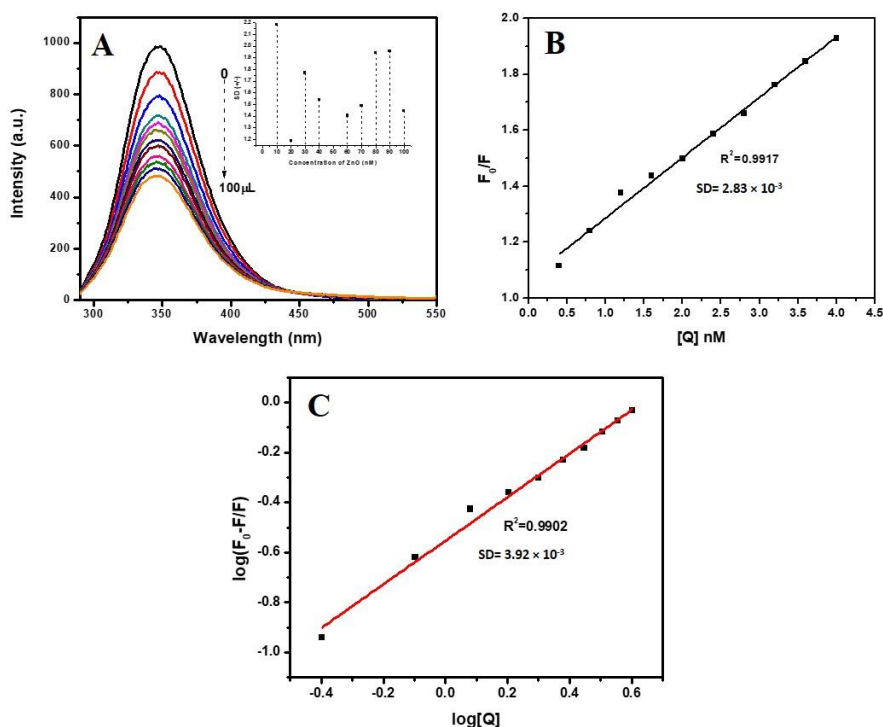
Fig. 1.A) Fluorescence emission spectra of BSA on the addition of increasing concentrations of ZL3 nanoparticles (Inset: Standard deviation at λmax 347nm), B) Stern-Volmer plot, and C) Scatchard plot.

When a small molecule binds independently on macromolecule, the equilibrium between free and bound molecule is represented by binding constant Scatchard equation [9], given below,

$$log[\frac{(F_0 - F)}{F}] = log\, K_b + n\, log[\,Q\,] \qquad (2)$$

where, K_b is the binding constant of the complex with BSA and n is the number of binding sites. From the plot of log $[(F_o\text{-} F)/F]$ versus log[Q], n value (a constant representing the binding sites) and the binding constant (K_b) value have been obtained. Fig. 1.B and C represents the Stern-Volmer and Scatchard plots respectively. The K_{SV}, k_q, K_b and n values are found to be $2.16{\times}10^8$ M^{-1}, $2.16{\times}10^{16}$ M^{-1} S^{-1}, 6.34×10^{11} L M^{-1}, 0.87 respectively which confirms the strong interaction of ZnO nanoparticle with BSA.

Tryptophan and tyrosine residues are responsible for the fluorescence property of BSA which are highly sensitive to the local environments [10]. Synchronous fluorescence spectroscopy provides valuable information on the molecular microenvironment of the fluorophores. The fluorescence spectral properties of tryptophan and tyrosine residues in BSA can be studied by taking synchronous spectra at the selected wavelength difference (Δλ). According to Miller theory, the wavelength difference between excitation and emission corresponds to the nature of chromophores [11]. The tryptophan and tyrosine residues have the Δλ of 60 and 15 nm respectively. The synchronous fluorescence spectra of BSA in the absence and presence of incremental addition of ZnO nanoparticles were recorded at both of these wavelength differences (Fig 2.A and B). With ZnO nanoparticles, the tyrosine (Δλ = 15 nm) and tryptophan (Δλ = 60 nm) fluorescence peak decreases by 50.91 and 61.31 % respectively. This observation shows that the introduction of ZnO nanoparticles perturbed the local microenvironment of tryptophan and

tyrosine residues of BSA. Moreover, the emission intensity of the residues decreased gradually with no considerable changes in characteristic wave length implying that the conformation is intact [12, 13].
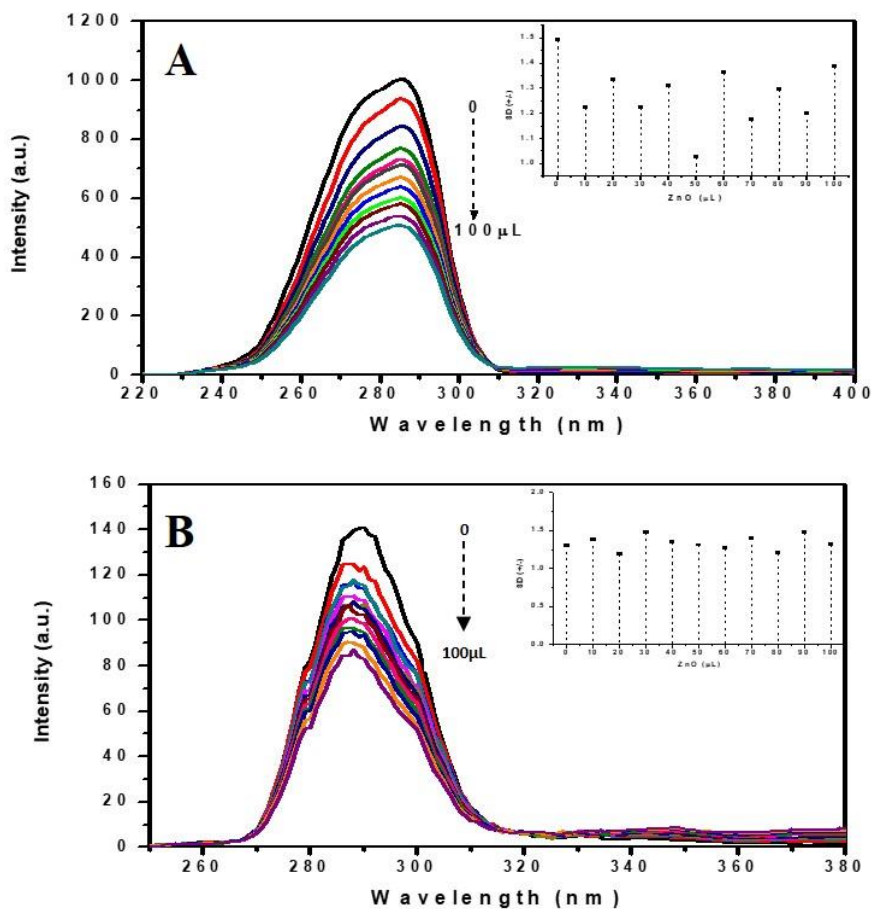

Fig. 2. Synchronous fluorescence spectra of (A) Tryptophan residue ($\Delta\lambda$ ¼ 60 nm) and B) Tyrosine residue ($\Delta\lambda$ ¼ 15 nm) on incremental addition of ZL3 nanoparticles (Inset: A) Standard deviation at λmax 285 nm, and B) λmax 289).

Fig 3 depicts the changes observed in the fluorescence emission spectra of BSA at 347 nm with the addition of ZL5 sample, corresponding Stern-

Volmer and Scatchard plots respectively. The fluorescence intensity of BSA was quenched to a great extent (70.2%) upon the gradual addition of ZL5 sample with negligible shift in λmax. The K_{SV}, k_q, K_b and n values for ZL5-BSA binding were determined to be 5.80×10^8 M^{-1}, 5.80×10^{16} M^{-1} S^{-1}, 5.91×10^{11} L M^{-1} and 0.84 respectively.
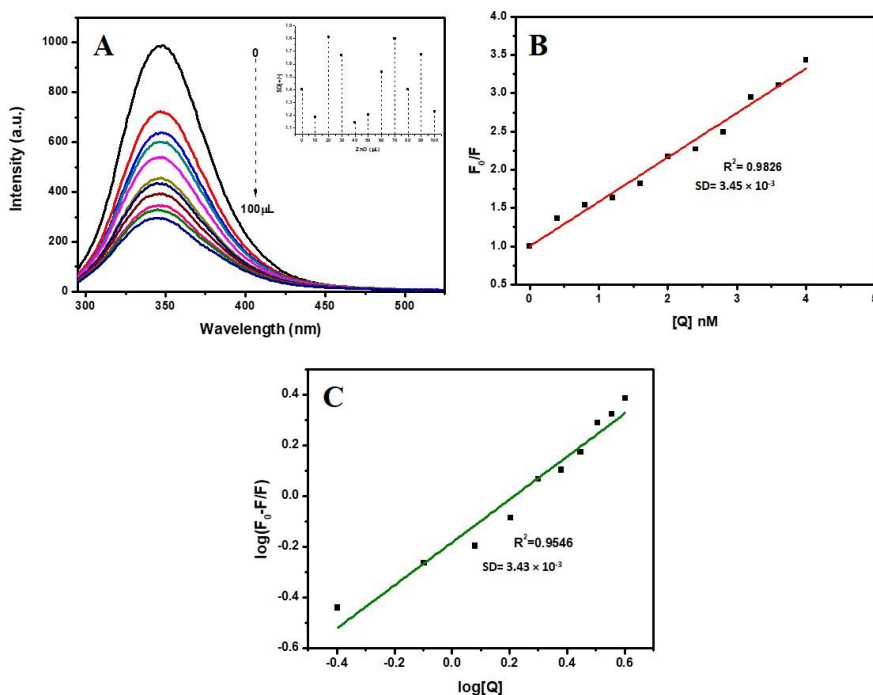

Fig. 3.A) Fluorescence emission spectra of BSA on the addition of increasing concentrations of ZL5 nanoparticles (Inset: Standard deviation at λmax 347nm), B) Stern-Volmer plot, and C) Scatchard plot.

The fluorescence intensity of tryptophan and tyrosine was quenched about 69.4% and 59.28% with the addition of ZL5 nanoparticle which indicate the perturbation at the local microenvironment of the respective amino acid residues. However, the emission spectra of tyrosine and tryptophan residues have negligible shift at characteristic emission wavelength. This observation

implies that the conformation of amino acid residues is intact during the interaction with nanoparticles. The fluorescence spectra of tryptophan and tyrosine residues are presented in Fig. 4.
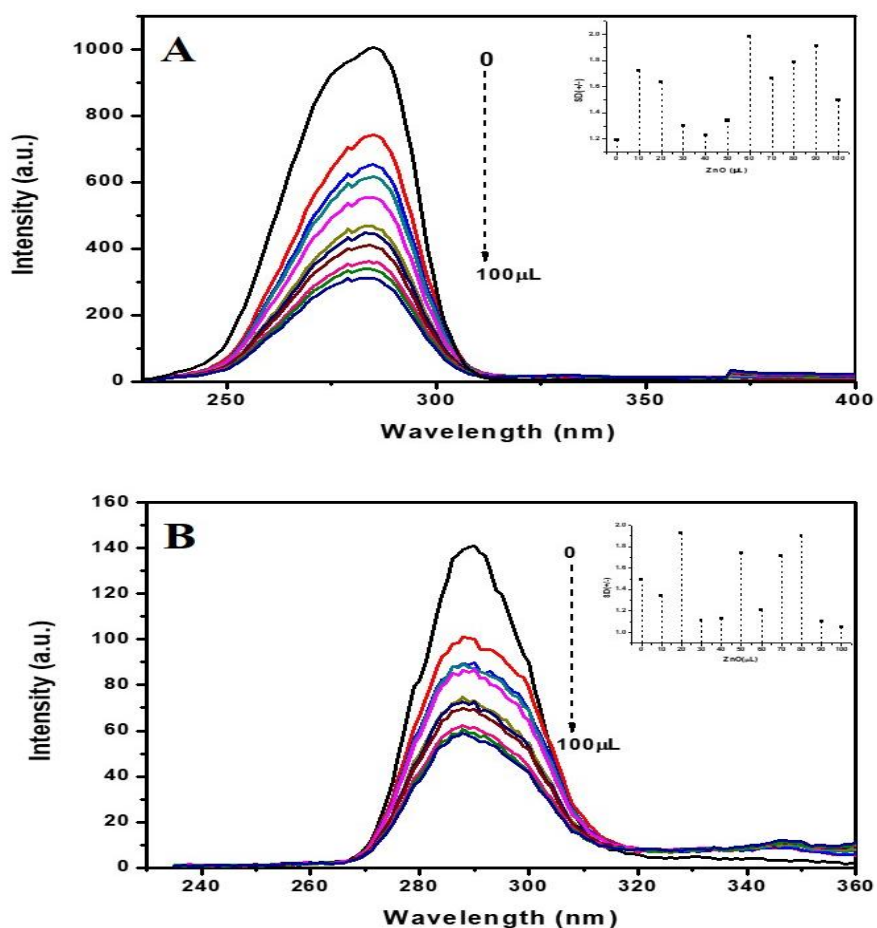

Fig. 4. Synchronous fluorescence spectra of (A) Tryptophan residue (Δλ ¼ 60 nm) and B) Tyrosine residue (Δλ ¼ 15 nm) on incremental addition of ZL5 nanoparticles (Inset: A) Standard deviation at λmax 285 nm, and B) λmax 289).

The fluorescence emission spectra of BSA at 347 nm with the addition of ZL7 sample is shown in Fig. 5. A. Corresponding Stern-Volmer and

Scatchard plots are depicted in Fig 5.B and C respectively. The fluorescence intensity of BSA was reduced 69.93% with the gradual addition of ZL7 sample and negligible shift in characteristic wavelengths were observed. From the Stern-Volmer and Scatchard plots the values for K_{SV}, k_q, K_b and n for ZL7-BSA binding were calculated to be 3.70×10^8 M^{-1}, 3.70×10^{16} $M^{-1} S^{-1}$, 3.74×10^{11} L M^{-1} and 0.87 respectively.

Fig. 6 shows the synchronous emission spectra of tryptophan and tyrosine residues and the changes in emission intensities due to the interaction with ZL7 nanoparticles. The emission intensities of the tryptophan and tyrosine were reduced to 58.99% and 51.06% respectively with the successive addition of nanoparticles. The emission peaks remined unshifted from the characteristic wavelengths of the residues indicating unaffected confirmation.
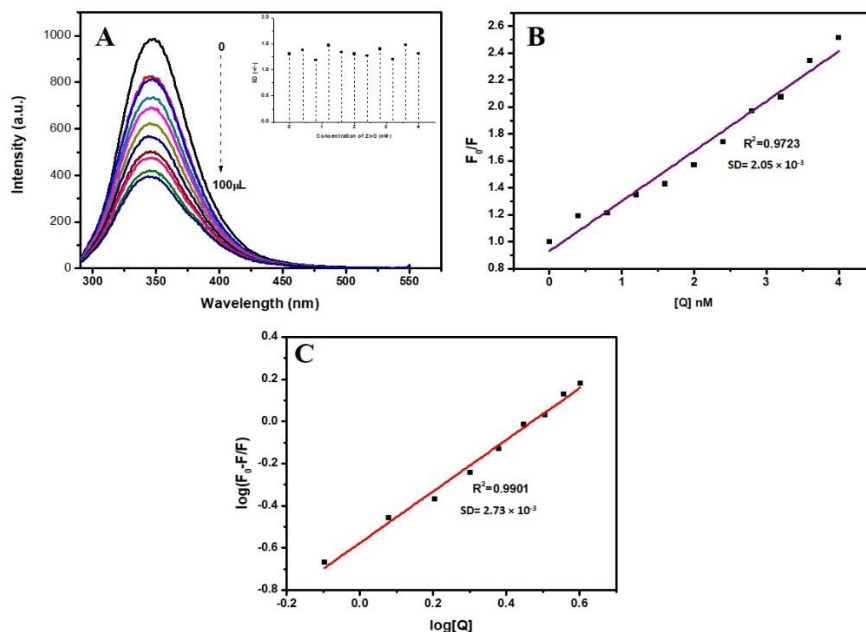

Fig. 5.A) Fluorescence emission spectra of BSA on the addition of increasing concentrations of ZL7 nanoparticles (Inset: Standard deviation at λmax 347nm), B) Stern-Volmer plot, and C) Scatchard plot.
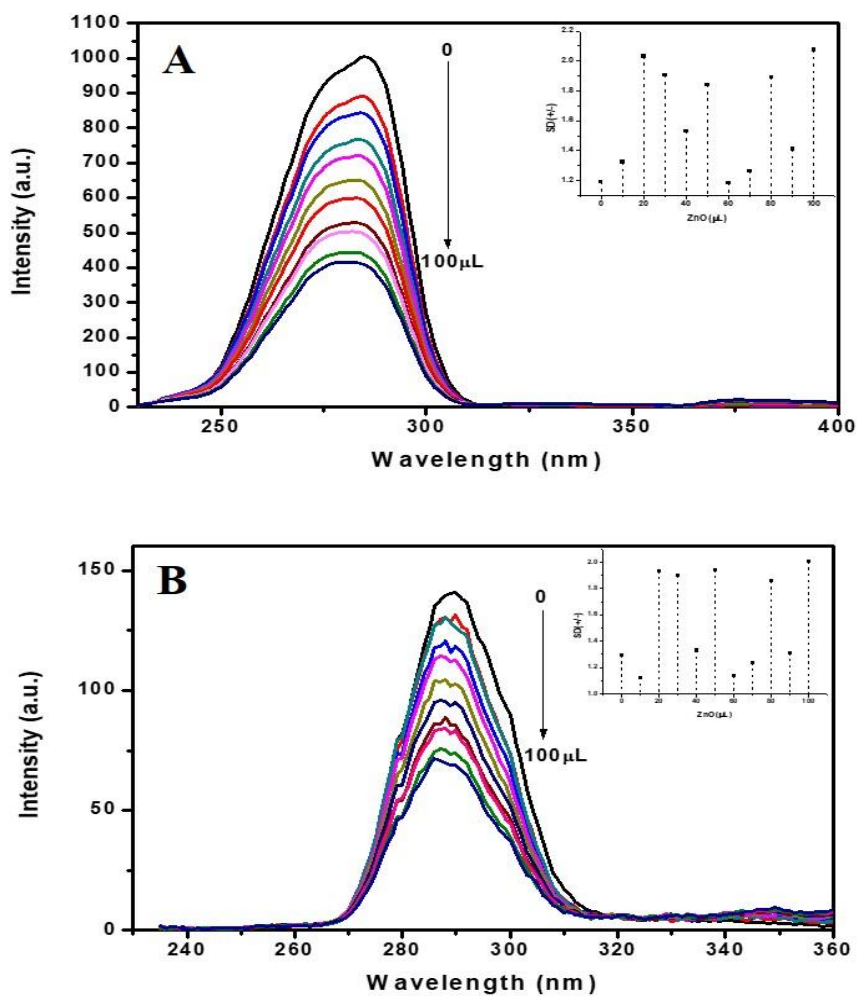
Fig. 6. Synchronous fluorescence spectra of (A) Tryptophan residue ($\Delta\lambda$ ¼ 60 nm) and B) Tyrosine residue ($\Delta\lambda$ ¼ 15 nm) on incremental addition of ZL7 nanoparticles (Inset: A) Standard deviation at λmax 285 nm, and B) λmax 289).

Here, ZnO nanoparticles prepared using the *citrus lemon* extract shows great extent of binding with the BSA protein. The samples ZL3, ZL5, and ZL7 exhibit 50-70% reduction in fluorescence emission of BSA and associated

fluorophores tryptophan and tyrosine. The order of BSA fluorescence quenching follows the order ZL5>ZL7>ZL3. Moreover, these interactions didn't interfere the conformation of the protein. Table 1 summarises the binding parameters for the ZL nanoparticles-BSA interaction.

Table 1. Binding parameters for ZL-BSA interaction

Sample	% reduction in BSA emission intensity	K_{SV} (M^{-1})	k_q $(M^{-1}S^{-1})$	K_b $(L\ M^{-1})$	n
ZL3	69.93	3.70×10^8	3.70×10^{16}	6.34×10^{11}	0.97
ZL5	70.20	5.80×10^8	5.80×10^{16}	5.91×10^{11}	0.84
ZL7	50.4	2.16×10^8	2.16×10^{16}	3.74×10^{11}	0.87

5.2. ZnO (ZM)-BSA binding interactions

The interaction of ZM samples (ZM3, ZM5, and ZM7) were studied with the changes in BSA fluorescence emission and the synchronous spectra. Fig. 7 represents the emission spectra of BSA, the Stern-Volmer and Scatchard plots derived for the ZM3 nanoparticles-BSA interaction. 71.84% reduction in fluorescence intensity of BSA was recorded by the successive addition of ZM3 nanoparticles inferring strong nanoparticle-protein binding. The binding parameters for the experimental set were derived from the Stern-Volmer and Scatchard plots. The values obtained for K_{SV}, k_q, K_b and n are 6.01×10^8 M^{-1}, 6.01×10^{16} $M^{-1}S^{-1}$, 4.23×10^{11} $L\ M^{-1}$ and 0.88 respectively.

The synchronous fluorescence spectra of BSA with addition of ZM3 nanoparticles recorded for the tyrosine ($\Delta\lambda = 15$ nm) and tryptophan ($\Delta\lambda = 60$ nm) residues are presented in Fig. 8. The percentage reduction in emission

intensities for tryptophan and tyrosine are 69.50% and 52.1% respectively. There was no shift in the characteristic emission wavelength observed for both the residues indicating the micro environment of the amino acid residues are perturbed without changing the confirmation of binding site/ protein.
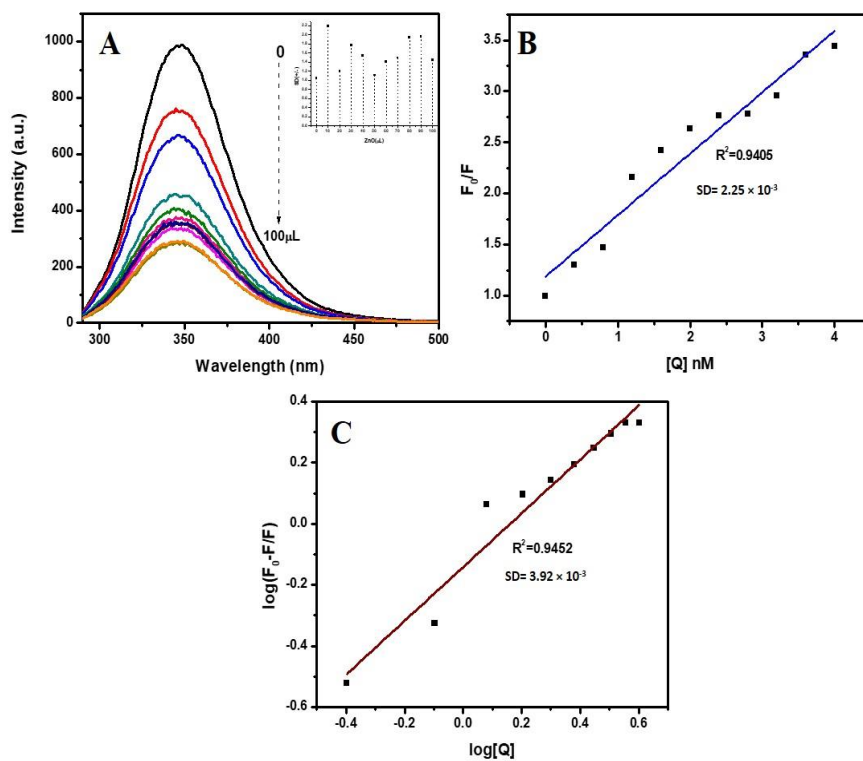

Fig. 7. A) Fluorescence emission spectra of BSA on the addition of increasing concentrations of ZM3 nanoparticles (Inset: Standard deviation at λmax 347nm), B) Stern-Volmer plot, and C) Scatchard plot.
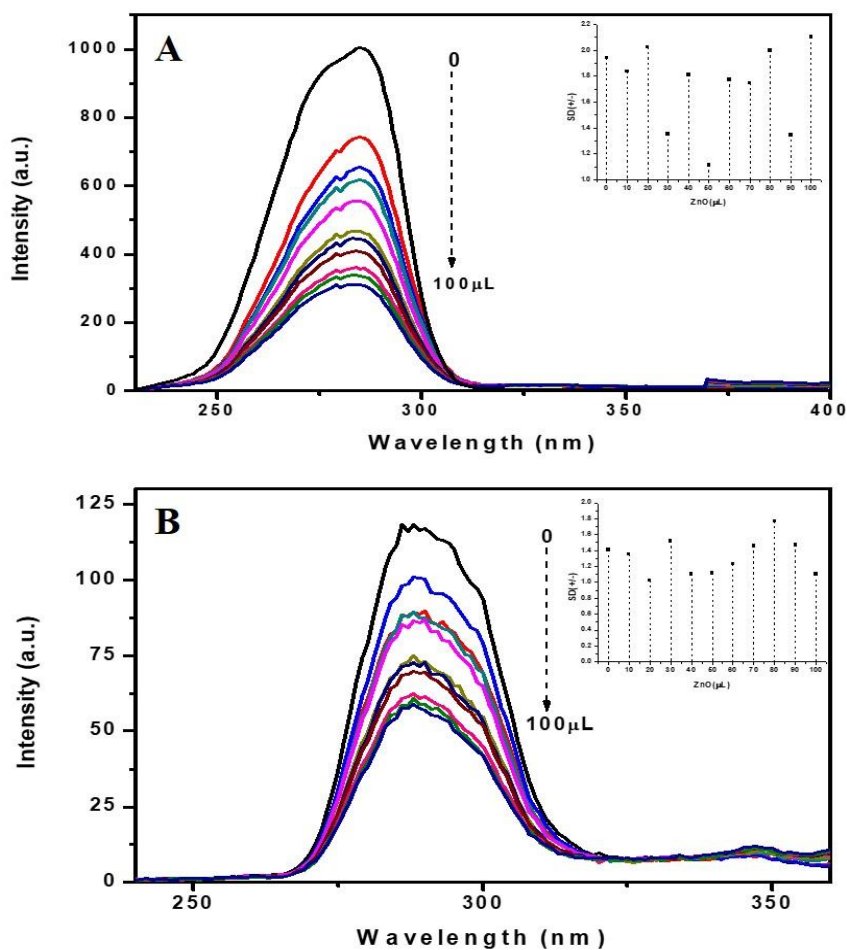
Fig. 8. Synchronous fluorescence spectra of (A) Tryptophan residue (Δλ ¼ 60 nm) and B) Tyrosine residue (Δλ ¼ 15 nm) on incremental addition of ZM3 nanoparticles (Inset: A) Standard deviation at λmax 285 nm, and B) λmax 289).

Fig. 9 depicts the changes observed in the fluorescence emission spectra of BSA at 347 nm with the consecutive addition of ZM5 sample, corresponding Stern-Volmer and Scatchard plots respectively. Here 41.91% reduction in the emission intensity of BSA was observed with the gradual addition of

ZM5 nanoparticles devoid of shift in the characteristic emission wavelength. The values of K_{SV}, k_q, K_b and n for the ZM5-BSA binding were determined to be 1.11×10^8 M^{-1}, 1.11×10^{16} M^{-1} S^{-1}, 1.32×10^{11} L M^{-1} and 0.75 respectively.
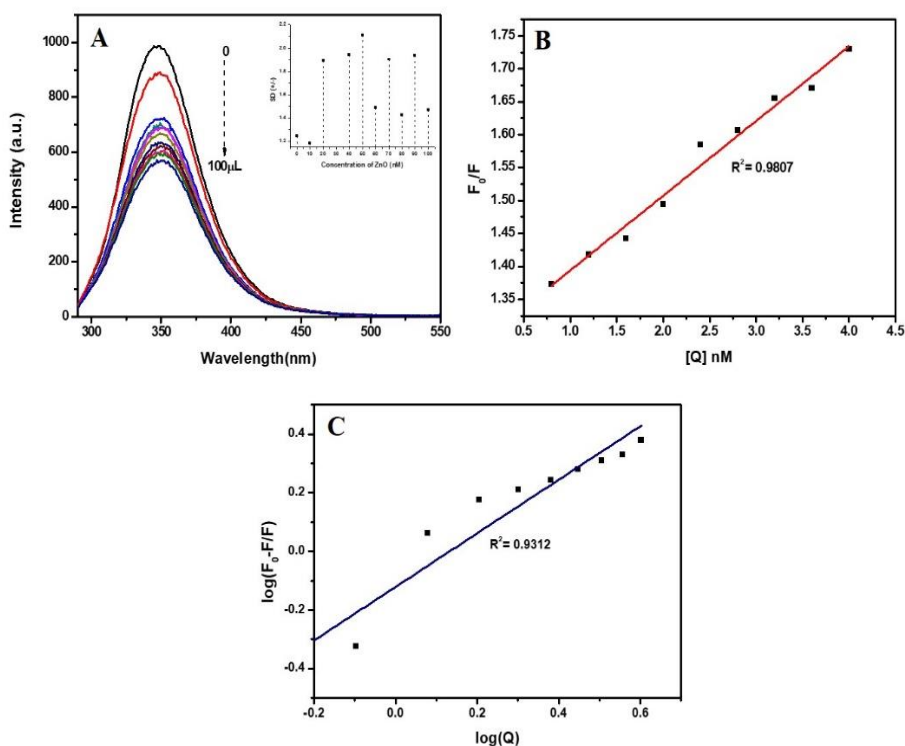

Fig. 9.A) Fluorescence emission spectra of BSA on the addition of increasing concentrations of ZM5 nanoparticles (Inset: Standard deviation at λmax 347nm), B) Stern-Volmer plot, and C) Scatchard plot.

The fluorescence emission intensity of tryptophan and tyrosine was decreased about 37.64% and 34.72% with the addition of ZM5 nanoparticle without considerable shift in their characteristic emission wavelengths which indicate the perturbation at the local microenvironment of the respective amino acid residues and the conformation of amino acid residues and the protein is

unaffected during the interaction with nanoparticles. The fluorescence spectra of tryptophan and tyrosine residues with the addition of ZM5 nanoparticles are shown in Fig. 10.
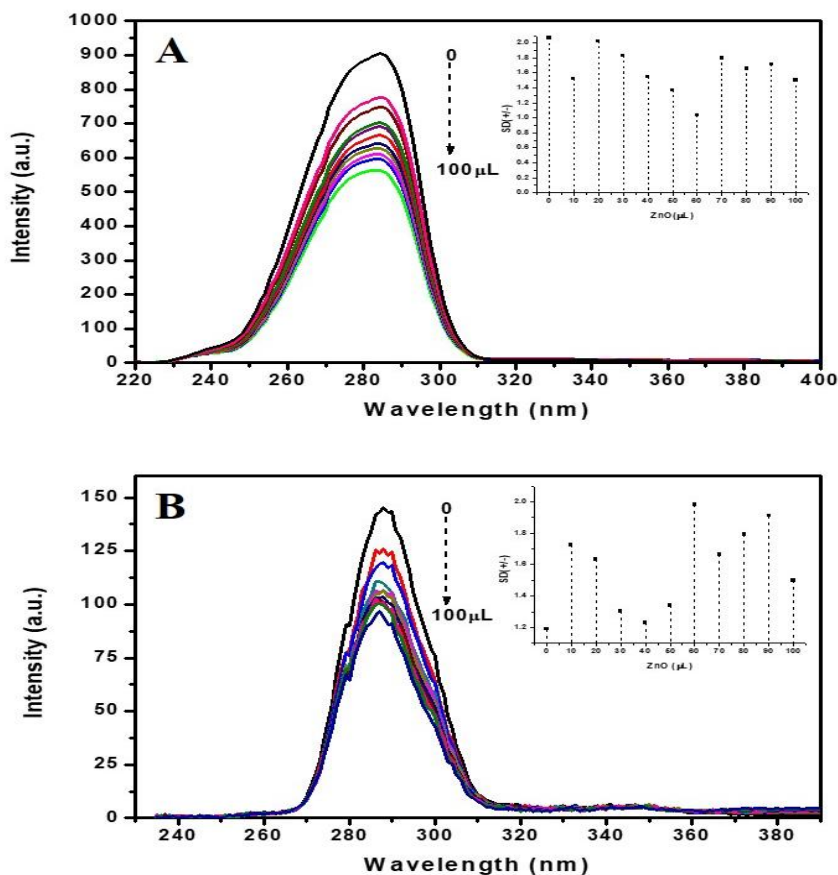

Fig. 10. Synchronous fluorescence spectra of (A) Tryptophan residue ($\Delta\lambda$ ¼ 60 nm) and B) Tyrosine residue ($\Delta\lambda$ ¼ 15 nm) on incremental addition of ZM5 nanoparticles (Inset: A) Standard deviation at λmax 285 nm, and B) λmax 289).

The fluorescence emission spectra of BSA at 347 nm with the addition of ZM7 sample is shown in Fig. 11. A. Corresponding Stern-Volmer and Scatchard plots are depicted in Fig. 11.B and C respectively. The fluorescence intensity of BSA was quenched 27.06% with the gradual

addition of ZM7 nanoparticles with negligible shift in characteristic wavelength. From the Stern-Volmer and Scatchard plots the values for K_{SV}, k_q, K_b and n for ZM7-BSA binding were calculated to be 7.21 $\times 10^7$ M^{-1}, 7.21×10^{15} M^{-1} S^{-1}, 8.68×10^{10} L M^{-1} and 0.81 respectively.

Fig. 12 shows the synchronous emission spectra of tryptophan and tyrosine residues and the changes in emission intensities due to the interaction with ZM7 nanoparticles. The emission intensities of the tryptophan and tyrosine were reduced to 37.04% and 15.38% respectively with the successive addition of nanoparticles. The emission peaks remined unshifted from the characteristic wavelengths of the residues indicating unaffected confirmation.
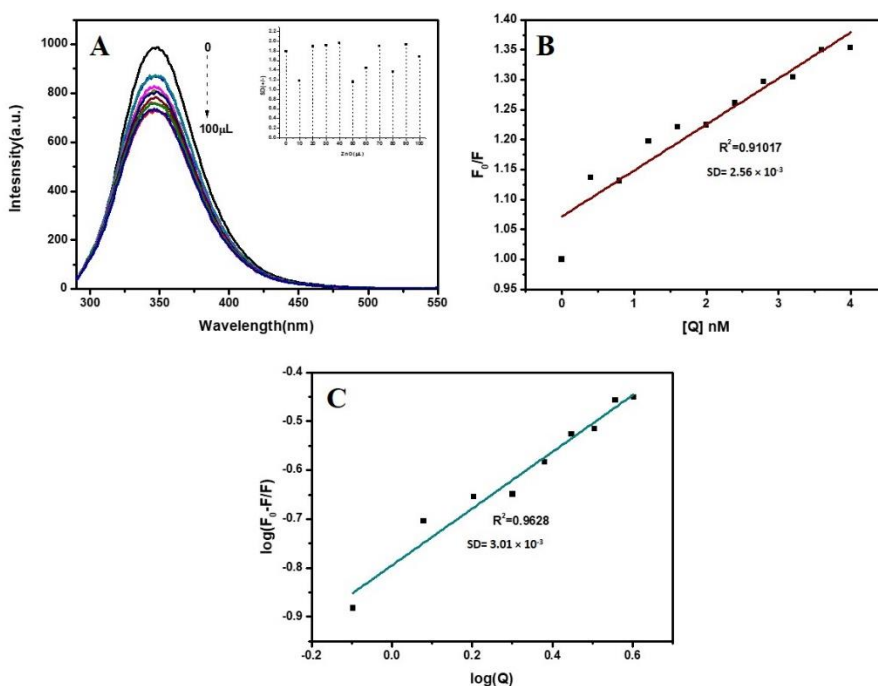

Fig. 11.A) Fluorescence emission spectra of BSA on the addition of increasing concentrations of ZM7 nanoparticles (Inset: Standard deviation at λmax 347nm), B) Stern-Volmer plot, and C) Scatchard plot.
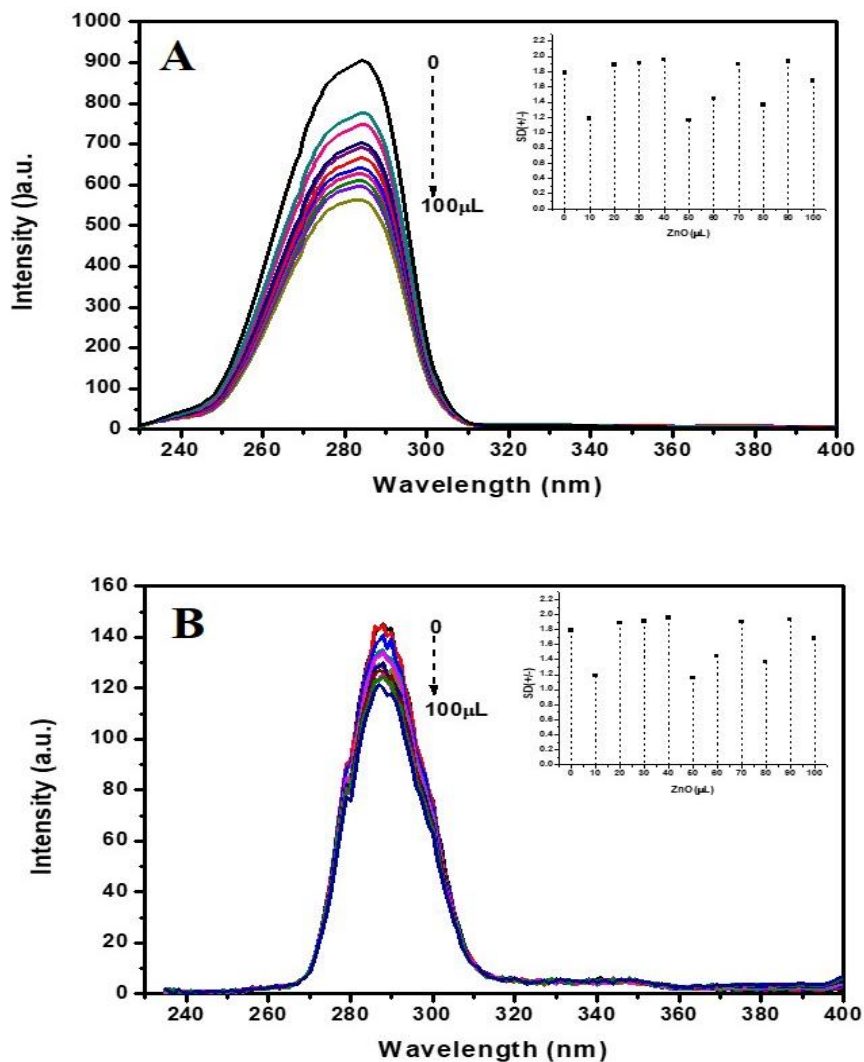
Fig. 12. Synchronous fluorescence spectra of (A) Tryptophan residue (Δλ ¼ 60 nm) and B) Tyrosine residue (Δλ ¼ 15 nm) on incremental addition of ZM7 nanoparticles (Inset: A) Standard deviation at λmax 285 nm, and B) λmax 289).

The ZnO nanoparticles ZM3, ZM5 and ZM7 synthesized using *Abelmoschus esculents* mucilage interact variably with the BSA protein. Here the quenching in fluorescence emission of BSA follows the order ZM3>ZM5>ZM7. There were negligible changes in the emission spectra of BSA, tryptophan and tyrosine residues during the interaction with ZM3, ZM5 and ZM7 nanoparticles which reveals the unchanged protein conformation. The binding parameters are summarized in Table2.

Table 2. Binding parameters for ZM-BSA interaction

Sample	% reduction in BSA emission intensity	K_{SV} (M^{-1})	k_q $(M^{-1} S^{-1})$	K_b $(L\ M^{-1})$	n
ZM3	71.84	6.01×10^8	6.01×10^{16}	4.23×10^{11}	0.88
ZM5	47.91	1.11×10^8	1.11×10^{16}	1.32×10^{11}	0.75
ZM7	27.04	7.21×10^7	7.21×10^{15}	8.68×10^{10}	0.81

5.3. ZnO (ZG)-BSA binding interactions

The interaction of ZG nanoparticles (ZG3, ZG5, and ZG7) with BSA was studied using the fluorescence emission of BSA and synchronous spectra. Fig. 13 depicts the changes in the emission spectra of BSA with the addition of ZG3 nanoparticles, corresponding Stern-Volmer and Scatchard plots. The percentage reduction in fluorescence intensity of BSA was 29.36% with the increase in concentration of ZG3 nanoparticles. The binding parameters ZG3-BSA interaction were calculated from the Stern-Volmer and Scatchard plots. The values obtained for K_{SV}, k_q, K_b and n are 4.33×10^7 M^{-1}, 4.33×10^{15} $M^{-1} S^{-1}$, 2.80×10^{10} L M^{-1} and 0.56 respectively.
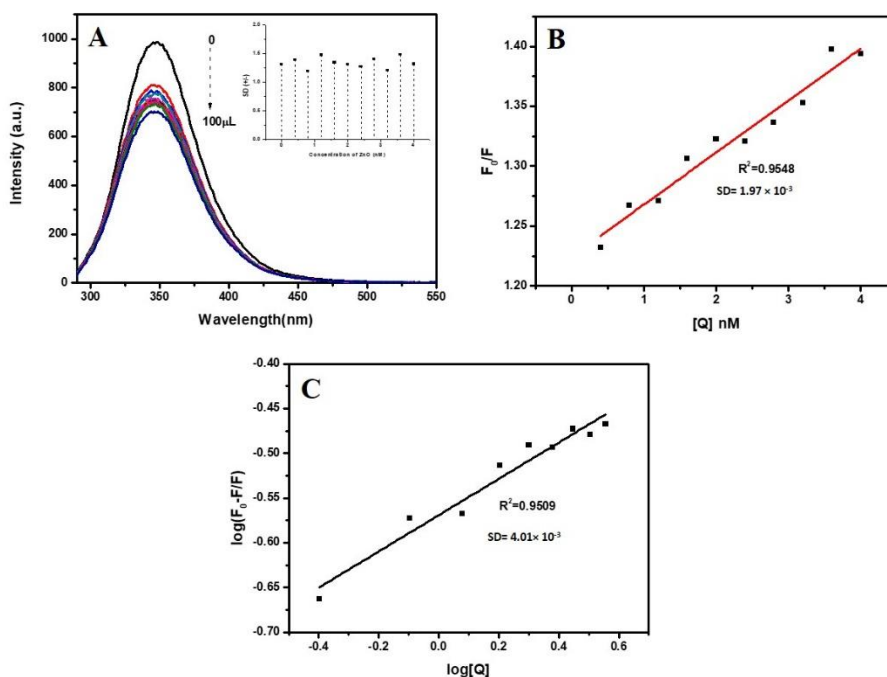
Fig. 13.A) Fluorescence emission spectra of BSA on the addition of increasing concentrations of ZG3 nanoparticles (Inset: Standard deviation at λmax 347nm), B) Stern-Volmer plot, and C) Scatchard plot.

The synchronous fluorescence spectra of BSA with addition of ZG3 nanoparticles recorded for the tyrosine (Δλ = 15 nm) and tryptophan (Δλ = 60 nm) residues are presented in Fig. 14. The emission intensities of tryptophan and tyrosine have 24.23% and 16.31% reduction respectively. There was no shift in the characteristic emission wavelength observed for both the residues indicating the micro environment of the amino acid residues are perturbed without changing the confirmation of the binding site/ protein.
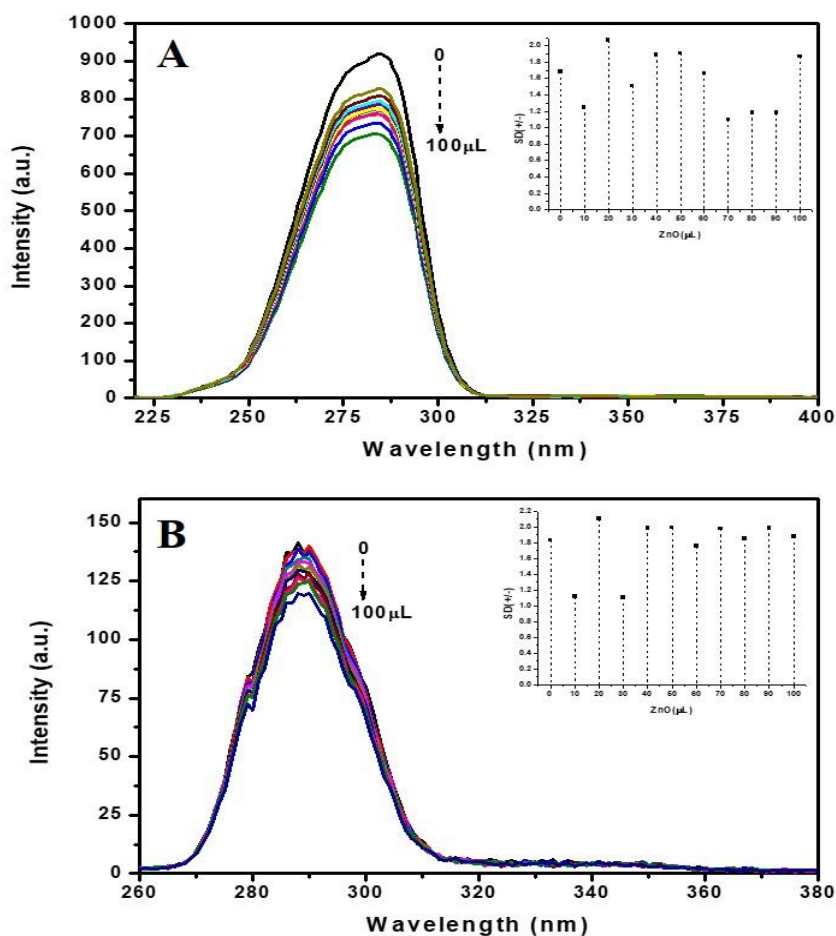
Fig. 14. Synchronous fluorescence spectra of (A) Tryptophan residue ($\Delta\lambda$ ¼ 60 nm) and B) Tyrosine residue ($\Delta\lambda$ ¼ 15 nm) on incremental addition of ZG3 nanoparticles (Inset: A) Standard deviation at λmax 285 nm, and B) λmax 289).

The fluorescence emission spectra of BSA at 347 nm with the addition of ZG5 nanoparticles is shown in Fig. 15. A. Corresponding Stern-Volmer and Scatchard plots are depicted in Fig. 15.B and C respectively. 62.85% of the fluorescence intensity of BSA was quenched by the successive addition of ZG5 sample and no remarkable changes in the characteristic wavelength was

noticed. The values of K_{SV}, k_q, K_b and n associated with the ZG5-BSA binding were calculated to be 3.76×10^8 M^{-1}, 3.76×10^{16} M^{-1} S^{-1}, 4.80×10^{11} L M^{-1} and 1.36 respectively.
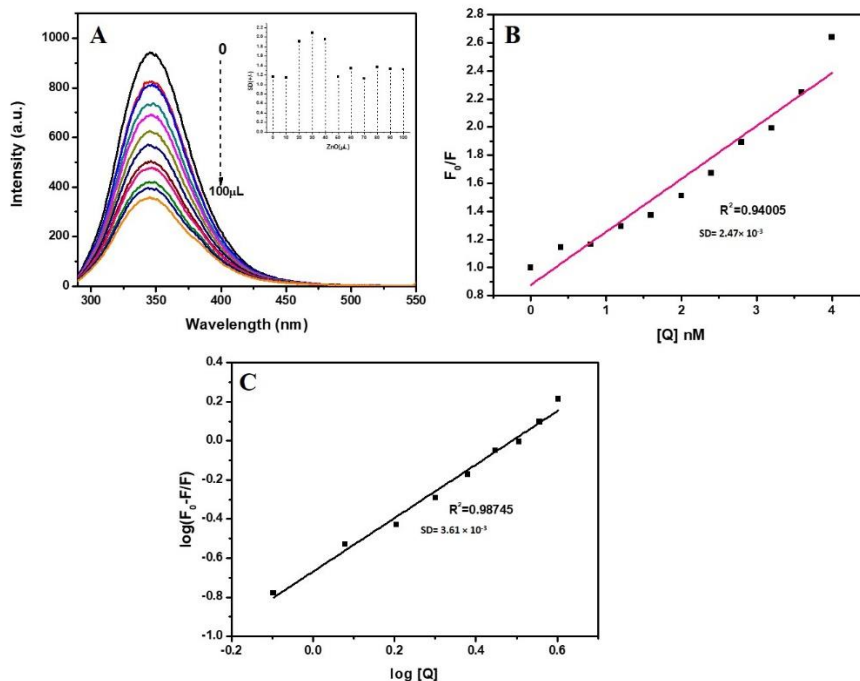

Fig. 15. A) Fluorescence emission spectra of BSA on the addition of increasing concentrations of ZG5 nanoparticles (Inset: Standard deviation at λmax 347nm), B) Stern-Volmer plot, and C) Scatchard plot.

Fig. 16 represents the synchronous emission spectra of tryptophan and tyrosine residues and the changes in emission intensities due to the interaction with ZG5 nanoparticles. The percentage reduction in emission intensities of the tryptophan and tyrosine are 66.73% and 59.57% respectively with the successive addition of nanoparticles. The emission peaks remined unshifted from the characteristic wavelengths of the residues infer the intact confirmation of protein and the residues.
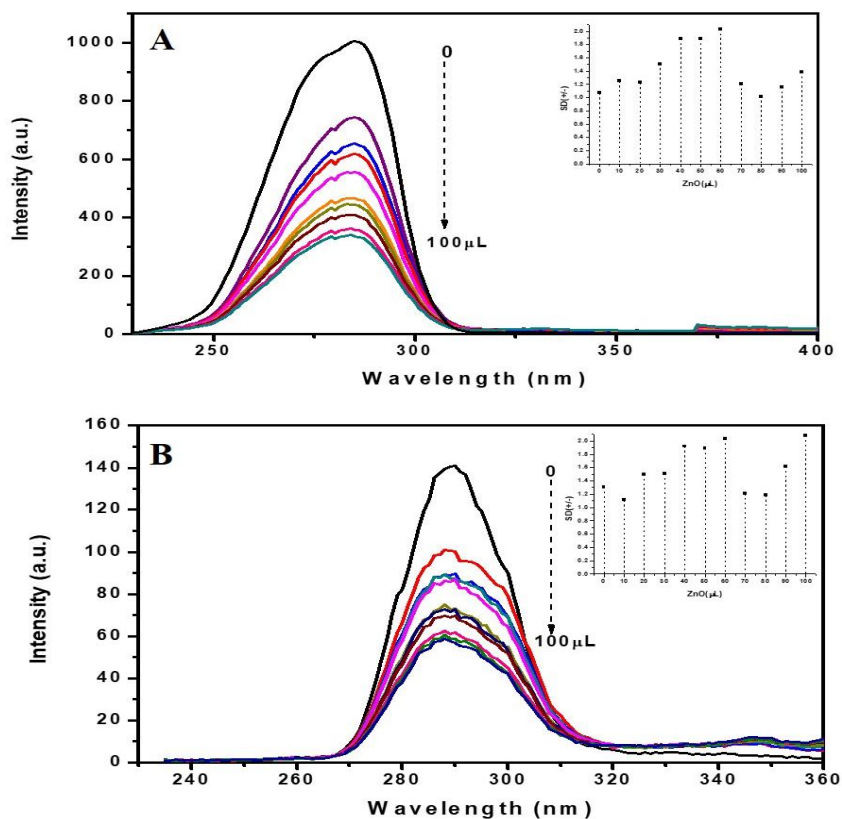
Fig. 16. Synchronous fluorescence spectra of (A) Tryptophan residue (Δλ ¼ 60 nm) and B) Tyrosine residue (Δλ ¼ 15 nm) on incremental addition of ZG5 nanoparticles (Inset: A) Standard deviation at λmax 285 nm, and B) λmax 289).

Fig. 17 shows the fluorescence emission spectra of BSA at 347 nm with the addition of ZG7 sample, corresponding Stern-Volmer and Scatchard plots respectively. Here 33.13% reduction in the emission intensity was observed with the gradual addition of ZG7 nanoparticles devoid of shift in the characteristic emission wavelength. The values of K_{SV}, k_q, K_b and n for the ZG7-BSA binding were determined from the Stern-Volmer and Scatchard plots to be 6.25×10^7 M^{-1}, 6.25×10^{15} M^{-1} S^{-1}, 1.73×10^{10} L M^{-1} and 0.68 respectively.
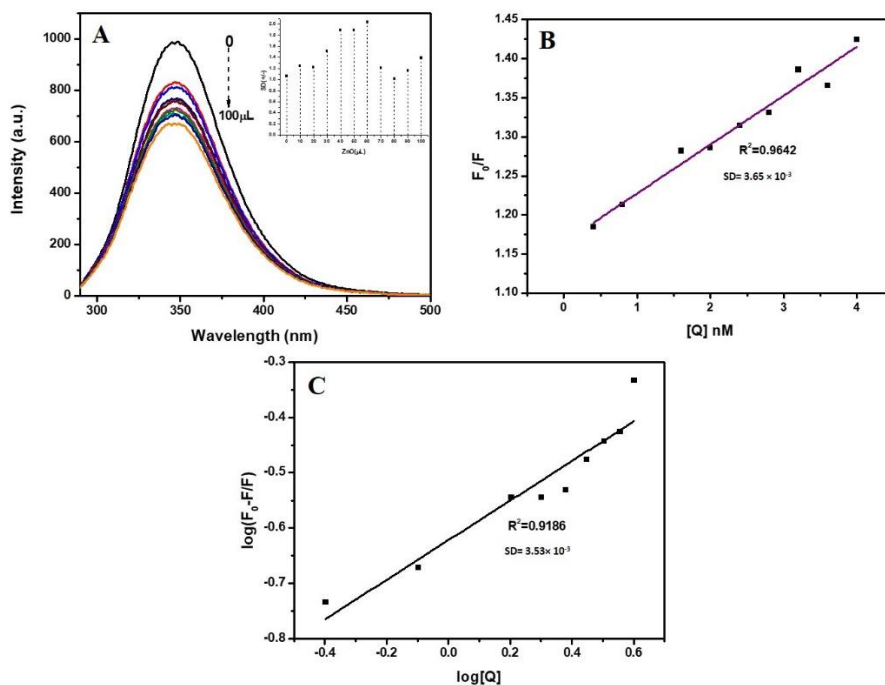
Fig. 17.A) Fluorescence emission spectra of BSA on the addition of increasing concentrations of ZG7 nanoparticles (Inset: Standard deviation at λmax 347nm), B) Stern-Volmer plot, and C) Scatchard plot.

The fluorescence emission intensity of tryptophan and tyrosine was decreased about 31.32% and 12.3% with the addition of ZG7 nanoparticles without considerable shift in their characteristic emission wavelengths which indicate the perturbation at the local microenvironment of the respective amino acid residues and the conformation of amino acid residues and the protein is unaffected during the interaction with nanoparticles. The fluorescence spectra of tryptophan and tyrosine residues with the addition of ZG7 nanoparticles are shown in Fig. 18.
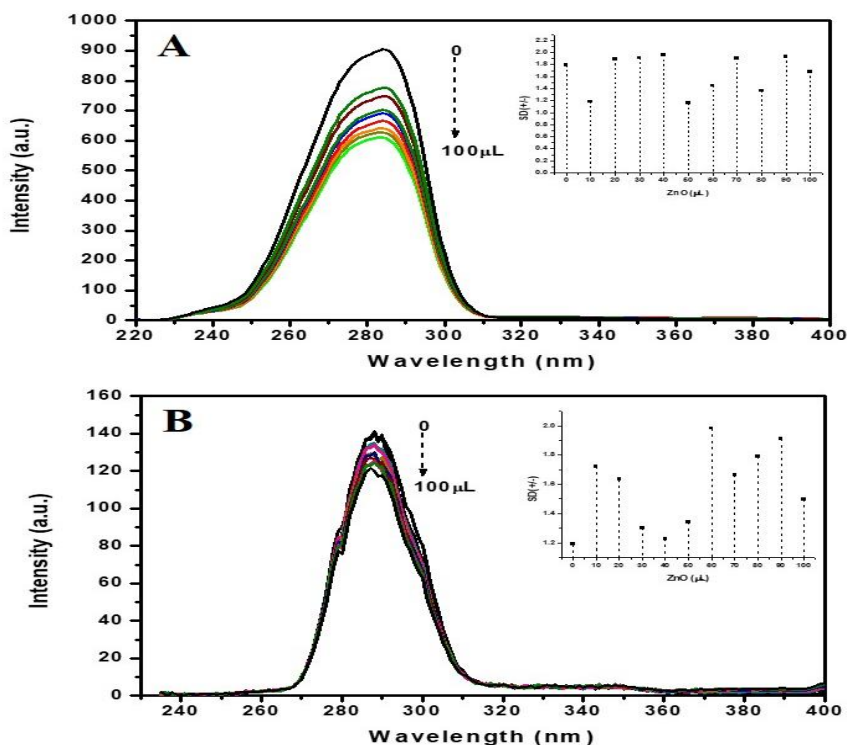
Fig. 18. Synchronous fluorescence spectra of (A) Tryptophan residue ($\Delta\lambda$ ¼ 60 nm) and B) Tyrosine residue ($\Delta\lambda$ ¼ 15 nm) on incremental addition of ZG7 nanoparticles (Inset: A) Standard deviation at λmax 285 nm, and B) λmax 289).

ZnO nanoparticles prepared using the *Gliricidiasepium* leaf extract ZG3, ZG5 and ZG7 have variable binding properties with the BSA protein. Addition of ZG5 sample cause the maximum quenching in the emission spectra of BSA while ZG3 and ZG7 have comparatively less interaction with the protein. The decrease in fluorescence intensity of BSA follows the order ZG5>ZG7>ZG3 and the samples doesn't interfere the conformation of the protein and associated fluorophores. The binding parameters associated with the ZM-BSA interactions are summarized in Table 3.

Table 3. Binding parameters for ZG-BSA interaction

Sample	% reduction in BSA emission intensity	K_{SV} (M^{-1})	k_q (M^{-1} S^{-1})	K_b (L M^{-1})	n
ZG3	29.36	4.33×10^7	4.33×10^{15}	2.80×10^{10}	0.56
ZG5	62.85	3.76×10^8	3.76×10^{16}	4.80×10^{11}	1.36
ZG7	33.13	6.25×10^7	6.25×10^{15}	1.73×10^{10}	0.68

5.4. Summary

➢ This chapter describes the interaction ZnO nanoparticles prepared using *citrus lemon* extract (ZL3, ZL5, and ZL7), *Abelmoschus esculents* mucilage (ZM3, ZM5, and ZM7) and *Gliricidiasepium* leaf extract (ZG3, ZG5, and ZG7) with BSA protein. Here, the changes in fluorescence emission spectra of BSA and its fluorophores tryptophan and tyrosine were monitored with the successive addition of ZnO nanoparticles.

➢ ZnO nanoparticles ZL3, ZL5, and ZL7 prepared using *citrus lemon* extract have shown good extend of binding with BSA. The fluorescence quenching of BSA follows the order ZL5>ZL7>ZL3. However, in presence of all the three samples, the emission intensity was reduced above 50%.

➢ For ZM nanoparticles the BSA fluorescence quenching follows the order ZM3>ZM5>ZM7. Unlike ZL samples, there is considerable difference in quenching capacity of the nanoparticles ranging from 27.04 to 71.84%. It could be associated with the differences in characteristics including size, crystallinity and surface charge of nanoparticles.

> ➢ The order of reduction in BSA fluorescence intensity follows ZG5>ZG7>ZG3 for the samples synthesized using *Gliricidiasepium* leaf extract. The percentage reduction in intensity varies from 29.36 to 62.85%.

> ➢ There were negligible changes in the emission spectra of BSA, tryptophan and tyrosine residues during the interaction with the ZnO (ZL, ZM, and ZG) nanoparticles indicating that the protein conformation remains intact.
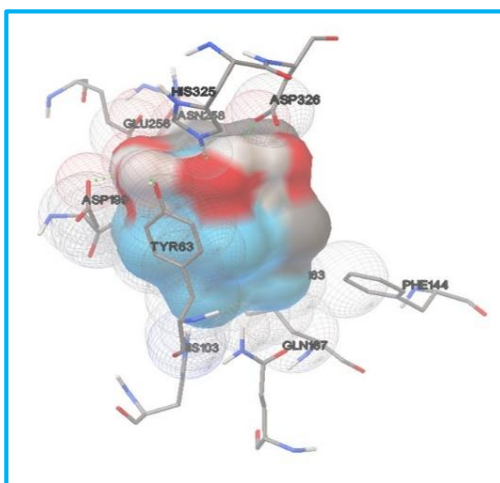
Reference

1. M. Muralisankar, S.M. Basheer, J. Haribabu, N.S.P. Bhuvanesh, R. Karvembu, A. Sreekanth, Inorg. Chim. Acta, 2017, 466, 61.

2. K. Jeyalakshmi, Y. Arun, N.S.P. Bhuvanesh, P.T. Perumal, A. Sreekanth, R. Karvembu, Inorg. Chem. Front., 2015, 2, 780.

3. S.R. Saptarshi, A. Duschl, A.L. Lopata, J. Nanobiotechnol., 2013, 11, 26.

4. A. Bhogalea, N. Patel, P. Sarpotdar, J. Mariam, P.M. Dongre, A. Miotell, D.C. Kothari, Coll. Surf. B Biointer., 2013, 102, 257.

5. Y.Z. Zhang, B. Zhou, Y.X. Liu, C.X. Zhou, X.L. Ding, Y. Liu, J. Fluoresc. 2008, 18, 109.

6. R.E. Oslon, D.D. Christ, Annu. Rep. Med. Chem., 1996, 3, 327.

7. B. Friedrichs, Th. Peters, Jr.: All about Albumin. Biochemistry, Genetics, and Medical Applications., Academic Press, New York, 1996.

8. K.A. Majorek, P.J. Porebski, A. Dayal, M.D. Zimmerman, K. Jablonska, A.J. Stewart, M. Chruszcz, W. Minor, Mol. Immunol., 2012, 52, 174.

9. S. Palaniappan, B. Narayana, Thermochim. Acta, 1994, 237, 91.

10. V.V.T. Padil, M. Cerník, Int. J. Nanomed., 2013, 8, 889.

11. A. Sonavane, A. Inamdar, H. Deshmukh, P. Patil, J. Phys. D Appl. Phys., 2010, 43, 315102.

12. G. Song, J. Han, R. Guo, Synth. Met., 2007, 157, 170.

13. L. Chu, M. Li, X. Li, Y. Wang, Z. Wan, S. Dou, D. Song, Y. Li, B. Jiang, RSC Adv., 205, 5, 49765.

Nanobiotechnology is an emerging interdisciplinary area of science for the twenty first century. The theoretical approaches using computational simulations can provide some complementary evidences for the binding of nanoparticles with the biomolecules, better understanding and visualization of the surface interactions. Computational modelling can be a guide to design nanomaterials for the future biomedical experiments. Moreover, theoretical calculations can provide a near-idea of these experimental results, rather than conducting numerous trials. Molecular docking helps to characterize the binding sites of target protein and thus to illustrate the biochemical processes.

Chapter 6

In-silico docking models of ZnO- biomolecule interactions.

"As technology advances, the boundaries between different disciplines of technology are blurring- such as what we are seeing with the use of nanotechnology and information technologies in health care delivery."

Ed Rudnic

Molecular docking is a bio-informatics modelling tool which provides the possible orientations of two or more molecules when they interact each other to form a stable adduct with minimum energy [1]. The docking models are capable of forecasting a three-dimensional view of any such complexes, the strength and type of interactions involved reliant on the binding characteristics of the ligand and target molecule [2-7]. It can generate a set of probable complex structures that are ranked by total energy, and assembled via scoring function software. The computational modelling experiments are extremely useful to conserve the wet-lab experimental time-line and cost [7-9].

A.E. Ledesma et.al has introduced the approach of computational docking studies to investigate the interactions in a protein and ZnO nanoparticles, for the first time ZnO clusters were generated to model the nanoparticles [10]. We have modelled the complexes of ZnO- α-amylase, ZnO- α-glucosidase, and ZnO-BSA. The basic hexagonal wurtzite structure of ZnO obtained from American metrological crystal data (AMC) and the three-dimensional ZnO crystal structures of dimensions 10, 30 and 50 nm (Z10, Z30 and Z50 respectively) were generated using the software Gauss View 6 and Mercury 3.8 version. The crystal structure of BSA was obtained from RCSB protein data bank (ID: 3V03). The chain A of 3V03 was used for the docking studies. The structure of α-amylase and α-glucosidase was not available in protein data bank. Hence, we have modelled their homologous 3-D structure using Easy Modeller 4.0 software. *In silico* docking studies were carried out using Autodock 4.2 version and the images were viewed in Accelry's Discovery Studio Visualizer version 4.0.

6.1. *In-silico* docking models of ZnO- α-amylase interaction

Fig. 1 depicts the docked models with least energy obtained for ZnO-α-amylase complexes. The Z10-amylase complex has negative binding energy value (-0.73 kcal/mol) indicating favourable interaction. However, as the dimension of ZnO (Z30 and Z50) increased positive binding energy values were obtained (32.18 kcal/mol and 452.22 kcal/mol respectively). The binding energy for ZnO- α-amylase association follows the order Z10< Z30<Z50. Z10 forms one hydrogen bond with the protein via -C=O group of tryptophan (TRP 321) residue in α-amylase. The H- bonding parameters were determined to be bond length 1.978 Å, bond angle 120.21º, dihedral angle 76.381º and bond energy -0.027kcal/mol. Fig. 2 reveals the near residue interactions involved in the ZnO- α-amylase association.
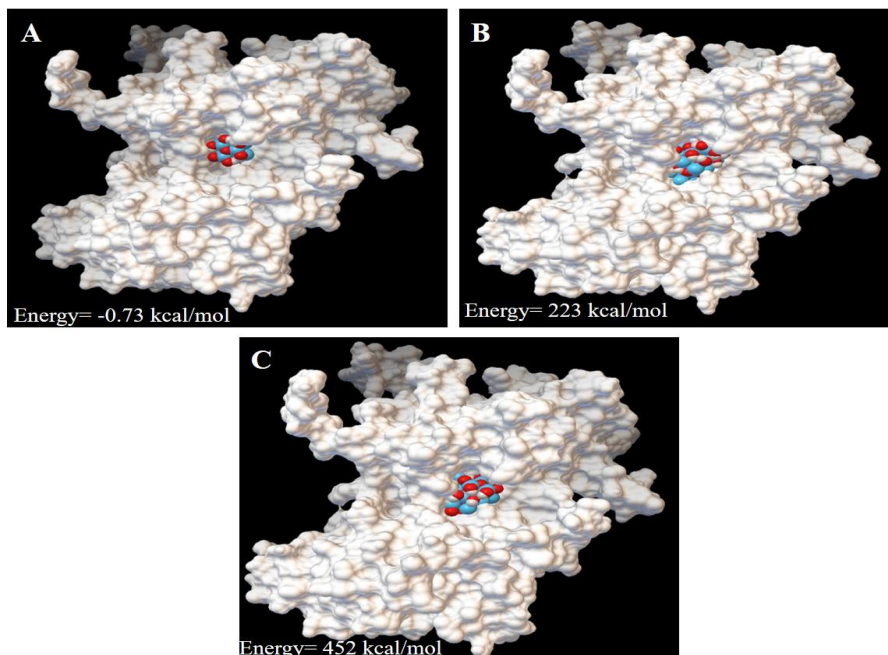

Fig. 1. Complex models generated for the interaction between A) Z10 B) Z30 and C) Z50 ZnO nanoparticles and α-amylase.
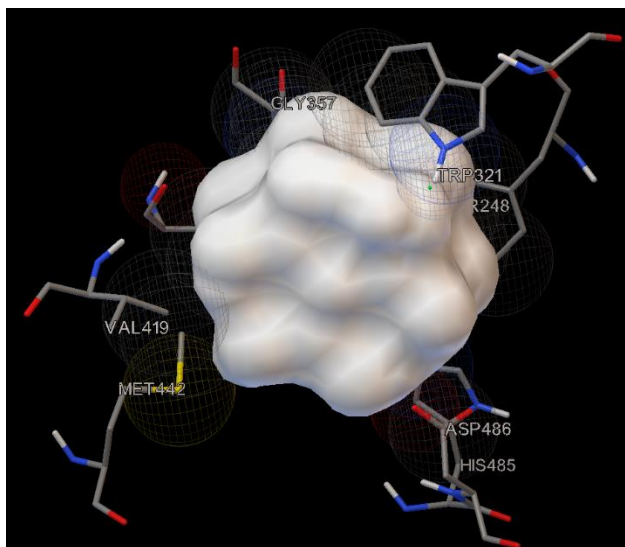
Fig. 2. Near residue interactions obtained for the Z10- α-amylase complex (green dots indicating H- bond formation).

The amino acids aspartic acid (ASP 486), histidine (HIS 485), methionine (MET 442), tryptophan (TRP 321), glycine (GLY 357), valine (VAL 419), glutamic acid (GLU 417), ASP 356, and tyrosine (TYR 248) are involved in the near residual interactions of Z10-α-amylase complex. Since no information regarding chemical interaction were obtained for the Z30 and Z50 docked models with amylase the nanoparticles should be physically interleaved into the amylase moiety. The binding energy values and limited interactions obtained with the in-silico docking studies on ZnO- α-amylase association thus suggest the ZnO nanoparticles to be mild inhibitors for the enzyme. Experimentally, ZnO nanoparticles prepared with citrus lemon extract (ZL3, ZL5, and ZL7) were very mild α-amylase inhibitors. Among the ZnO nanoparticles synthesised using *Abelmoschus esculents* mucilage, ZM5 exhibited strong α-amylase inhibition while others (ZM3, and ZM7) display very mild activity. The nanoparticles synthesised using

121

Gliricidiasepium leaf extract (ZG3, ZG5 and ZG7) have substantial inhibition. Thus, in experimental and theoretical monitoring the nanoparticles seem to be mild α-amylase inhibitors while the experimental exceptions should be concerned with the dependence of biological activity on morphology and crystallinity along with the dimension.

6.2. *In-silico* docking models of ZnO- α-glucosidase interaction

Docking studies were useful to find the interaction sites and size effect of the nanoparticles on α-glucosidase association. Fig. 3 shows the best docked models for ZnO-α-glucosidase complex obtained for Z10, Z30 and Z50 nanoparticles. The negative value of binding energy obtained for all three complexes indicates the favourable association of ZnO nanoparticles with the protein. The association of Z30- α-glucosidase possess least binding energy of -13.64 kcal/mol indicating most facile interaction and Z10 shows the least facile interaction with comparatively higher binding energy value (-7.83 kcal/mol). The binding energy for ZnO- α- glucosidase association follows the order ZL30< Z50< Z10. Fig. 4 reveals the near residue interactions of ZnO- α-glucosidase association. Z10 form three hydrogen bonds with the protein via -C=O and -NH groups in aspartic acid (ASP 46), and glycine (GLY 10) residues. The sample Z30 shows hydrogen bonds with glycine (GLY 10) and phenyl alanine (PHE 1) residues. Whereas Z50 forms hydrogen bonds with the amino acid residues aspartic acid (ASP 46), glutamic acid (GLU 286) and valine (VAL 325). The details of hydrogen bonding have been indexed in Table 1.
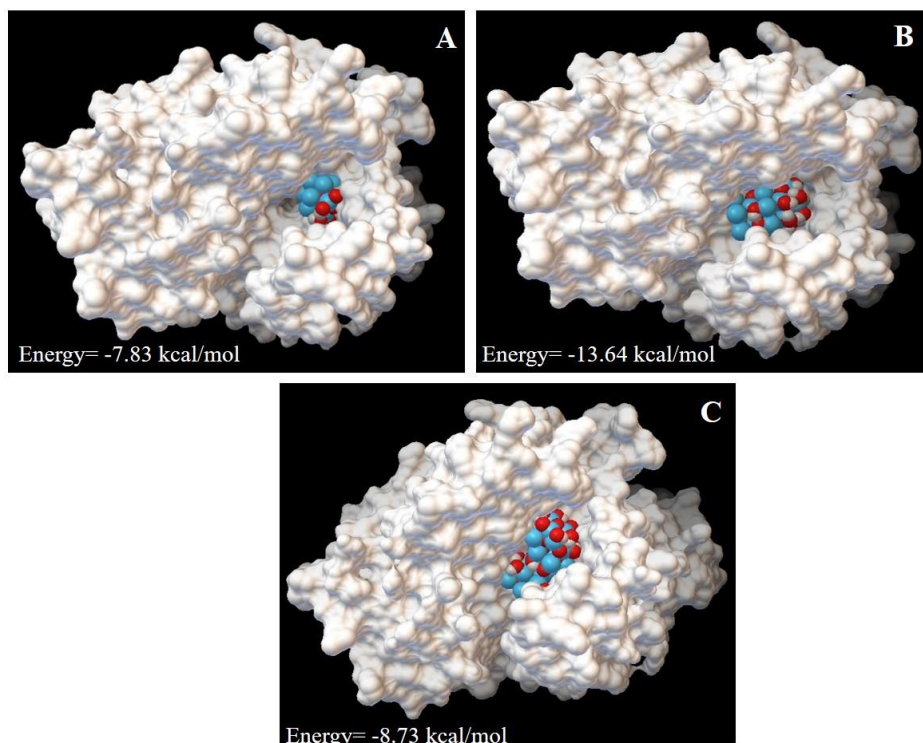
Fig. 3. Complex models generated for the interaction between A) Z10 B) Z30 and C) Z50 ZnO nanoparticles and α-glucosidase.

Owing to the favourable binding energies of ZnO-α-glucosidase complexes and chemical interactions revealed, *In-silico* docking studies recommend the nanoparticles to be strong α-glucosidase inhibitors. However, the size, shape and crystallinity of nanoparticle have crucial role in their biological interactions. The size and crystallinity varied with calcination temperatures. Experimentally, all the samples exhibited substantial inhibition efficiency towards α-glucosidase. ZnO nanoparticles synthesized using *citrus lemon* extract (ZL3, ZL5, and ZL7) were strong inhibitors for α-glucosidase enzyme. Moreover, they show selective inhibition and experimental and theoretical order of enzyme inhibition follows the same order. Similarly, ZM3, ZM5, and ZM7 samples obtained using *Abelmoschus esculents*

mucilage shows considerable and comparable activity towards α-glucosidase enzyme. ZnO nanoparticles prepared using *Gliricidiasepium* leaf extract (ZG3, ZG5, and ZG7) are moderate α-glucosidase inhibitors among which ZG5 have the maximum efficiency.
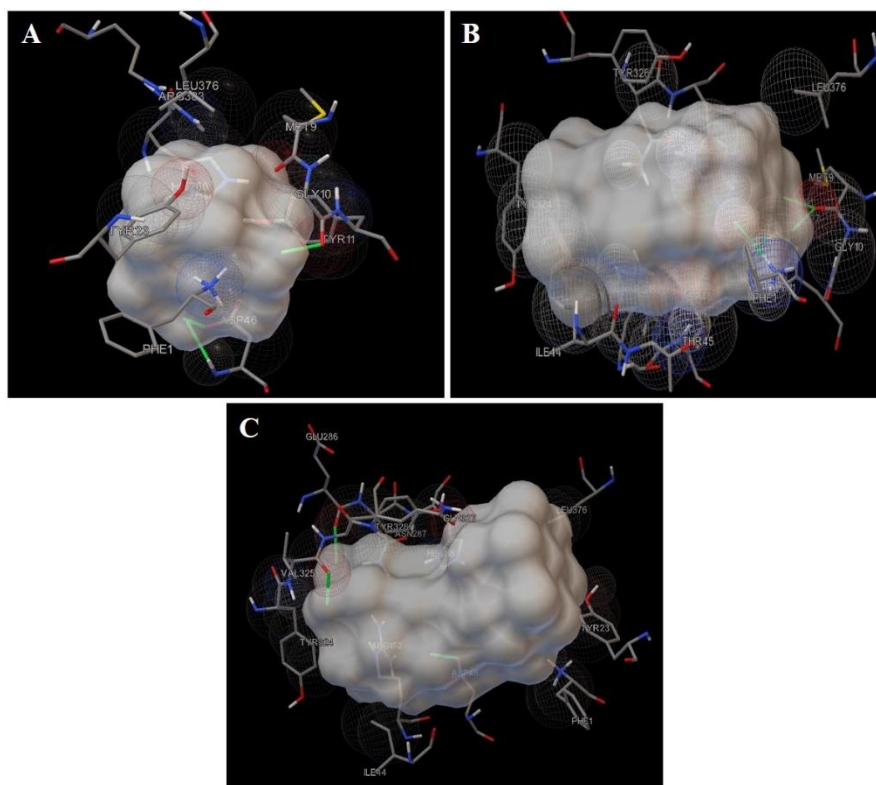

Fig. 4. Near residue interactions of ZnO- α-glucosidase complexes A) Z10, B) Z30 and C) Z50 (green dots indicating H- bond formation).

Table.1 Details of hydrogen bond parameters obtained for ZnO- α-glucosidase association.

Sample	Residue	Bond distance (Å)	Bond angle, θ (degree)	Dihedral angle, ϕ (degree)	Energy (kcal/mol)
Z10	ASP 46	1.734	132.435	117.154	-0.037
	GLY 10	1.849	132.584	104.723	-0.141
	ASP 46	2.068	137.905	105.901	-1.567
Z30	GLY 10	1.891	123.583	165.312	-0.529
	GLY10	1.827	144.281	136.655	-2.566
	PHE 1	2.006	163.473	115.553	-5.538
Z50	ASP 46	1.958	142.987	89.355	-0.001
	VAL 325	2.226	146.710	108.510	-0.337
	GLU 286	2.20	166.313	157.916	-3.492

6.3. *In-silico* docking models of ZnO- BSA interaction

Docking studies were employed to gather information about changes in microenvironment of protein in addition to that obtained from spectrofluorometric titrations. Different possible models for ZnO-BSA binding and the best docking models obtained are presented in Fig. 5. Z10-BSA complex has the least total energy value (-6.93 kcal/mol) indicating the most stable adduct formed. The total energy of the complexes was amplified with the increase in size of ZnO cluster and the total energy of BSA complexes with Z30 and Z50 determined to be 25.14 kcal/mol and 54.4 kcal/mol respectively. However, all three complexes have shown near-residue interactions (Fig. 6) where ZnO has been involved in hydrogen bonding with the amino acid residues present in the protein moiety. The details of hydrogen bonding have been indexed in Table 2.
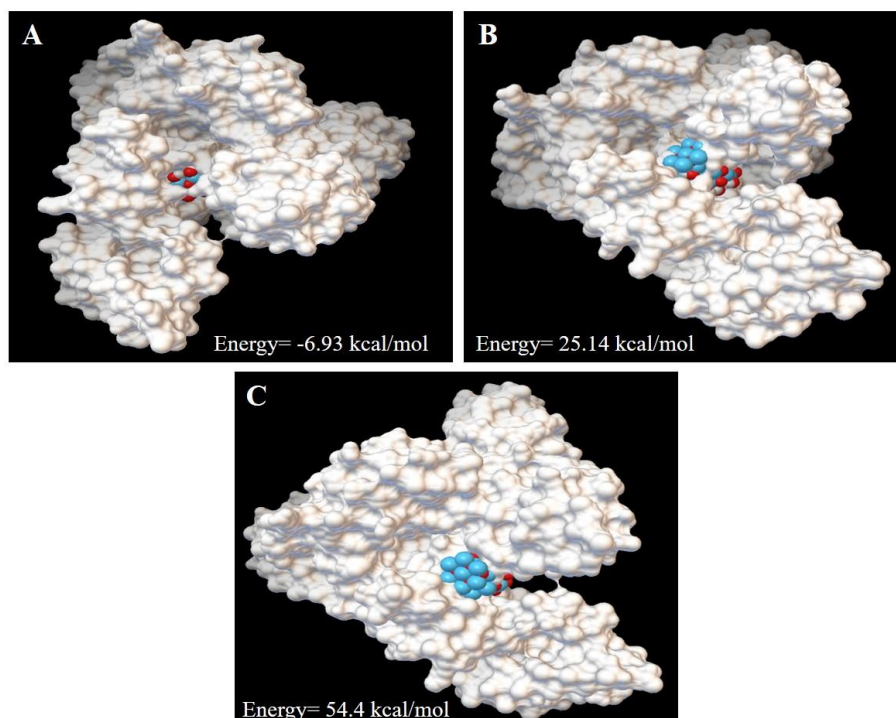
Fig. 5. Complex models generated for the interaction between A) Z10 B) Z30 and C) Z50 ZnO nanoparticles and α-BSA.

The amino acid residues serine (SER 428), lysine (LYS 431), isoleucine (ILE 455), leucine (LUE 454), alanine (ALA 193), tyrosine (TYR 451), threonine (THR 190) and glutamic acid (GLU 186) are present in the proximity of ZnO in Z10-BSA complex. Here, ZnO forms hydrogen bonds with SER 428 and THR 190 residues. In Z30-BSA complex, the near residue interactions involve TYR 451, SER 420, LYS 431, GLU 186, LYS 167, ILE 445, ALA 193, SER 192, arginine (ARG 458), THR 190, SER 192, LYS 187, GLU 186 and SER 428 is involved in hydrogen bonding. SER 192 and TYR 451 amino acid residues form hydrogen bond with ZnO in Z50-BSA complex and the amino acid residues LYS 431, ARG 435, GLU 424, histidine (HIS 145),

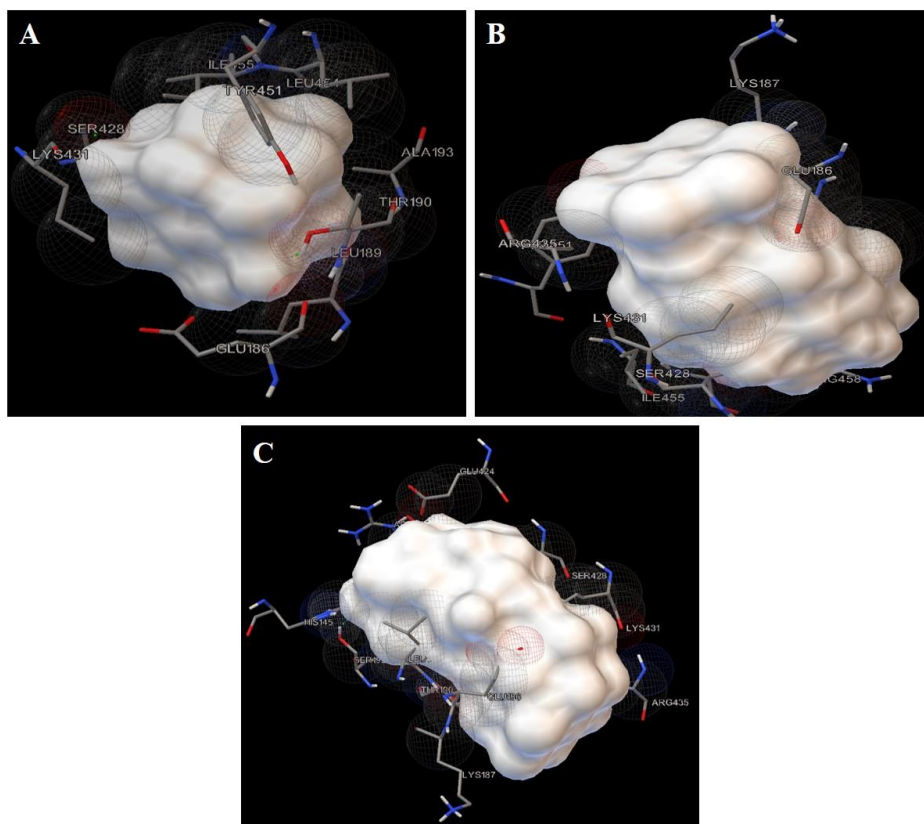LYS 187, GLU 186, ARG 458, GLU 424, SER 428, ILU 189, THR 190 and ALA 193 share the contiguous occupancy.

Fig. 6. Near residue interactions of ZnO- α-BSA complexes A) Z10, B) Z30 and C) Z50 (green dots indicating H- bond formation).

The docking results doesn't convey any interactions with the sulphur containing methionine and cysteine amino acid residues. The sulphur atoms could be masked such that it is difficult to take part in hydrogen bonding [2]. However, the docking studies found all the ZnO models are able to form stable complexes with BSA protein through hydrogen bonding interactions and the total energy of the system enter to positive values when the size of ZnO increased. Hence the interaction is most favourable at low particle

dimensions. The experimental results also correlate with this size factor. There is a discrepancy on the interactions with fluorophores (tryptophan and tyrosine residues) that they couldn't found in proximity of ZnO (only present in the near residue interactions of Z50). In fact, the molecular modelling gives the pretended orientations of the complexes depending on the binding characteristics of the structures we feed and in rigid frame the protein is treated.

Table 2. Details of hydrogen bond parameters obtained for ZnO- α-BSA association.

Sample	Residue	Bond distance (Å)	Bond angle, θ (degree)	Dihedral angle, φ (degree)	Energy (kcal/mol)
Z10	THR 190	2.12	129.123	88.042	-1.683
	SER 428	1.912	138.003	113.52	-0.601
Z30	SER 428	1.733	154.438	117.881	-0.363
Z50	SER 192	2.148	135.281	92.355	-0.277
	TYR 451	1.517	137.525	82.084	2.706

6.4. Summary

➢ Docking models were generated for ZnO- α-amylase, ZnO- α-glucosidase, and ZnO-BSA complexes. ZnO clusters of 10, 30 and 50 nm dimensions were generated using computational software. The structure of BSA was accessed from RCSB protein data bank, α-amylase and α-glucosidase were computationally modelled.

➢ The binding energy values and limited interactions obtained with the docking studies on ZnO- α-amylase association thus suggest the ZnO

nanoparticles to be mild inhibitors for the enzyme. Z10-amylase complex has negative binding energy value indicating favourable interaction while increasing the dimension of ZnO (Z30 and Z50) positive binding energy values were obtained. The binding energy for ZnO- α-amylase association follows the order Z10< Z30< Z50. Also, the chemical interactions were revealed for Z10 complex and no information regarding chemical interaction were obtained for the Z30 and Z50 docked models with amylase. Thus, the nanoparticles should be physically interleaved into the amylase moiety. The experimental and theoretical studies imply the nanoparticles to be mild α-amylase inhibitors while the experimental exceptions should be concerned with the dependence of biological activity on morphology and crystallinity along with the dimension.

➢ *In-silico* docking studies recommend the nanoparticles to be strong α-glucosidase inhibitors according to the negative binding energy values obtained for the three complexes and hydrogen bonding interactions obtained. Experimentally, all the samples exhibited substantial inhibition efficiency towards α-glucosidase even though selectivity and efficiencies vary. The binding energy for ZnO- α-glucosidase association follows the order Z30< Z50< Z10.

➢ Z10- BSA complex has the least total energy value indicating the most stable adduct formed. Higher binding energy values were obtained with ZnO of increased dimensions Z30 and Z50. The binding energy for ZnO- BSA complexes follows the order Z10< Z30< Z50. However, all the three complexes have shown chemical interactions (H-bonding) through different amino acid residues with ZnO indicating favourable association. Docking and experimental

investigations suggest the interaction is most favourable at low particle dimensions. The interaction with the BSA fluorophores, tryptophan and tyrosine were not revealed in the docking studies. In fact, the rigid molecular frame of protein assigned and the binding properties of provided structures matters.
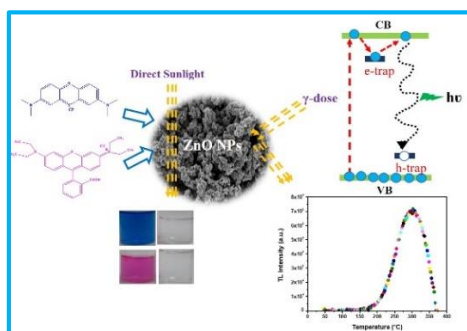
Reference

1. A.M. Dar, S. Mir, J. Anal Bioanal Tech, 2017, 8, 356.

2. G.M. Morris, R. Huey, W. Lindstrom, M.F. Sanner, R.K. Belew, D.S. Goodsell, A.J. Olson, J. Comput. Chem., 2009, 30, 2785.

3. S. Khan, A. Gupta, C.K. Nandi, J. Phys. Chem. Lett., 2013, 4, 3747.

4. R. Zhou, T. Weikl, Y. Ma, Nanoscale, 2020, 12, 10426.

5. R.Rohs, I. Bloch, H.Sklenar, Z.Shakked, Nucl Acids Res, 2005, 33, 7048.

6. I.A. Guedes, C.S. de MagalhãeS, I.E. Dardenne, Biophysical Reviews, 2014, 6, 75.

7. D. Seeliger, B.L. de Groot, J Comput Aided Mol Des, 2010, 24, 417.

8. B.K. Shoichet, S.L. McGovern, B. Wei, J.J. Irwin, CurrOpin Chem Biol., 2002, 6, 439.

9. M.L. Lamb, W.L. Jorgensen, CurrOpin Chem Biol., 1997, 1, 449.

10. A.E. Ledesma, D.M. Chemes, M.A. Frías, M.P.G. Appl. Surf. Sci., 2017, 412, 177.

The wastewater produced by dyeing industries have the highest level of toxicity, with cytotoxic, genotoxic, and mutagenic effects. Persistence of dyes even in small concentrations will inhibit the solar light penetration in to water which retards the photosynthetic action, stunt the biota growth thereby impart toxicity in aquatic life and makes the water source undesirable for usage. Serious attention and severe struggle should be paid to remove the dye pollutants from the contaminated media before its release in to natural streams. Photocatalytic degradation of dyes using UV/sunlight is a core method because it minimizes time, cost and can be undertaken in ambient conditions. Semiconducting nano zinc oxide is a renowned photocatalyst.

Chapter 7

ZnO nanoparticles: selective photodegradation, antibacterial activity, and thermoluminescence emission characteristics.

"There is no question that clean, affordable drinking water is essential to the health of our global community. But bottled water is not the answer in developed world, nor does it solve the problems for the 1.1 billion people who lack a secure waters supply. Improving and expanding existing water treatment and sanitation systems is more likely to provide safe and sustainable sources of water over the long term."

Emili Arnold

7.1. Photocatalytic degradation of Methylene blue and Rhodamine B

Industrial wastewater possesses non-biodegradable and organic dyes that are toxic to living organisms [1-3]. Photocatalytic degradation of dyes using UV/sunlight is a core method because it minimizes time, cost and can be undertaken in ambient conditions [4]. Photocatalytic degradation of organic pollutants is highly sought, because dye contaminants from various industries enter into the aquatic ecosystem, which affects the aquatic flora and fauna. Semiconducting nano zinc oxide is a renowned photocatalyst. The organic dyes Methylene blue (MB) and Rhodamine B (RhB) were subjected to photodegradation using the synthesized ZnO nanoparticles under UV and direct sunlight in order to investigate its photocatalytic activity. Photodegradation studies were undertaken after control experiments. The dyes were stirred in the dark for 1 h without the catalyst to monitor any changes in their concentrations due to surface phenomena such as adsorption. In addition, the dye solutions were tested to determine whether decomposition occurred under light illumination without the catalyst. No significant changes were observed in the dye concentration in both experiments. Thus, solutions containing 50 mg of the catalyst were introduced to the UVlight source and direct sunlight, and the changes in the absorption spectra of dyes under regular intermissions were documented.

7.1.1. ZnO photocatalyst synthesized using Citrus lemon extract

The photocatalytic degradation profiles of the MB and RhB dyes using the nanoparticle ZL7 are shown in Fig. 1.A-D. The concentrations of the dyes decreased gradually due to their degradation according to the declines in their

characteristic peaks located at λ_{max} = 660 nm and 550 nm for MB and RhB, respectively. The results indicated that 96.8% of MB and 95.8% of RhB were removed after 50 min due to the activity of the biogenic ZnO nanoparticles under UV light. Fig. 1.E and F shows the percentage degradation efficiency after each time interval. Conversely, the degradation of MB and RhB was complete (100%) under direct sunlight within 40 and 45 minutes respectively. According to the semiconductor photocatalysis, illumination of ZnO catalyst with appropriate UV-light having energy equal or more than the photo-threshold energy cause electronic excitations and consequent generation of electron-hole pairs.The electron–hole pairs generated by this photo-excitation process diffused to the surface of the catalyst, thereby reacting with the molecular oxygen and hydroxide ions to produce reactive radicals that facilitated the degradation of the organic dyes [5,6].

The photocatalytic degradation was analysed with 25–175 mg of the catalyst (Fig. 2.A). The increased population of reactive sites by adding more catalyst results in enhanced degradation efficiencies. However, increasing the catalyst load above 175 mg for MB and 125 mg for RhB, decreased the degradation efficiency due to particle sedimentation, thereby leading to a lack of reactive surface sites, or the turbidity of the suspension may have obstructed the passage of light and thus the activation of the catalyst [7-9]. Photodegradation of anionic methyl orange (MO) dye was monitored under UV and sunlight with ZnO nanoparticles and no visible change in colour or absorption spectra of MO was observed. Fig. 2.B shows the percentage degradation of MO (15 ppm) dye under light sources. Thus, the photodegradation was selective towards cationic dyes. The surface charge of ZnO nanoparticles was determined to be -31.52 mV in neutral solution.

Hence, the degradation was selective due to the electrostatic interaction between the negatively charged catalyst surface and cationic dye molecules.
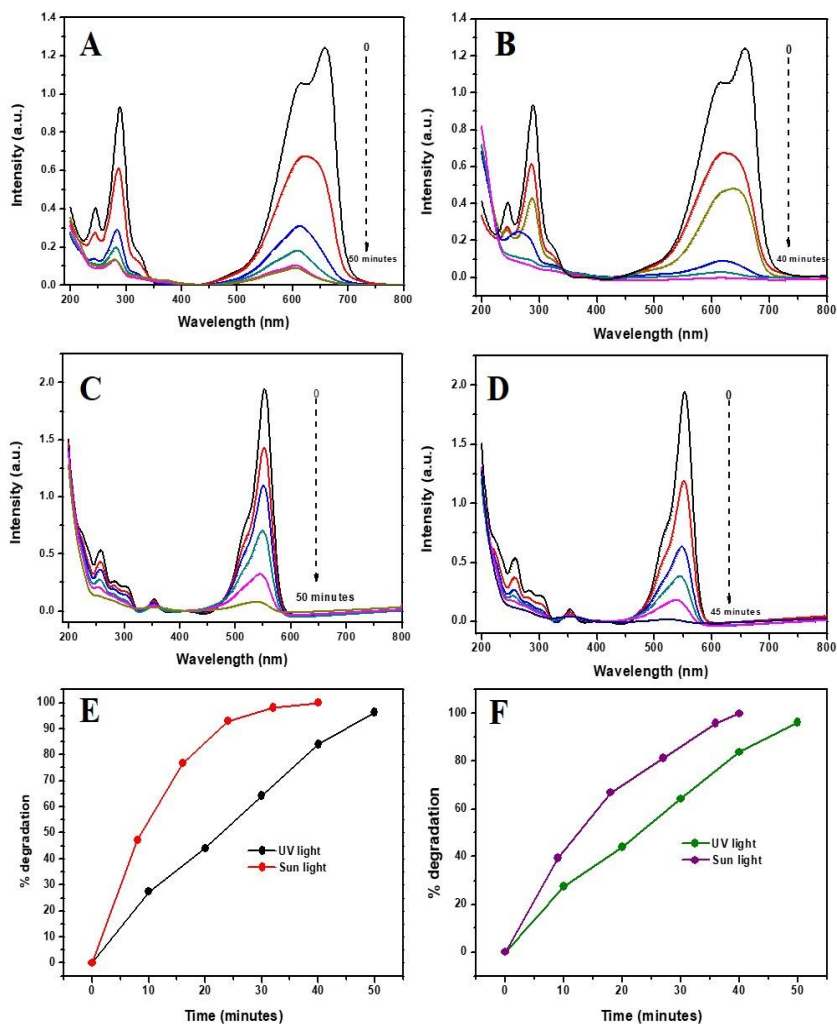

Fig. 1. Photodegradation profiles (pH ∼7, room temperature) for (A) MB under UV light (B) MB under sunlight C) RhB under UV light D) RhB under sunlight and percentage degradation efficiencies for E) MB and F) RhB under UV and sunlight light using ZL7 nanoparticles.
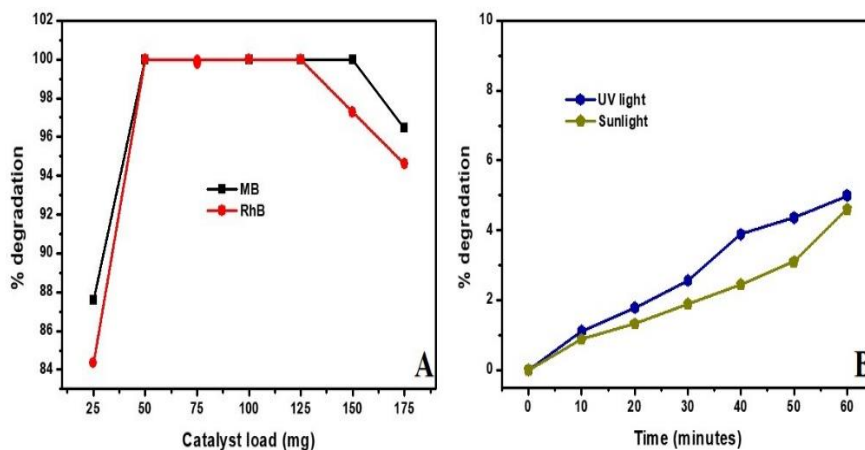
Fig. 2. A) Effect of catalyst (ZL7) loading on the degradation efficiency of MB and RhB under sunlight and B) degradation of MO under UV and sunlight.

During the photoexcitation of the semiconductor catalyst, different types of reactive species are generated including electrons (e^-) holes (h^+) and hydroxyl radical ($HO^\bullet$) and/or superoxide anion radical ($O_2^{\bullet-}$) resulting from the surface diffusion of e-h pairs [10, 11]. KI (for holes, h^+, and surface bounded hydroxyl radicals), ethanol (for electron e^-), sodium azide (for molecular oxygen O_2) and Isopropyl alcohol (IPA- for hydroxyl radicals, $\cdot OH$), scavengers were chosen to study their inhibitory effects during the process of photocatalytic degradation. Fig. 3.A display the effect of scavengers in the photodegradation of MB and RhB under direct sunlight. The degradation efficiency was considerably reduced in the presence of sodium azide, ethanol, and KI which indicates the electrons, holes/surface hydroxyl radicals and molecular oxygen play important role in the photodegradation of dye molecules.
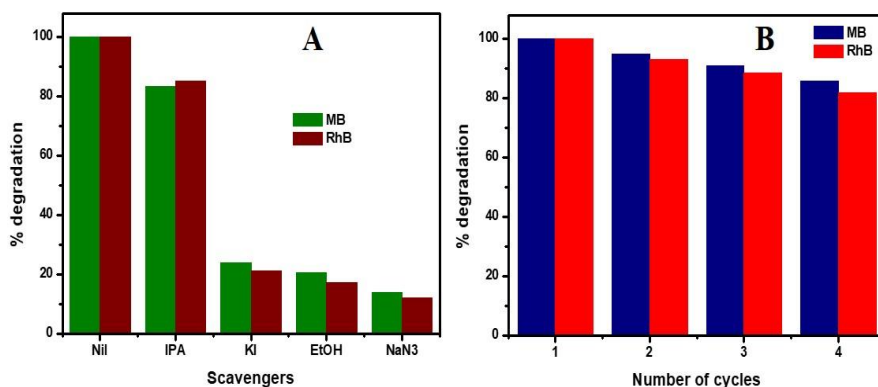
134

Fig. 3. A) Effect of scavengers on percentage degradation efficiencies of MB and RhB under direct sunlight and (B) recyclability of ZnO nanoparticles (ZL7) after four successive cycles of MB and RhB photodegradation under direct sunlight.

The reusability of a photocatalyst is very important for large-scale applications. Fig. 3.B shows the recyclability of ZnO after MB and RhB degradation under identical conditions upon natural-sunlight irradiation. An unavoidable loss of a small amount of the catalyst occurred during repeated cycles but, even so, the activity of the sample was reduced only minimally. After consecutive degradation for four cycles, the photocatalyst remained stable and retained high degradation efficiencies, 85.6% and 81.67% for MB and RhB respectively thereby ensuring reusability.

7.1.2. ZnO photocatalyst synthesized using *Abelmoschus esculents* mucilage

The ZnO sample ZM7 synthesized by using *Abelmoschus esculents* mucilage was employed as photocatalyst under UV and direct sunlight. Fig. 4.A-D represents the photocatalytic degradation profile of MB and RhB under UV and sunlight illumination. The intensities fall at characteristic $\lambda max = 660$ nm

and λmax = 550 nm can be well observed. Both exhibit gradual decrease in concentration due to their degradation as indicated by the depression in characteristic peaks after regular time intervals exposed under the light sources in presence of catalyst. The status of percentage degradation of the target dye molecule has been shown in Fig. 4.E and F.
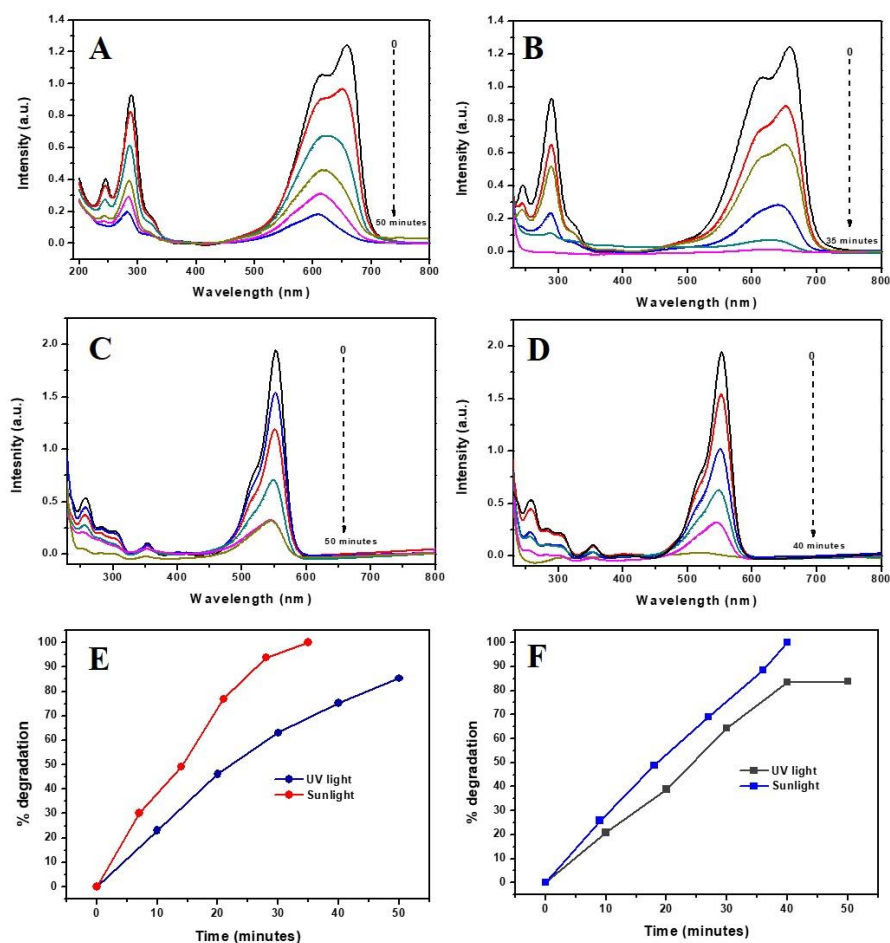

Fig. 4. Photodegradation profiles (pH ~7, room temperature) for (A) MB under UV light (B) MB under sunlight C) RhB under UV light D) RhB under sunlight and percentage degradation efficiencies for E) MB and F) RhB under UV and sunlight using ZM7 nanoparticles.

Under UV light 85.36% of MB molecules were removed from the solution within 50 minutes whereas the degradation was complete in 35 minutes under direct sunlight. The degradation of RhB is almost complete after 40 minutes under sunlight exposure while only 83.93% of the dye molecules were removed under UV light within 50 minutes. The photo degradation of MB, and Rh B was also conducted with 50 mg–200 mg catalyst dosage. According to the heterogeneous photocatalysis, as the catalyst loading makes more reactive sites and exhibit higher degradation efficiencies [12]. The degradation efficiency of MB and RhB increased with successive catalyst loading. However, the catalyst load over 150 mg reduced the efficiency. Fig. 5.A displays the percentage degradation profile with different catalyst dose. To inspect the selectivity, the catalyst was subjected to the degradation of 15 ppm MO solution (Fig. 5.B). There was negligible percentage of degradation indicating the selective degradation of cationic dyes. The surface charge of the nanoparticles was determined to be -38.37 mV which makes the surface selective towards cationic dye molecules via electrostatic interactions.
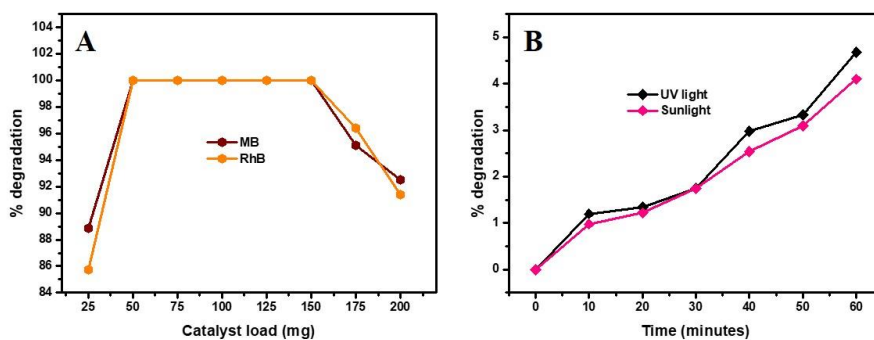

Fig. 5. A) Effect of catalyst (ZM7) loading on the degradation efficiency of MB and RhB under sunlight and B) degradation of MO under UV and sunlight.

The effect of scavengers (KI, ethanol, IPA and sodium azide) on the degradation of MB and RhB under sunlight has been presented in Fig. 6.A. Significant reduction in photodegradation efficiency of the sample was observed for MB and RhB in presence of KI, ethanol and sodium azide which implies the molecular oxygen, electrons and holes/surface hydroxyl radicals are conspicuously involved in the degradation of dye molecules. Recyclability of the catalyst was investigated for four repeated cycles under sunlight and could sustain the percentage degradation up to 88.92 and 83.15 for MB and RhB respectively. Fig. 6.B displays the percentage degradation of dye molecules after consecutive recycling of the catalyst.
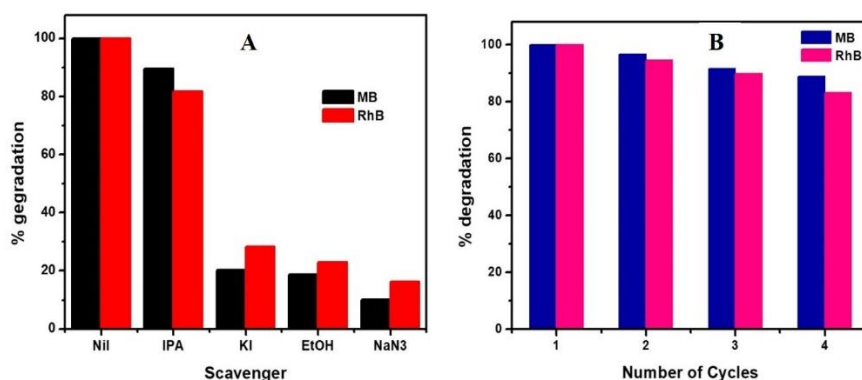

Fig. 6. A) Effect of scavengers on percentage degradation efficiencies of MB and RhB under direct sunlight and (B) recyclability of ZnO nanoparticles (ZM7) after four successive cycles of MB and RhB photodegradation under direct sunlight.

7.1.3. ZnO photocatalyst synthesized using *Gliricidia sepium* leaf extract.

The photocatalytic experiments were conducted with ZG7 sample under UV and direct sunlight. Fig. 7.A-D shows the UV-visible spectroscopic profiles for the degradation of MB and RhB. The percentage degradation efficiencies have been presented in Fig. 7.E and F. Complete removal of MB was

occurred within 35 minutes under direct sunlight-exposure. The catalyst was comparatively less efficient under UV light, where the percentage degradation was 93% after 50 min, with no further changes thereafter. Similarly, the comprehensive exclusion of RhB dye molecules was monitored in 40 minutes under direct sunlight whereas 91.1% efficiency was obtained with the catalyst under UV light.
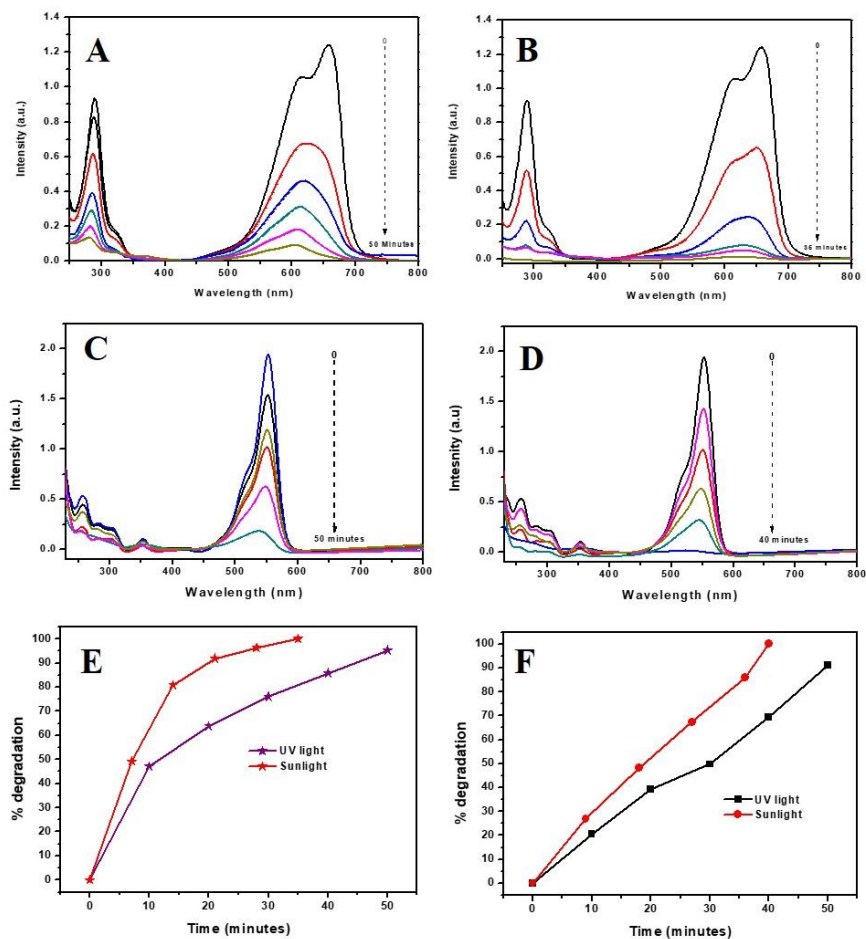

Fig. 7. Photodegradation profiles (pH ~7, room temperature) for (A) MB under UV light (B) MB under sunlight C) RhB under UV light D) RhB under sunlight and percentage degradation efficiencies for E) MB and F) RhB under UV and sunlight light using ZG7 nanoparticles.
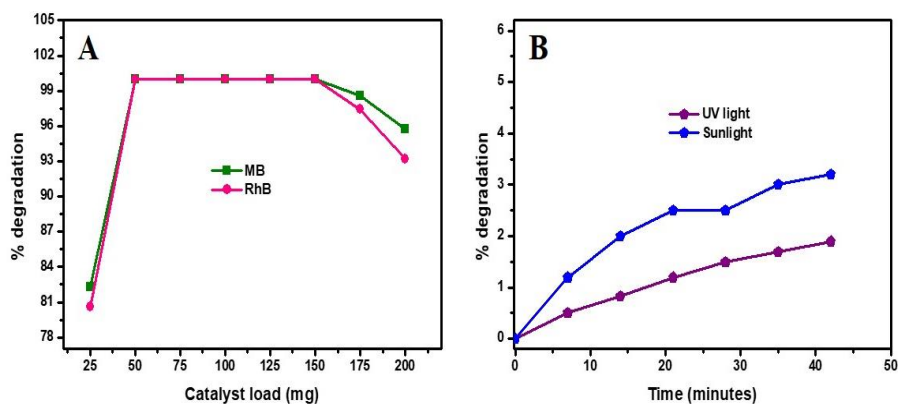
Fig. 8. A) Effect of catalyst (ZG7) loading on the degradation efficiency of MB and RhB under sunlight and B) degradation of MO under UV and sunlight.

The effect of catalyst loading was monitored for the degradation of MB and RhB under direct sunlight. Fig. 8.A depicts the percentage degradation of dye solutions with various catalyst loads. The degradation efficiency was reduced over 150 mg of ZG7 load. Photodegradation of MO dye was conducted with the nanoparticles to ensure the selectivity of degradation. Fig.8.B shows the percentage degradation of MO dye under light sources. Since no significant changes in visible colour or absorption spectra was observed, the degradation was selective towards cationic dye molecules. The catalyst surface was negatively charged (zeta potential = −36.74 mV) in neutral solution, which elucidate the selectivity.
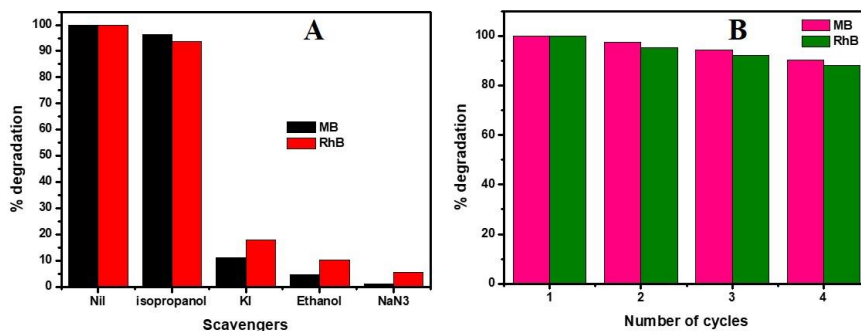
Fig. 9. A) Effect of scavengers on percentage degradation efficiencies of MB and RhB under direct sunlight and (B) recyclability of ZnO nanoparticles (ZG7) after four successive cycles of MB and RhB photodegradation under direct sunlight.

The scavengers like KI, ethanol, IPA and sodium azide introduced to the dye solutions under sunlight. Fig. 9.A shows the effect of scavengers on photodegradation of MB and RhB. The photodegradation efficiency of the sample was remarkably decreased in presence of KI, ethanol and sodium azide indicating molecular oxygen, electrons and holes/surface hydroxyl radicals are noticeably involved in the degradation of MB and RhB. Fig. 9.B displays the recyclability of the catalyst investigated for successive cycles under sunlight. After four consecutive cycles the 90.3% and 88.26% degradation was retained for MB and RhB respectively.

Table 1 presents a comparison of the performance of the ZnO photocatalysts (ZL7, ZM7, and ZG7) with that of other photocatalysts in recent reports. ZnO nanoparticles obtained in the present study showed superiority in terms of degradation time and efficiency. The catalyst achieved complete degradation of the dye pollutant in a shorter time than ZnO nanoparticles derived via other phyto-routes (which took ~ 1 h).

Table 1. Comparison of present work with some bio-synthesized ZnO nanoparticles and their photo degradation performances under direct sunlight/ visible light illumination.

Plant Extract	Particle size	Shape	Dye	Dye concentration	Catalyst load	%Degradation efficiency	Time (minutes)	Reference
Garcinia mangostana fruit pericarp extract	21 nm	Spherical	Malachite Green	10 mg/l	50 mg	99	180	[13]
Ulva lactuca seaweed extract	7 to 49 nm	Sponge-like asymmetrical shaped	Methylene blue	25 ppm	100 mg	95	120	[14]
Azadirachtaindica leaf extract	35 nm	Spherical-agglomerated	Methylene blue	1×10^{-5}M	50 mg	88	60	[15]
Tabernaemontanadivaricata green leaf extract	20-25 nm	spherical	Methylene blue	1×10^{-5}M	100 mg	100	90	[16]
Lagerstroemia Speciosa leaf extract	40 nm	Variable	Methyl orange	1 mg in 100 ml	0.1 mg	93.4	100	[17]
Ferulagoangulata boiss extract	44 nm	Spheroid	Rhodamine B	100μM	50 mg	93	150	[18]
Cyanometraramiflora leaf extract	13.33 nm	Flower	Rhodamine B	10μM	20 mg	98	200	[19]
Citrus lemon extract	49.16	Near spherical	Methylene blue	15 ppm	50 mg	100	40	Present work
Citrus lemon extract	49.16	Near spherical	Rhodamine B	10 ppm	50 mg	100	45	Present work
Abelmoschus esculentus	29–70 nm	Near spherical and elongated	Methylene blue	15 ppm	50 mg	100	35	Present work
Abelmoschus esculentus	29-70 mn	Near spherical and elongated	Rhodamine B	10 ppm	50 mg	100	40	Present work
Gliricidiasepium leaf extract	55.7 nm	Near spherical and elongated	Methylene blue	15 ppm	50 mg	100	35	Present work
Gliricidiasepium leaf extract	55.7 nm	Near spherical and elongated	Rhodamine B	10 ppm	50 mg	100	40	Present work

7.2. Antibacterial activity of Photocatalytic ZnO Nanoparticles

ZnO has been incorporated into the linings of food cans in packages for meat, fish, corn, and peas to preserve colours and avoid spoilage owing to its antibacterial properties. During wastewater processing, bacterial decontamination is essential but challenging. Materials possessing antimicrobial action along with photocatalytic properties can be worthy candidates for water processing applications. The antibacterial activity of photocatalytic ZnO nanoparticles (ZL7, ZM7, and ZG7) was evaluated towards K. pneumoniae and S. aureus pathogenic stains via a well-diffusion assay. The diameter of the inhibition zone is presented in Fig. 10.The

bactericidal action of ZnO nanoparticles was evident from the well diffusion assays. A clear zone of inhibition could observe around all diffusion wells for samples loaded with ZnO nanoparticles. The zone diameter has increased with increase in ZnO dosage. All the photocatalysts offer antibacterial activity towards the studied Gram-positive and Gram-negative bacterial strains. The exact antibacterial mechanism of action of nanoparticles is not known, but could involve internalization of nanoparticles or reactive oxygen species (ROS) to bacterial cells, thereby causing inner stress and loss of cell integrity [20].
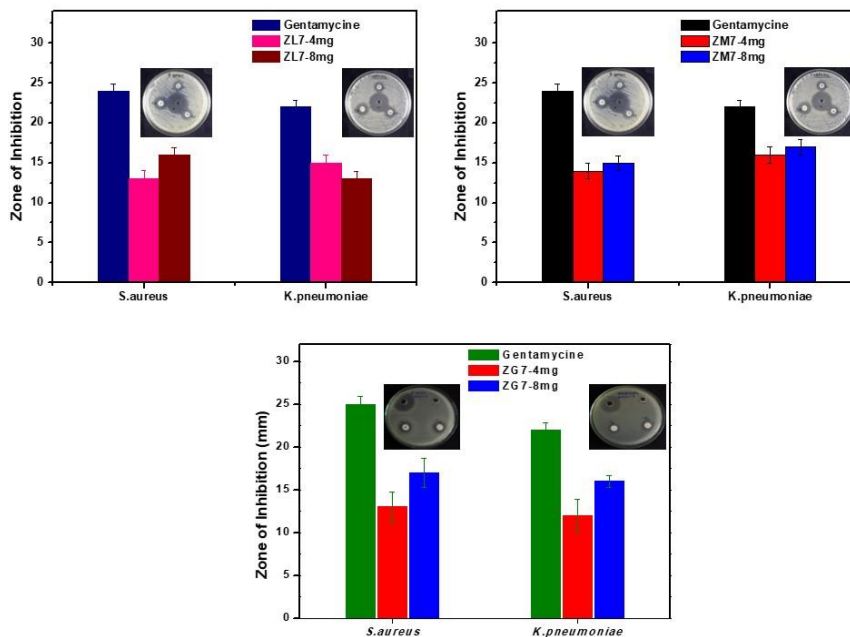

Fig. 10. Zone of inhibition measured for K. pneumoniae and S. aureus strains with standard and synthesized ZnO nanoparticles A) ZL7, B)ZM7 and C) ZG7.

7.3. Thermoluminescence Emission

Thermally stimulated luminescence (TL) has been employed widely to investigate crystal defects. Synthetic and natural TL-phosphors have been introduced for low- and high-dose applications in industrial, environmental and domestic sectors [21, 22]. Pure ZnO and modified structures (e.g., doped and composite materials) have been studied according to TL properties after exposure to different doses of ionizing radiation below room temperature [23-26]. Despite their inert nature, non-toxic and insoluble characteristics, ZnO can offer TL emission above room temperature, which makes them apposite material for thermoluminescence dosimeters (TLDs) [27, 28]. TL active materials are extensively employed in dosimetry appropriated for radiation therapy, personal monitoring, health and biological sciences. For the past few years, a considerable number of nanophosphors has been introduced for TLD applications [29].

The TL glow curves obtained for the ZnO samples (ZL5, ZL7, ZM5, ZM7, ZG5 and ZG7) subsequently being exposed to gamma irradiation (10 Gy) recorded at a constant heating rate of 2°C are presented in Fig 11. All samples have a single broad glow curve with a single maximum located at 304°C (ZL5), 323°C (ZL7), 312°C (ZM5), 335°C (ZM7) 323°C (ZG5), and 319°C (ZG7). The distinct and intense peaks evolved at high temperatures are associated with the deep localized electron and hole trap states which is suitable for domestic TL dosimeters [30]. The materials have good response even at low gamma dosages. We obtained stable TL peaks all above 300°C indicating the recombination of charge carriers at the deep traps and broad nature of glow curves designates the traps being distributed in the band gap of ZnO nanostructure [29-32]. Intrinsic surface defects (F and F+ centres) induced by the irradiation have been identified as the charge donor sources in ZnO which includes oxygen vacancies (V_O) and interstitial zinc (Zn_i) defects [33]. The energy levels allied with the Zn_i are relatively shallow energy levels

whereas V_O energy levels are deep [34]. Thus, the TL emission exhibited by the samples are ascribed to the reunion of electron-hole pairs that are released from the surface states associated with the vacant oxygen centres.TL glow curves recorded at different gamma dosages have similar profiles indicating identical physical properties of the traps.
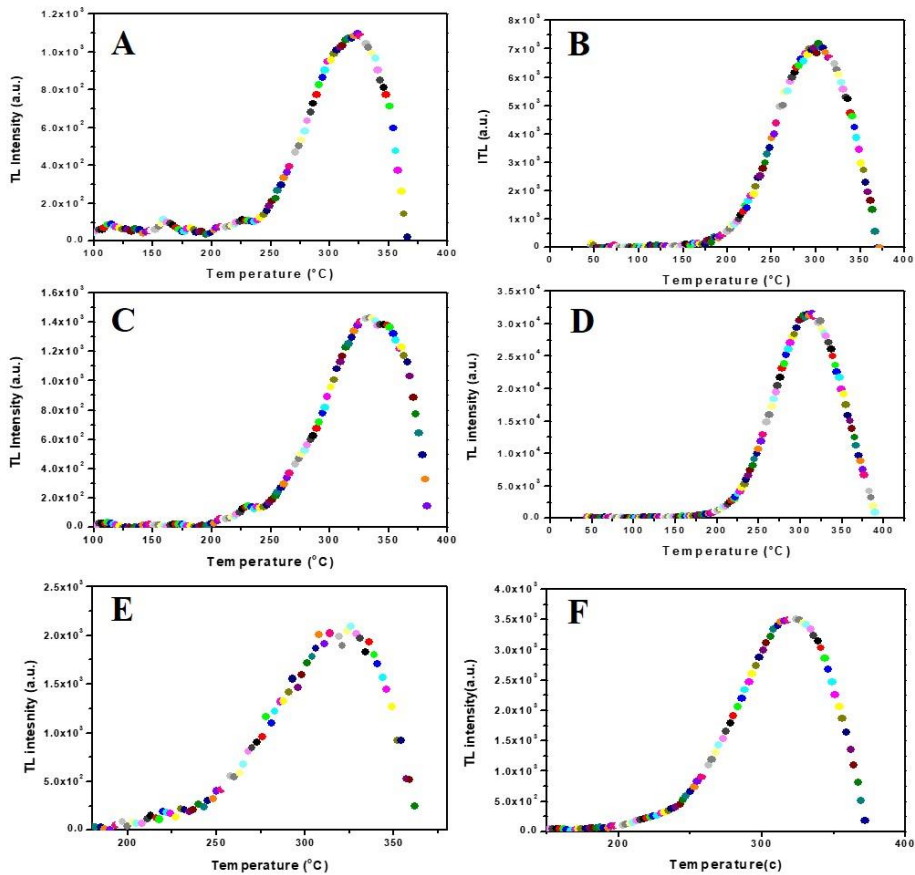

Fig 11. TL glow curves resolved for ZnO samples A) ZL5, B) ZL7, C) ZM5, D) ZM7, E) ZG5 and F) ZG7 previously exposed to gamma radiation (10 Gy) at a constant heating rate of 2°C.
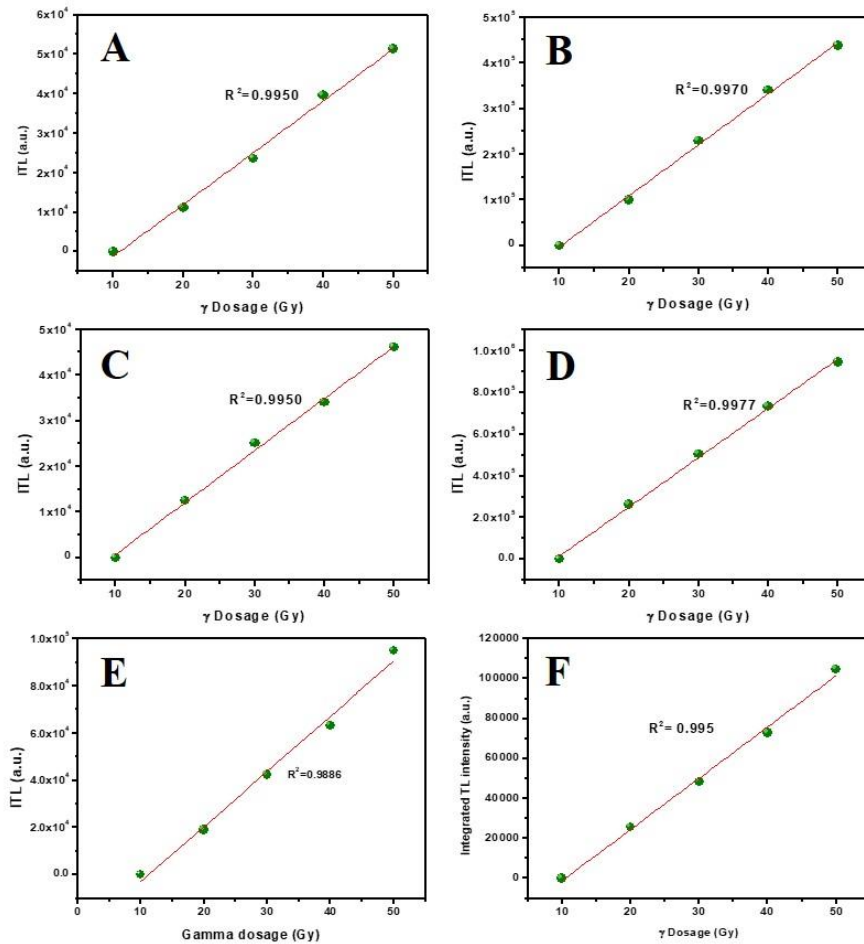
Fig. 12. Integrated TL profile of ZnO samples A) ZL5, B) ZL7, C) ZM5, D) ZM7, E) ZG5 and F) ZG7 as a function of gamma dosage (10-50 Gy) at constant heating rate of 2°C.

The highest intensity of TL emission was recorded for ZM7 nanoparticle. A common trend of enhanced intensity can be observed for the samples prepared at higher calcination temperature (700°C) due to increased crystallinity and purity by the elimination of carbonaceous residues. Fig. 12 shows the integrated TL (ITL) as a function of gamma dosage 10-50 Gy for

the ZnO nanophosphors obtained. The sample exhibited close-to-linear dependence up to gamma radiation doses studied. Besides, signs of saturation were not observed for the sample. The linear ITL profile has been displayed by all the samples which is desirable for radiation dosimeters.

Summary

➢ The photocatalytic activity of ZnO nanoparticles ZL7, ZM7, and ZG7 prepared using *Citrus lemon extract, Abelmoschus esculentus* mucilage, and *Gliricidiasepium* leaf extract was investigated. All samples exhibited substantial activity for the photodegradation of MB and RhB. The dye molecules were completely removed within 35-45 minutes under direct sunlight. The samples are more active on exposure to sunlight rather than in UV light illumination due to the favorable semiconductor band gap (3.13, 3.10 and 3.11eV). The surface charge of the nanoparticles was determined to be negative and photodegradation was selective towards cationic dyes. The effect of catalyst load, scavengers, and recyclability of the photocatalysts were investigated. The degradation efficiency for MB and RhB was significantly reduced in presence of KI, ethanol and sodium azide indicating the molecular oxygen, electrons and holes/surface hydroxyl radicals play significant role in degradation. 80-90% of degradation efficiency could retain for the samples after four consecutive cycles. Moreover, a substantial zone of inhibition was observed in the well-diffusion assay for Gram-positive and Gram-negative bacterial strains when ZnO nanoparticles were loaded. Antibacterial activity along with the photocatalytic property ensures the materials as good choice for water treatment.

➢ The thermoluminescence emission of ZnO nanoparticles ZL5, ZL7, ZM5, ZM7, ZG5, and ZG7 were studied. We could resolve well defined and intense single glow curves all situated above 300ºC. High temperature glow curves indicate the recombination of charge carriers from deep traps most probably from vacant oxygen surface states. Owing to their higher crystallinity and purity the samples calcined at 700ºC (ZL7. ZM7, and ZG7) depicts more intense glow curves compared to that at 500ºC (ZL5, ZM5, and ZG5). The highest intensity of TL emission was recorded for ZM7 nanoparticle. All samples are suitable for high temperature TLDs and linear dependence observed in ITL profile is desirable for dosimeters. More extensive monitoring of the TL properties envisioned.

Reference

1. N.S. Mutamim, Z. Z. Noor, M.A. Hassan and G. Olsson, Desalination, 2012, 305, 1.

2. B. Vellaichamy and P. Periakaruppan, RSC Adv., 2016, 6, 31653.

3. A.R. Prasad and A. Joseph, RSC Adv., 2017, 7, 20960.

4. B. Archana, K. Manjunath, G. Nagaraju, K.C. Sekhar and N. Kottam, Int. J. Hydrogen Energy, 2017, 42, 5125.

5. Y.J. Jang, C. Simer, T. Ohm, Mater. Res. Bull., 2006, 41, 67.

6. C.W. Tang, Mod. Res. Catal., 2013, 2, 19.

7. A.N. Kadam, R.S. Dhabbe, M.R. Kokate, Y.B. Gaikwad, K.M. Garadkar, Spectrochim. Acta Mol. Biomol. Spectrosc., 2014, 133, 669.

8. S.S.M. Hassan, W.I.M. El Azab, H.R. Ali, M.S.M. Mansour, Adv. Nat. Sci. Nanosci. Nanotechnol., 2015, 6, 045012.

9. K. Byrappa, A.K. Subramani, S. Ananda, K.M.L. Rai, R. Dinesh, M. Yoshimura, Bull. Mater. Sci., 2006, 29, 433.

10. Y. Sun and J. J. Pignatello, Environ. Sci. Technol., 1995, 29, 2065.

11.   C. Miner, G. Mariella, V. Maurino, D. Vione and E. Pelizzetti, Langmuir, 2000, 16, 8964.

12.   J. Krýsa, M. Keppert, J. Jirkovský, J. Šubrt, V. Štengl, Mater. Chem. Phys., 2004, 86, 333.

13.   M. Aminuzzaman, L. P. Ying, W. S. Goh and A. Watanabe, Bull. Mater. Sci., 2018, 41, 50.

14.   R. Ishwarya, B. Vaseeharan, S. Kalyani, B. Banumathi, M. Govindarajan, N.S. Alharbi, S. Kadaikunnan, M.N. Al-anbr, J.M. Khaled and G. Benelli, J. Photochem. Photobiol., B, 2018, 178, 249.

15.   A.R. Prasad, S. M. Basheer, I. R. Gupta, K. K. Elyas and A. Joseph, Mater. Chem. Phys., 2020, 240, 122115.

16.   K.C. Lalithambika, A. Thayumanavan, K. Ravichandran and S. Sriram, J. Mater. Sci.: Mater. Electron., 2017, 28, 2062.

17.   A. Raja, S. Ashokkumar, R.P. Marthandam, J. Jayachandiran, C.P. Kathiwada, K. Kaviyarasu, R.G. Raman and M. Swaminathan, J. Photochem. Photobiol., B, 2018, 181, 53.

18.   V. Sai Saraswathi, J. Tatsugi, P.-K. Shin and K. Santhakumar, J. Photochem. Photobiol., B, 2017, 167, 89.

19.   E.S. Mehr, M. Sorbiun, A. Ramazani and S.T. Fardood, J. Mater. Sci.: Mater. Electron., 2018, 29, 1333.

20.   T. Varadavenkatesan, E. Lyubchik, S. Pai, A. Pugazhendhi, R. Vinayagam and R. Selvaraj, J. Photochem. Photobiol., B, 2019, 199, 111621.

21.   S.E. Burruel-Ibarra, C. Cruz-Va´zquez1, R. Bernal, J.R. Martı´nezCastelo, A.R. Garcı´aHaro and V.R. Orante-Barro´n, Mater. Sci. Forum, 2013, 755, 139.

22.   R. Chen and S.W.S. McKeever: Theory of Thermoluminescence and Related Phenomena, World Scientific, Singapore, 1997.

23.   V.A. Nikitenko, K.E. Tarkpea, I. V. Pykanov and S.G. Stoyukhin, J. Appl. Spectrosc., 2001, 68, 502.

24.   W.A. Hadi, M. S. Shur and S.K. O'Leary, J. Mater. Sci.: Mater. Electron., 2012, 23, 1.

25.   D. Millers, L. Grigorjeva, W. Łojkowski and T. Strachowski, Radiat. Meas., 2004, 38, 589.

26. M. Oztas, J. Mater. Sci.: Mater. Electron., 2006, 17, 937.

27. A.N. Yazici, M. Oztas and M. Bedir, Opt. Mater., 2007, 29, 1091.

28. P.T. Hsieh, Y.C. Chen, K.S. Kao and C.M. Wang, Phys. B, 2008, 403, 178.

29. A.J. Reddy, R.H. Krishna, B.M. Nagabhushana, M.K. Kokila, H. Nagabhushana, C. Shivakumara, R.P.S. Chakradhar,Spectrochim Acta A., 2015, 139, 262.

30. V. R. Orante-Barrón, F. M. Escobar-Ochoa, C. Cruz-Vázquez, and R. Bernal, J. Nanomater. 2015, 2015, 273571-1-5.

31. S. E. Burruel-Ibarra, C. Cruz-Vázquez, R. Bernal, J. R. Martínez-Castelo, A. R. García Haro, V. R. Orante-Barrón, Mater. Sci. Forum, 2013, 755,139.

32. A. J. Reddy, M. K. Kokila, H. Nagabhushana, J. L. Rao, C. Shivakumara, B. M. Nagabhushana, R. P. S. Chakradhar, Spectrochim Acta A, 2011, 81, 59.

33. N. Pushpa, M.K. Kokila, K.R. Nagabhushana, Nucl. Instrum. Methods Phys. Res., B, 2016, 379, 62.

34. M.K. Kavitha, K.B. Jinesh, R. Philip, P. Gopinath, H. John, Phys. Chem. Chem. Phys., 2014, 16, 25093.

Conclusion and Future outlook

"Being able to do research in a real-time way is the way research needs to be done in future."

Anne Wojcicki

The practice of green routes in synthesis is highly demanded for materials preparation in concern of better human health, environment and economy. Being rapid, sustainable and follow ecological and economic protocol, this method of synthesis of nanomaterials using plant products is an active area of research in chemical science. As an outcome of this research work, we could successfully produce phyto-mediated ZnO nanoparticles having significant biological activities, photocatalytic activity and thermoluminescence property. The Zinc oxide nanoparticles were synthesized using *Citrus lemon* extract (ZL), *Abelmoschus esculents* mucilage (ZM), and *Gliricidia sepium* leaf extract (ZG). A detailed characterization of the materials was performed with different analytical techniques. Zinc oxide nanoparticles were obtained in its hexagonal wurtzite structure devoid of any secondary phases. However, traces of carbon content were encountered in the elemental and composition analysis of the samples due to the presence of organic residues. The surface morphology, particle size, crystallinity and surface charge of the samples vary with the calcination temperature (300ºC, 500ºC, and 700ºC in each sample sets) and the plant extract. These variations accounts for the difference in their physical and biological activities.

In-vitro α-amylase and α-glucosidase inhibition studies reveals the ZnO nanoparticles synthesized using C*itrus lemon* extract shows selective inhibition towards α-glucosidase. The samples synthesized using

Abelmoschus esculents mucilage shows substantial and comparable activity towards α-glucosidase. Only the sample ZM5 has considerable activity towards α-amylase enzyme. ZnO nanoparticles synthesised using *Gliricidia sepium* leaf extract display significant inhibition towards α-amylase and α-glucosidase. The cytotoxicity and selectivity index of the samples obtained are well within acceptable limit. These ZnO nanoparticles also show good binding property with BSA. The intensity of the emission spectra of BSA, tryptophan and tyrosine residues were reduced with the addition of ZnO (ZL, ZM, and ZG) nanoparticles keeping negligible changes in the emission wavelength which indicate the intactness of the protein conformation. Since the physical properties of ZnO varies with the calcination temperature and the composition of the plant extract, their synergistically influence in biological systems show different trends in the *In-vitro* biological activities. Further, we have generated docking models for ZnO- α-amylase, ZnO- α-glucosidase, and ZnO-BSA interactions. The experimental and theoretical screening suggest that the nanoparticles are mild α-amylase inhibitors and strong candidates for α-glucosidase inhibition. According to theoretical evaluations, the interaction in ZnO-BSA is most favourable at low particle dimensions. However, the complexes generated with ZnO-BSA interactions have shown chemical interactions (H-bonding) through different amino acid residues implying favourable association.

ZnO nanoparticles exhibited remarkable activity for the photodegradation of MB and RhB dyes. The degradation of dyes was complete with in 35-45 minutes on exposure to direct sunlight. Interestingly, the nanoparticles have shown superior activity under direct sunlight than in UV light owing to their favorable optical band gap. Negative surface charge of nanoparticles accounts for the selectivity observed towards the cationic dyes. The photocatalytic ZnO samples have aantibacterial activity which ensures the

materials as good choice for water treatment. We could resolve well defined and intense high temperature TL glow curves for ZnO nanoparticles.

These outcomes can be integrated to the real-time applications by extended research. The biological experiments demand *in-vivo* monitoring over the *in-vitro* results since it explores better understanding on the net effects on the living organisms. *In-vivo* research includes animal testing and various clinical trials. Hence the *in-vivo* monitoring of anti-diabetic activity (α-glucosidase and α-amylase inhibition) of ZnO nanoparticles should be explored to understand the effects in real biological conditions. Additionally, the *in-vitro* and *in-vivo* monitoring of protein kinase-B enzyme which plays important role in glucose transport and metabolism is also besieged. Similarly, the *in-vivo* studies have to be conducted over the *in-vitro* ZnO-BSA interactions.

ZnO nanoparticles have remarkable selective photocatalytic activity towards the cationic dye pollutants. The photocatalytic property of the materials can be examined further for the treatment of other organic pollutants getting released to the water resources. Moreover, the photocatalytic activity of the nanoparticles under direct sun-light can be explored for the semiconductor solar cell applications. We have an ongoing research on composite materials including these photocatalytic ZnO nanoparticles aimed for the instantaneous removal of chromium from water bodies. Thermoluminescence of ZnO nanoparticles desires further inspections on emission with different heating rates and TL fading to evaluate the potential of the materials for implementing real-time dosimeters.

Publications
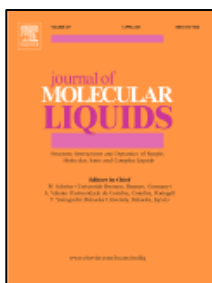
Anupama R.Prasad, Linda Williams, Julia Garvasis, K.O.Shamsheera, Sabeel M.Basheer, Mathew Kuruvilla, Abraham Joseph, https://doi.org/10.1016/j.molliq.2021.115805

Anupama R. Prasad, Anagha M., Shamsheera K. O. and Abraham Joseph, Bio-fabricated ZnO nanoparticles: direct sunlightdriven selective photodegradation, antibacterial activity, and thermoluminescence emission characteristics, **New Journal of Chemistry** 2020, **44**, 8273-8279.

Anupama R. Prasad, Sabeel M. Basheer, Induja R. Gupta, K.K. Elyas, Abraham Joseph, Investigation on Bovine Serum Albumin (BSA) binding efficiency and antibacterial activity of ZnO nanoparticles, Materials Chemistry and Physics 240 (2020) 122115
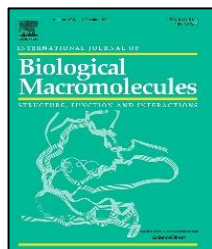
Anupama R. Prasad, Sabeel M. Basheer, Linda Williams, Abraham Joseph, Highly selective inhibition of α-glucosidase by green synthesised ZnO nanoparticles - In-vitro screening and in-silico docking studies, International Journal of Biological Macromolecules 139 (2019) 712-718.

Anupama R. Prasad, Julia Garvasis, Shamsheera Kunnekkat Oruvil, Abraham Joseph, Bio-inspired green synthesis of zinc oxide nanoparticles using Abelmoschus esculentus mucilage and selective degradation of cationic dye pollutants, Journal of Physics and Chemistry of Solids 127(2019) 265-274.

Anupama R. Prasad, P. Rugmini Ammal, Abraham Joseph, Effective photocatalytic removal of different dye stuffs using green synthesized zinc oxide nanogranules, Materials Research Bulletin 102 (2018) 116–121.

Other Publications

Anupama R. Prasad and Abraham Joseph, Synthesis, characterization and investigation of methyl orange dye removal from aqueous solutions using waterborne poly vinyl pyrrolidone (PVP) stabilized poly aniline (PANI) core–shell nanoparticles, RSC Advances 2017, 7, 20960.
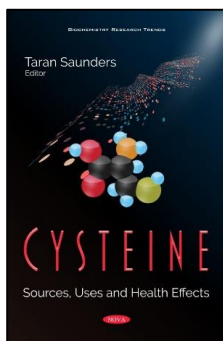
Anupama R Prasad, Mathew Kuruvilla and Abraham Joseph, Applications of cysteine in health and industries, Cysteine: Sources, Uses and Health Effects, Edited by Taran Saunders, ISBN: 978-1-53619-033-5, Published 2021 by Nova Science Publishers, Inc., Hauppauge, NY, USA.
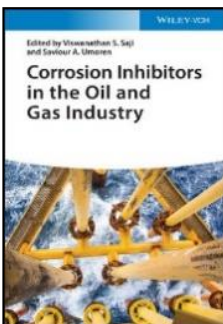
Anupama R. Prasad, Anupama Kunyankandy, and Abraham Joseph, Corrosion Inhibition in Oil and Gas Industry: Economic Considerations, Corrosion Inhibitors in the Oil and Gas Industry, First Edition. Edited by Viswanathan S. Saji and Saviour A. Umoren, Wiley-VCH Verlag GmbH & Co. KGaA. Published 2020 by Wiley-VCH Verlag GmbH & Co. KGaA.
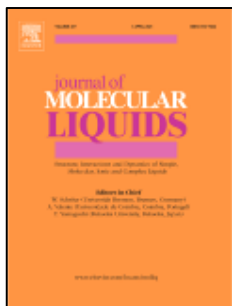
K.O. Shamsheera, <u>Anupama R. Prasad</u>, P.K. Jaseela, Abraham Joseph, Effect of surfactant addition to Guar Gum and protection of mild steel in hydrochloric acid at high temperatures: Experimental and theoretical studies, Journal of Molecular Liquids 331 (2021) 115807.
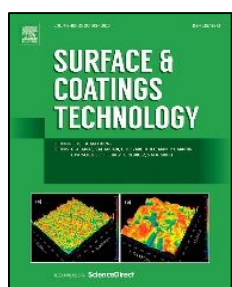
K.O. Shamsheera, <u>Anupama R. Prasad</u>, Abraham Joseph, Extended protection of mild steel in saline and acidic environment using stearic acid grafted chitosan preloaded with mesoporous-hydrophobic silica (mhSiO2), Surface & Coatings Technology 402 (2020) 126350.

Shamsheera KO, <u>Anupama R. Prasad</u>, Jaseela PK, Abraham Joseph, Development of self-assembled monolayer of stearic acid grafted chitosan on mild steel and inhibition of corrosion in hydrochloric acid, Chemical Data Collections 28 (2020) 100402.

Linda Williams, <u>Anupama R. Prasad</u>, P. Sowmya, Abraham Joseph, Characterization and Temperature dependent DC conductivity study of bio templated nickel oxide nanoparticles (NiO) and their composites using polyaniline (PANI), Materials Chemistry and Physics 242 (2020) 122469.
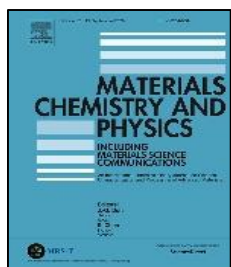
K.O. Shamsheera, R. <u>Prasad Anupama</u>, Joseph Abraham, Computational simulation, surface characterization, adsorption studiesand electrochemical investigation on the interaction of guar gumwith mild steel in HCl environment, Results in Chemistry 2 (2020) 100054.

Rugmini Ammal P a , Anupama R. Prasad b , Abraham Joseph, Synthesis, characterization, in silico, and in vitro biological screening of coordination compounds with 1,2,4-triazine based biocompatible ligands and selected 3d-metal ions, <u>https://doi.org/10.1016/j.heliyon.2020.e05144</u>

Julia Garvasis, <u>Anupama R. Prasad</u>, K.O. Shamsheera, P.K. Jaseela, Abraham Joseph, Efficient removal of Congo red from aqueous solutions using phytogenic aluminum sulfate nano coagulant, Materials Chemistry and Physics 251 (2020) 123040.

Shamsheera K O, <u>Anupama R Prasad</u>, Julia Garvasis, Sabeel M Basheer & Abraham Joseph, Stearic acid grafted chitosan/epoxy blend surface coating for prolonged protection of mild steel in saline environment, Journal of Addition Science and Technology 33 (2019) 2250-2264.
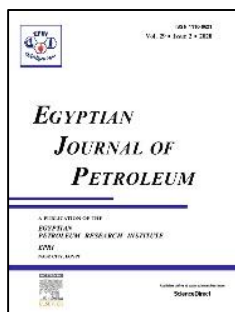
K.M. Shainy, Anupama R. Prasad, Asha Thomas, Abraham Joseph, Synergistic interaction of 2-amino 4-methyl benzothiazole (AMBT) and benzotriazole (BTZ) offers excellent protection to mild steel exposed in acid atmosphere at elevated temperatures: Electrochemical, computational and surface studies, Egyptian Journal of Petroleum 28 (2019) 35–45.

Rugmini Ammal P, Anupama R Prasad, Ramya K, Sam John & Abraham Joseph, Protection of mild steel in hydrochloric acid using methyl benzimidazole substituted 1, 3, 4- oxadiazole: computational, electroanalytical, thermo-dynamic and kinetic studies, Journal of Addition Science and Technology 33 (2019) 2227-2249.

Mathew Kuruvilla, Anupama R. Prasad, K. M. Shainy, Abraham Joseph, Protection of Metallic Copper from the Attack of Sulphuric Acid Using HDMMA, a Schiff Base Derived from l-Cysteine and 2-Hydroxy-1-naphthaldehyde, Journal of Bio- and Tribo-Corrosion (2019) 5:9.
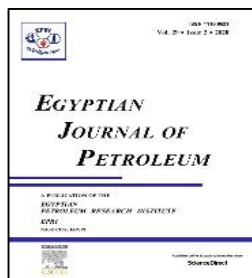
P. Rugmini Ammal, Anupama R. Prasad, Abraham Joseph, Comparative studies on the electrochemical and physicochemical behaviour of three different benzimidazole motifs as corrosion inhibitor for mild steel in hydrochloric acid, Egyptian Journal of Petroleum 27 (2018) 1067–1076.

Mathew Kuruvilla, <u>Anupama R. Prasad</u>, Sam John, Abraham Joseph, Enhanced Inhibition of the Corrosion of Metallic Copper Exposed in Sulphuric Acid Through the Synergistic Interaction of Cysteine and Alanine: Electrochemical and Computational Studies, J Bio Tribo Corros (2017) 3:5

Under Revision:

- Self cleaning surfaces: Experimental Advances and Surface Model Controversies – 'Photocatalysis' De Gruyter publishers.

- Electrochemical and surface examination of aqueous sol-gel derived corrosion resistant zirconia network developed on mild steel surface – Materials Chemistry and Physics.

List of Presentations

1. **Biogenic ZnO NPs: TL emission and direct sunlight assisted selective photodegradation of cationic dyes,** 14th RSC-CRSI joint symposium and 26th CRSI National symposium in chemistry 2020, held at VIT Vellore, Tamilnadu, India. **<u>Secured the RSC-Chemical Communication Poster Prize.</u>**

2. **Direct sunlight driven selective photodegradation, antibacterial activity and thermoluminescence emission of bio fabricated ZnO nanoparticles via *Gliricidia sepium leaf extract,*** National seminar on Frontiers in Chemical Sciences (FCS-2020), January 2020, held at university of Calicut. Organized by department of Chemistry, University of Calicut, Kerala, India. **<u>Secured second prize for best oral presentation.</u>**

3. **Green synthesized zinc oxide nanogranules for the photodegradation of organic dye stuffs**, National seminar on Frontiers in Chemical Sciences (FCS-2018), February 2018, held at university of Calicut, Organized by the department of chemistry and KSCSTE.

4. **2-mercaptobenzimidazole loaded nano ZnO: CeO$_2$ combination as protective coating for mild steel corrosion in HCl,** International Seminar on Environment, Society and Economy AMBIENTE December 2017, Organized by Department of Chemistry, St. Joseph's College for women, Alapuzha and sponsored by Keral State Council for Science Technology and Environment.

5. **Cyclic voltametric characterization of polyanilline/polyvinyl pyrollidone nanoparticles,** TEQIP II Sponsored International Conference on Advances in Biological, Chemical and Physical Sciences (ABCPS'2017), March 2017 jointly organized by the departments of Biotechnology, Chemistry and Physics BIT campus, Anna University, Tiruchirappalli.

6. **Electrochemical investigation on ZrO$_2$ nanocoating for corrosion protection of mild steel in Hydrochloric acid,** International Symposium on New Trends in Applied Chemistry (NTAC-2017), February 2017, Organized by Post Graduate and Research department of Chemistry, Sacred Heart College (Autonomous), Thevara.